Title

Noninvasive Imaging of Hemorrhagic Myocardial infarction with Confounder-Corrected T2* Cardiac MRI

Author

Guan, Xingmin

Publication Date

2022

Peer reviewed|Thesis/dissertation

UNIVERSITY OF CALIFORNIA

Los Angeles

Noninvasive Imaging of Hemorrhagic Myocardial infarction with Confounder-Corrected T_2* Cardiac MRI

A dissertation submitted in partial satisfaction of the requirements for the degree Doctor of Philosophy in Bioengineering

by

Xingmin Guan

2022

ABSTRACT OF THE DISSERTATION

Noninvasive Imaging of Hemorrhagic Myocardial infarction with

Confounder-Corrected T_2* Cardiac MRI

by

Xingmin Guan

Doctor of Philosophy in Bioengineering

University of California, Los Angeles, 2022

Professor Holden H. Wu, Co-Chair

Professor Rohan Dharmakumar, Co-Chair

The current gold-standard approach for detection and quantification of intramyocardial hemorrhage (IMH) is T_2* cardiovascular magnetic resonance imaging (CMR). T_2*-based imaging techniques have been demonstrated to have high sensitivity for detecting hemorrhage and residual iron. The conventional T_2*-based imaging employed for IMH imaging is based on a 2D breath-held, ECG-triggered, segmented, multi-gradient-echo sequence.

More recently, a dark-blood cardiac T_2* MRI technique has emerged for imaging of global iron overload such as thalassemia. It has been interchangeably used with bright-blood T_2* MRI

for imaging of local iron overload such as intramyocardial hemorrhage. To date however, dark-blood T_2* techniques for intramyocardial hemorrhage characterization has not been validated. In Chapters 2 and 3, we investigated the diagnostic capacity of dark-blood T_2* MRI against bright-blood T_2* MRI for intramyocardial hemorrhage characterization in both clinical and preclinical settings. We found that double-inversion-recovery prepared dark-blood T_2* images provide lower signal-to-noise ratio and lower contrast-to-noise ratio between hemorrhage and remote myocardium, consequently underestimating the hemorrhage extent. Dark-blood T_2* MRI also demonstrated weaker sensitivity, specificity, accuracy, and inter-observer variability compared to bright-blood T_2*-weighted MRI. Our studies also showed that the loss in SNR and CNR in dark-blood T_2* imaging emerges from the signal loss following double-inversion-recovery preparation and insufficient recovery time between double-inversion-recovery preparation and readout. Hence, we conclude that dark-blood T_2* MRI does not have the same diagnostic capacity for assessment of intramyocardial hemorrhage and bright-blood T_2* MRI should be the preferred choice for clinical use.

Studies have shown that fat infiltration is a common phenomenon in chronic myocardial infarction. However, signal from fat protons can confound the T_2* assessment of intramyocardial hemorrhage. To address this issue, in Chapter 4, we studied the influence of fat infiltration on iron quantification in T_2* mapping using a widely accepted water-fat separation algorithm. Specifically, we evaluated the temporal dependence of fat infiltration in hemorrhagic myocardial infarctions. We found that fat infiltration was observed in early and late chronic phases of myocardial infarctions, which if not corrected for, can underestimate the extent of iron content within the infarct zone. Notably, we also found that the amount of fat infiltration in chronic phase of MI was closely correlated with the amount of iron.

Another major confounder in conventional 2D breath-held ECG-gated T_2* imaging is motion artifacts. In clinical settings, patients with acute myocardial infarctions often find it difficult to hold their breath during cardiac MRI exams. Some patients may even suffer from arrhythmia (irregular heartbeat). Both situations can lead to unsuccessful gating during data acquisition leading to motion artifacts on T_2* images especially with long echo times. To address this issue, in Chapter 5, we developed a motion-resolved fully ungated free-breathing 3D cardiac T_2* imaging technique using a low-rank tensor framework to accommodate clinical needs and to mitigate motion artifacts due to unsuccessful breath-holds or ECG gating. We tested our 3D LRT technique in healthy volunteers and animal models for image quality, SNR and T_2*. We found that the proposed 3D LRT technique can provide superior image quality compared to conventional T_2* techniques at the same level of signal-to-noise ratio. T_2* measured from proposed 3D LRT data showed excellent agreement with T_2* from conventional 2D approach. We also found that a key benefit of 3D acquisition is that it permits the reconstruction of high-resolution T_2* images using the proposed 3D LRT T_2* approach. High-resolution T_2* images from proposed 3D LRT approach showed superior image quality and diagnostic capacity for assessment of intramyocardial hemorrhage. In Chapter 6, the proposed 3D LRT T_2* imaging approach was validated on an animal model for feasibility and capability for characterization of intramyocardial hemorrhage. We found that our 3D LRT approach had excellent image quality and diagnostic accuracy in the assessment of intramyocardial hemorrhage compared to the 2D breath-held and gated acquisitions.

Broadly, this dissertation identified and corrected a number of critical confounders affecting the accuracy of T_2* MRI in assessment of intramyocardial hemorrhage. By identifying and solving these confounders in T_2* imaging, we aim to improve the diagnostic capability of MRI for prognosis and therapeutic care of patients with hemorrhagic myocardial infarctions.

In future work, feasibility of the newly developed fully ungated free-breathing 3D LRT T_2* imaging technique will be investigated on patients for imaging of intramyocardial hemorrhage. And the potential of high-resolution T_2* imaging which greatly improved intravoxel dephasing due to off-resonance will be explored.

This dissertation of Xingmin Guan is approved.

Michael Albert Thomas

Zhaoyang Fan

Holden H. Wu, Co-Chair

Rohan Dharmakumar, Co-Chair

University of California, Los Angeles

2022

Dedicated to my parents, Wei Guan and Juan Yin, who have unconditionally supported me throughout my PhD studies.

Table of Contents

LIST OF ACRONYMS

Units

h	Hour
min	Minute
mm	Millimeter
ms	Millisecond
mT	Millitesla
s	Second
T	Tesla

Statistics

ANOVA	Analysis of Variance
AUC	Area Under the Curve
COV	Coefficient of Variation
ICC	Intra-class Correlation Coefficient
p	Statistical Significance Coefficient
r	Regression coefficient
ROC	Receiver Operating Characteristic Curve
SD	Standard Deviation
SEM	Standard Error of Mean

Mathematics

HOSVD	Higher-Order Singular Value Decomposition

LRT	Low-Rank Tensor
SVD	Singular Value Decomposition

Medicine

bpm	Beats Per Minute
CAD	Coronary Artery Disease
CHF	Congestive Heart Failure
CMR	Cardiac Magnetic Resonance
CT	Computed Tomography
CVD	Cardiovascular Disease
ECG	Electrocardiogram
ECM	Extracellular Matrix
EF	Ejection Fraction
FDA	Food and Drug Administration
HF	Heart Failure
I/R injury	Ischemia Reperfusion Injury
IACUC	Institutional Animal Use and Care Committee
IMH	Intramyocardial Hemorrhage
IRA	Infarction Related Artery
IV	Intravenous
LV	Left Ventricle
LVEDV	Left Ventricular End-Diastolic Volume
LVEF	Left Ventricular Ejection Fraction

LVESV	Left Ventricular End-Systolic Volume
MACE	Major Adverse Cardiovascular Events
MI	Myocardial Infarction
MRI	Magnetic Resonance Imaging
MVO	Microvascular Obstruction
NIH	National Institutes of Health
PB	Prussian Blue
PCI	Percutaneous Coronary Intervention
PO	Oral administration
RBC	Red Blood Cell
R-R Interval	Interval between heart beats (identified by R-wave) on ECG waveform
SCD	Sudden Cardiac Death
STEMI	ST-Elevated Myocardial Infarction

Magnetic Resonance Imaging

2D/3D	2/3 Dimensions
B_0	Main static magnetic field
B_1	Radio frequency magnetic field
cc-R2*	Confounder-corrected R2*
CNR	Contrast to Noise Ratio
EPI	Echo Planar Imaging
FA	Flip Angle
FOV	Field of View

GRE	Gradient Echo
IR	Inversion Recovery
mGRE	Multi-Gradient-Echo
PD	Proton Density
PDFF	Proton Density Fat Fraction
PSIR	Phase Sensitive Inversion Recovery
R2*	$1/T_2$*
RF	Radiofrequency
ROI	Region of Interest
SE	Spin Echo
SI	Signal Intensity
SNR	Signal to Noise Ratio
SPGR	Spoiled Gradient-Recalled Echo
SR	Saturation Recovery
T_1	T_1 relaxation time
T_2	T_2 relaxation time
T_2*	T_2* relaxation time
T_2*-w	T_2* weighted
TD	Delay Time
TE	Echo Time
TI	Inversion Time
TR	Repetition Time
TSE	Turbo Spin Echo

LIST OF FIGURES

LIST OF TABLES

ACKNOWLEDGEMENT

I would like to express my gratitude to my advisor Dr. Rohan Dharmakumar, who have supported, mentored, and guided me throughout my PhD program. I really appreciated the opportunity when he admitted me to his group. The passion and dedication for research of Dr. Dharmakumar has truly inspired and motivated me. Dr. Dharmakumar has provided endless resources and generous instructions for my research work which is a key to the success of my PhD program. Not only in work, his wisdom, kindness, and generosity will always deeply influence me in my life.

In addition, I would like to extend my gratitude to my doctoral committee co-chair Dr. Holden Wu, and committee members Dr. Zhaoyang, Dr. Albert M. Thomas, and Dr. Peng Hu who served as my committee during my qualify exam for their valuable advice and guidance.

I sincerely thank the entire group in Biomedical Imaging Research Institute (BIRI) at Cedars-Sinai Medical Center where I am honored to meet so many brilliant people. Special thanks go to Dr. Debiao Li who is a wonderful leader of the group but also an amiable friend. Thanks to all the faculties including but not limited to Dr. Ivan Cokic, Dr. Anthony G. Christodoulou, Dr. Zhaoyang Fan, Dr. Yibin Xie, Dr. Behzad Sharif, Dr. Damini Dey, Dr. Hui Han, Dr. Wafa Tawackoli, and Dr. Wei Gao. Thanks to Randy who was involved in all my projects and always welcomed my questions. The countless insightful discussions with you really helped me solve the difficulties I faced during my study. Thanks to my dear friends Eric and James who shared an office with me and accompanied me through the journey. Thanks to Richard who have supported me with all the animal studies at Cedars-Sinai Medical Center. Thanks to all the supporting staff at imaging core including but not limit to Laura Smith, Ed Gill, Laura Chey, Irene Lee, Jimmy Fermin, Mike Ngo, Adis Asaturyan. Thanks to our visiting scholars Dr. Guan Wang, Dr. Ting Liu and Dr. Yinyin

Chen from whom I have learned my radiology knowledge. Thanks to my fellow graduate students Dr. Nan Wang, Dr. Sen Ma, Dr. Yuhua Chen, Zhehao Hu and Pei Han for all the discussions about research and the delightful get-togethers.

Also, my sincere thanks to the Siemens support team (Dr. Xiaoming Bi and Dr. Fei Han) for their support with the pulse sequence development. Thanks to our collaborators from Lawson Health Research Institute (Dr. Frank S. Prato, Jane Sykes, John Butler) and University of Wisconsin, Madison (Dr. Scott B. Reeder and Dr. Diego Hernando).

My deepest gratitude goes to my lovely parents Wei Guan and Juan Yin who are the source of my strength and courage. I am deeply grateful for their unconditional love and support throughout my PhD program and my whole life. Last and most importantly, I would like to thank my fiancé, Siyu Chen, whose love accompanied me in every precious moment of the past three years. I love you!

VITA

EDUCATION

- M.S. Materials Science and Engineering Shanghai Jiao Tong University 2015
- B.S. Materials Science and Engineering Shanghai Jiao Tong University 2012

PUBLICATIONS

- **Xingmin Guan,** Hsin-Jung Yang, Zhehao Hu, Nan Wang, Xinheng Zhang, Anthony G. Christodoulou, Richard Tang, Jane Sykes, John Butler, Frank S. Prato, Behzad Sharif, Debiao Li, Rohan Dharmakumar. Fully ungated free-breathing high-resolution 3D cardiac T_2* imaging of intramyocardial hemorrhage. In Preparation.
- **Xingmin Guan,** Yinyin Chen, Hsin-Jung Yang, Xinheng Zhang, Daoyun Ren, Jane Sykes, John Butler, Hui Han, Mengsu Zeng, Frank S. Prato, Rohan Dharmakumar. Assessment of intramyocardial hemorrhage with dark-blood T_2*-weighted cardiovascular magnetic resonance. Journal of Cardiovascular Magnetic Resonance. 2021
- **Xingmin Guan,** Xingheng Zhang, Hsin-Jung Yang, Jane Sykes, John Butler, Frank S. Prato, Rohan Dharmakumar. On the loss of image contrast in double-inversion-recovery prepared T_2* MRI of intramyocardial hemorrhage. In preparation.
- Ivan Cokic, Anand R. Nair, **Xingmin Guan,** Hsin-Jung Yang, Ting Liu, Diego Hernando, Jane Sykes, Richard Tang, John Butler, Alice Dohnalkova, Libor Kovarik, Robert Finney, Avinash Kali, Behzad Sharif, Andrew Howarth, Andreas Kumar, Joseph Francis, Scott Reeder, John C. Wood, Frank S Prato, Rohan Dharmakumar. Intramyocardial hemorrhage drives fatting degeneration of infarcted myocardium. Under Review.
- Yinyin Chen, Daoyuan Ren, **Xingmin Guan,** Hsin-Jung Yang, Ting Liu, Richard Tang, Hao Ho, Hang Jin, Mengsu Zeng, Rohan Dharmakumar. Quantification of myocardial hemorrhage using T_2* cardiovascular resonance at 1.5T with ex-vivo validation. Journal of Cardiovascular Magnetic Resonance. 2021.
- Ahmad Abiri, Anna Tao, Meg LaRocca, **Xingmin Guan,** Syed J. Askari, James W. Bisley, Erik P. Dutson, Warren S. Grundfest. Visual–perceptual mismatch in robotic surgery. Surgical endoscopy. 2017.

- **Xingmin Guan,** Meiping Xiong, Feiyun Zeng, Bin Xu, Lingdi Yang, Han Guo, Jialin Niu, Jian Zhang, Chenxin Chen, Jia Pei, Hua Huang, Guangyin Yuan. Enhancement of Osteogenesis and Biodegradation Control by Brushite Coating on Mg–Nd–Zn–Zr Alloy for Mandibular Bone Repair. ACS Applied Materials and Interfaces, 2014.
- Jialin Niu, Meiping Xiong, **Xingmin Guan,** Jian Zhang, Hua Huang, Jia Pei, Guangyin Yuan. The in vivo degradation and bone-implant interface of Mg-Nd-Zn-Zr alloy screws: 18 months post-operation results. Corrosion Science. 2016.

SELECTED CONFERENCE ABSTRACTS

- **Xingmin Guan,** et al. Free-breathing ungated 3D cardiac T_2* MR imaging using a low-rank tensor framework. The International Society for Magnetic Resonance in Medicine, 2022.
- **Xingmin Guan,** et al. Image contrast loss in Double inversion recovery dark-blood T_2* CMR of intramyocardial hemorrhage. Society of Cardiac Magnetic Resonance, 2020.
- **Xingmin Guan,** et al. The dependence of fatty remodeling of infarct territories on iron remnants from acute myocardial infarctions: a serial CMR study. Society of Cardiac Magnetic Resonance, 2018.
- Yinyin Chen, **Xingmin Guan,** et al. Quantification of Hemorrhagic Myocardial Infarctions with T_2* CMR at 1.5T and 3.0T. Society of Cardiac Magnetic Resonance, 2020
- Guan Wang, **Xingmin Guan,** et al. Staging reperfused myocardial infarctions with T_2 CMR: insights into the dependence on infarction type with ex vivo validation. Society of Cardiac Magnetic Resonance. Society of Cardiac Magnetic Resonance, 2018.
- Ivan Cokic, **Xingmin Guan,** et al. Lipomatous metaplasia of hemorrhagic myocardial infarction is a self-perpetuating process driven by foam cell formation and iron recycling. Society of Cardiac Magnetic Resonance, 2018.
- Meiping Xiong, **Xingmin Guan,** et al. In vivo characterization of brushite coated Mg–Nd–Zn–Zr alloy for mandible bone repairing applications, European Cells and Materials, 2014, 28(Suppl. 3): 63.

Chapter 1: Introduction

1.1 Background

1.1.1 Myocardial Infarction

According to the report from American Heart Association in 2018 [1], cardiovascular disease, listed as the underlying cause of death, accounts for nearly 836,546 deaths in the US. That is about 1 of every 3 deaths in the US. Coronary heart disease (CHD) is the leading cause of deaths (>40%) attributable to cardiovascular disease which accounts for 1 in 7 deaths in the US, killing over 350 thousand people a year. The overall prevalence for myocardial infarction (MI) in the US is about 7.9 million, or 3 percent, in the US adults, which contributes significantly towards the > $200 billion in cardiac care expenditure. Between 2013 and 2030, healthcare cost associated with coronary heart disease is projected to double.

Narrowing of the coronary arteries resulting in reduced blood flow and oxygen supplied to the heart muscle is the most common form of coronary artery disease. Significant narrowing of coronary arteries, due to atherosclerotic disease or acute embolic obstruction, which impedes blood flow and oxygen to the myocardium can result in acute myocardial infarction [2]. It is well established that timely reperfusion of the infarction related artery (IRA) by thrombolytics or percutaneous coronary intervention (PCI) can significantly reduce morbidity and mortality in patient suffering from ST-elevation myocardial infarction (STEMI) [3]. Even though the use of thrombolytic therapy or PCI is the most effective strategy for reducing the size of a myocardial infarction and improving clinical outcome, the process of restoring blood flow to the ischemic myocardium, however, can induce injury, termed as ischemia-reperfusion (IR) injury [4].

1.1.2 Intramyocardial Hemorrhage

Closely associated with reperfusion injury is intramyocardial hemorrhage (IMH), where erythrocytes extravasate through severely damaged endothelial walls into the interstitial space[5]. It has been demonstrated that hemorrhage occurs in MIs with prolonged ischemia (~2 hours) followed by reperfusion [6, 7]. Hemorrhage is a consequence of microvascular injury and evolves within the MOV zone (hypointense core on LGE images) [8, 9].

Intramyocardial hemorrhage (IMH) has emerged as an important predictor of adverse long-term outcomes in patients treated with reperfusion therapy for myocardial infarction (MI) [9-13]. Notably, IMH has been associated with delayed infarct healing[14], larger MIs [15, 16], presence of persistence microvascular obstruction, higher left ventricular volumes, compromised left-ventricular ejection fraction [15, 17] and late-arrhythmogenic risk [18, 19]. This has precipitated significant clinical interest in the management of MI patients with IMH [20] and driven investigations in the pre-clinical arena focused on understanding the mechanisms contributing to the adverse outcomes.

1.2 Imaging of Intramyocardial Hemorrhage

1.2.1 Imaging of Hemorrhage

Prior to the availability of cardiac MRI, the detection of IMH had solely relied on autopsy and observational description. Only with the emergence of cardiac MRI, prognostic studies were performed. Visualization of IMH in cardiac MRI is enabled by the magnetic susceptibility changes associated with the degradation of erythrocytes. After deoxygenation, hemoglobin is broken down into oxyhemoglobin, deoxyhemoglobin and eventually methemoglobin. Deoxygenation results in the lysis of the erythrocyte membrane, which exposes the iron breakdown products, ferritin and

hemosiderin [12, 21, 22]. Iron depositions in myocardium in the form of ferritin and hemosiderin create local susceptibility-induced distortions in the static magnetic field, which accelerates the transverse magnetization decay.

The transverse magnetization decay induced by local magnetic field inhomogeneities such as those induced by IMH can be observed on both T_2 and T_2*-based images as hypointense cores [16, 21, 23, 24]. However, studies have shown that T_2*-based imaging has higher sensitivity for detection and quantifying IMH for two major reasons [25, 26]. First, the refocusing pulses in T_2-based imaging will partially reverse the loss of phase coherence induced by local magnetic field distortion, hence losing sensitivity to the presence of hemorrhage. On the other hand, edema is often associated with acute myocardial infarctions which inherently has longer T_2 relaxation than hemorrhage and myocardium, therefore appears as hyperintensity on T_2-based images. The presence of edema will counteract the signal loss imposed by IMH in T_2-based images and reduce the sensitivity of hemorrhage detection on T_2-based images. In contrast, T_2*-based imaging does not utilize refocusing radiofrequency pulses thus maximizing loss of phase coherence. Also, T_2* is relatively insensitive to edema, which together with other factors described above, has facilitated for T_2* MRI to merge as the preferred choice for characterization of IMH.

1.2.2 Cardiac T_2* MRI

T_2* relaxation is the transverse relaxation in gradient-echo sequences as a combination of T_2 relaxation (spin – spin relaxation) and relaxation caused by magnetic field inhomogeneities:

$$\frac{1}{T2^*} = \frac{1}{T2} + \gamma \Delta B_i \tag{1.1}$$

Where $\gamma \Delta B_i$ is the relaxation rate contribution attributable to field inhomogeneities (ΔB_i) across a voxel.

T_2* relaxation rate is an inherent property of any tissue or substrate which arises principally from local magnetic field irregularities. Thus, T_2* is decreased by rapid dephasing of spin coherence mediated by iron introduced microscopic B_0 field inhomogeneities.

In general, myocardial T_2* is measured using a 2D breath-held, ECG-triggered, segmented, multi-gradient-echo sequence with image acquisition at diastole. The T_2* value is derived by fitting signal intensities (SI) at different echo times (TE) to a mono-exponential equation.

$$\mathrm{SI(TE)} = \mathrm{K}e^{-\mathrm{TE}/\mathrm{T2^*}} \tag{1.2}$$

where K is a fitting constant.

Studies have shown that the inverse of T_2* ($R2^*=1/T_2^*$) is close to a linear correlation with iron concentration within a voxel [26-29]. Therefore, the extent of hemorrhage (and hence iron) can be calibrated against R2* values.

1.2.3 Quantification of Iron Overload

Evaluation of T_2* maps is often used in patients with hemochromatosis or transfusion-dependent anemia where global iron overload occurs due to excess gastrointestinal absorption or repeated blood transfusions. As a result of the human body failing to excrete excess iron stored as ferritin and hemosiderin, iron will accumulate globally across myocardium over time [24]. Myocardial iron status is best evaluated by T_2* values on T_2* maps and is a function of degrading cardiac function [24, 30-34]. Studies have shown that there is a progressive and significant decline in left ventricular ejection fraction and increase in the left ventricular end-systolic volume index, and left ventricular mass index when myocardial T_2* is below 20 ms [24], which is 2 standard deviation lower than T_2* of normal myocardium [30, 35]. Cardiac iron rises is known to rise steeply when T_2* is under 10 ms [36]. Therefore, in global iron overload diagnosis, at 1.5T, those with

myocardial T_2* over 20 ms are considered to be at low risk of the imminent development of congestive heart failure. In those with myocardial T_2* between 10 and 20 ms it is expected that cardiac iron deposition has probably occurred, and the patients are at intermediate risk of cardiac decompensation. Those with T_2* less than 10 ms are considered to be in the high-risk category of cardiac decompensation and need immediate review and intensification of chelation therapy [33]. As T_2* values decrease with increased field strength [37], the corresponding thresholds of severity of iron deposition at 3.0T are over 12 ms (low risk), between 5.5 and 12 ms (modest risk) and less than 5.5 ms (high risk) [38].

Evaluation based on T_2*-weighted images is often used in patients with IMH where focal cardiac iron coming from extravasated erythrocytes within infarcted regions. The regional and unevenly distributed iron deposition, which are visualized as hypo-intensity cores, are suitable to be characterized on T_2*-weighted images using a mean – 2SD criterion [16, 23]. In validation studies, it has been shown that IMH extent determined as the regions with signal intensity of at least 2 standard deviation less than the mean signal intensity of the remote myocardium in T_2*-weighted images is not different between in-vivo and ex-vivo setting [23]. Studies have shown that the overall T_2* values of IMH based on mean- 2SD, correlated linearly on the logarithmic scale with the amount of iron deposits from mass spectrometry [16].

Both methods, T_2* thresholds on T_2* maps and mean - 2SD criterion on T_2*-weighted images, have excellent capacity to identify myocardial iron overload. However, due to differences in pathophysiology (global vs. local deposition patterns in iron), the standards for global iron overload (T_2* < 20 ms) do not yield equivalent information as mean-2SD criterion when used for characterization of IMH. Recent studies in patients have provided clear evidence that greater clarity as they have shown that for both the mean-2SD and a T_2* threshold approach to lead to

equivalent information, a T_2* threshold of 23 ms (instead of 20 ms) should be used as cut-off for iron deposition detection [39] on T_2* maps.

For consistency, in this dissertation, all image analysis were conducted using mean - 2SD approach on T_2*-weighted images for identification of intramyocardial hemorrhage.

1.3 Need for Technical Improvements in Cardiac T_2* MRI for Imaging IMH

1.3.1 Dark-blood T_2* MRI

Cardiac T_2* imaging can be performed with either bright-blood or dark-blood. Dark-blood cardiac T_2* imaging technique has been developed and commonly used for imaging global myocardial iron overload such as thalassemia as it offered greater immunity to image artifacts [40-42]. For example, dark-blood T_2* images provide better delineation of blood pool and myocardium comparing to bright-blood T_2* images, which is beneficial in examination of global iron overload. Blood signal artifacts such as flow or partial-volume effect are reduced on dark-blood T_2* images.

The recently developed dark-blood cardiac T_2* imaging is performed with a double-inversion-recovery (DIR) preparation at R-wave [40]. The DIR preparation consists of two adiabatic inversion pulses. The first, non-selective pulse inverts all the spins into -z axis and the second, slice-selective pulse restores the spins within the slice of interest to + z axis. After the DIR preparation, inverted blood will flow into the slice of interest, replacing the restored blood. Image acquisition will be applied after a delay time when recovering blood reaches to a null signal. Hence, blood pool will appear dark on short-axis T_2* images of myocardium.

Dark-blood prepared T_2*-based cardiac MRI has also been used in imaging of IMH [18, 43, 44]. However, the tissue environment of global iron overload, compared to localized elevation in iron with IMH are very different. Compared to conventional bright-blood T_2*-based MRI, which has

been extensively used and validated [16, 45], the capability of dark-blood T_2*-based MRI in the assessment of IMH has not been investigated. Notably, it is unclear whether dark-blood T_2*-based MRI can yield equivalent diagnostic information as bright-blood T_2*-based MRI in the detection and characterization of IMH [46]. To address this issue, series of studies were performed and reported in Chapter 2 and 3 of this work.

1.3.2 Fat Infiltration

Even though the mechanism of development of adipose tissue within myocardial infarctions is unclear, fat infiltration within myocardial infarctions is a well-established phenomenon [47-51]. Studies have shown that nearly 60% of myocardial scars associated with chronic ischemic heart disease show fatty replacement [52-54]. Due to the lower electrical conductivity of fat, the presence of intramyocardial fat has been identified as a substrate for arrhythmias that drive sudden death [55-57].

1.3.2.1 Chemical Shift

Coexistence of iron and fat within an imaging voxel can confound the absolute quantification of iron and fat on T_2* images due to the chemical shifts of fat signals [58]. Chemical shift is a signal alteration that result from the inherent differences in the resonant frequencies of precessing protons due to different molecular environments of nuclei [59]. In long-chain triglycerides of fat, the ^{1}H protons are shielded by the electron cloud around them while ^{1}H protons of water are less shielded due to highly electronegative oxygen atom pulling the electron cloud away. Therefore, ^{1}H protons in fat experience a slightly weaker local magnetic field and resonate at a slightly lower frequency than nearby ^{1}H protons in water on the order of 3.4 parts per million. At 1.5T, this corresponds to an absolute frequency shift of approximately 210 Hz; and 420 Hz at 3.0T at body temperature [60-63].

1.3.2.2 MR Imaging of Water and Fat

To isolate the effects of fat protons, there have been a variety of methods developed to eliminate undesirable influence of fat by suppressing fat signal, or to quantify fat by separating fat signal based on exploiting the chemical shifts in MR imaging[51, 64-68].

In 1985, a fat-saturation technique was developed [64] by applying a 'sinc' pulse with carrier frequency centered at the main fat peak to excite all fat signals to transverse plane irrespective of their spatial location. In this scheme, prior to signal readout, all transverse magnetization of fat is spoiled by a crusher gradient, suppressing the fat signals. Fat-saturation techniques have been shown to be effective in imaging of knees but can be challenging when the field of views are larger or when there are significant B_0 and B_1 inhomogeneities [62].

Alternatively, fat suppressed MR images can be acquired by solely exciting the water peak by spatial-spectral pulses [65, 69-71]. The spatial-spectral pulses are a train of slice-selective small flip-angle excitation pulses who apart from each other with the time for fat signals to precess 180º. Therefore, magnetization of fat signals is rotated back to the z axis by the even numbered excitation pulses, while only water signals are preserved on the transverse plane. Compared to fat-saturation pulses, spectral-spatial pulses are less sensitive to B_1 inhomogeneity with smaller flip angle excitation pulse. The major drawbacks with this approach are sensitivity to B_0 inhomogeneity and lengthy sequences [62].

Since the T_1 relaxation time of fat is short (approximately 260 ms at 1.5T), the short T_1 inversion recovery (STIR) method was widely used in fat suppression MR imaging [66, 72]. Here images are acquired after an inversion pulse when the fat signals were nulled. The STIR sequence can produce uniform fat suppression with strong insensitivity to B_0 inhomogeneities but at the cost of inherent T_1-weighting and reduced signal-to-noise ratio.

Different from eliminating fat signals, a class of approaches exploiting phase differences due to chemical shifts between water and fat signals were developed to separate fat from water signals. First introduced by Dixon in 1984 [51], Dixon imaging method acquires two images at different echo times. One image is acquired at an in-phase echo time when water and fat signals are at the same direction on the transverse plane and the other image is acquired at an out-of-phase echo time when water and fat signals are at the opposite direction on the transverse plane. Therefore, water only and fat only images are easily acquired by adding or subtracting the in-phase and out-of-phase images. This method of 2-point Dixon method was advanced by adding a third echo time [73, 74] for B_0 inhomogeneity correction. Three-point Dixon approaches has been widely used to correct for water and fat in a broad range of applications [75-79].

A more advanced multi-point iterative decomposition of water and fat algorithm called IDEAL (Iterative Decomposition with Echo Asymmetry and Least squares estimation) was described more recently [67, 80]. The robustness of the approach lies in the usage of multiple arbitrary echoes to iteratively recover water and fat signals by least square estimation. Other than treating fat signals as a single peak spectrum, the IDEAL algorithm holds the advantage of integrating multiple spectral peaks of fat which is a more accurate estimation [81]. Furthermore, this multi-echo chemical-shift-based algorithm can also simultaneously evaluate the amount of iron by estimating T_2* decay within the voxel [82].

1.3.2.3 Water-fat Separation Algorithm

According to the IDEAL algorithm [82, 83], in the presence of iron, it will dominate the shortening of T_2* effect, and the water and fat components that coexist in the same voxel have similar values of T_2*. Therefore, the signals of a voxel at echo time t can be represented as:

$$S(t) = \left(W + F \cdot \left(\sum_{m=1}^{M} a_m \cdot e^{i2\pi f_m t} \right) \right) \cdot e^{-\frac{t}{T2^*}} \cdot e^{i2\pi\varphi t} + n_i \quad (1.7)$$

where $S(t)$ represents overall signal, W is water proton density, F is fat proton density, a_m is the relative amplitude of mth peak in a fat spectrum with M peaks, f_m is the chemical shift frequency of the mth peak. In this work, a seven-peak fat model with fixed frequencies and amplitudes is used [82]. φ is the frequency shift due to field inhomogeneity, and n_i represents the noise.

With the signal model described above, field map, T_2* map, water and fat signal maps can be estimated by an iterative least-squares method. From there, iron concentration can be quantified as R2* ($1/T_2$*) and proton density fat fraction (PDFF) can be calculated as:

$$PDFF = \frac{F}{F + W} \times 100\% \quad (1.8)$$

1.3.2.4 Fat-corrected IMH Imaging

The effect of chemical shift in the presence of fat can affect the quantification of iron. Studies have shown that when extent of iron overload is approximated without accounting for fat significant errors in iron content can result [84, 85]. Even though fat infiltration within myocardial infarction has been extensively studied, the role of fat in imaging IMH has not been investigated.

In this dissertation, we will employ the IDEAL approach to isolate water, fat and iron for a more accurate assessment of IMH, particularly in chronic phase of MI. Specifically, in Chapter 4 we will use simultaneous chemical-shift-based water-fat separation algorithm to study the relationship between fat and iron within hemorrhagic MI territories.

1.3.3 Motion Artifacts

The conventional T_2*-based IMH imaging is based on a 2D breath-held, ECG-triggered, segmented, multi-gradient-echo sequence. While this approach is used clinically, it has critical shortcomings. For example, acute MI patients may find breath-holding very difficult during cardiac MRI scans and unsuccessful breath-holding will lead to respiratory motion, which are visualized as ghosting artifacts on MR images. (Figure 1.1A)

Furthermore, irregular heartbeat is commonly observed in patients with acute MIs. Since conventional 2D T_2* readouts are performed during diastole when the heart is quiescent, irregular heartbeat can cause failure of ECG-gating and introduce cardiac motion in image acquisitions, which can also appear as artifacts on MR images. (Figure 1.1B)

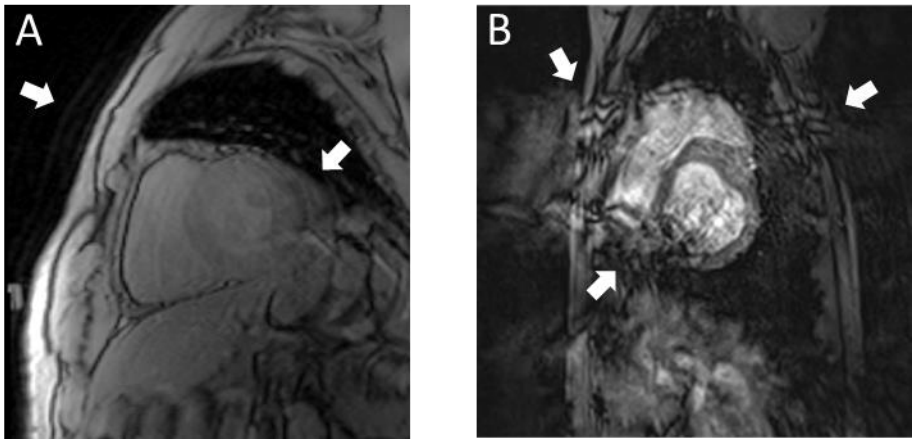

Figure 1.1. Illustration of motion artifacts in cardiac T_2* imaging. A. Cardiac T_2* image of a volunteer, TE = 1.4 ms. Ghosting artifacts are identified by arrows. **B**. Cardiac T_2* image of a dog with acute myocardial infarction, TE = 13 ms. Artifacts due to unsuccessful breathing-hold and ECG-gating are identified by arrows.

1.3.3.1 Free-breathing T_2* Imaging

Free-breathing T_2* method can be an alternative for patients who are unable to perform breath-holds. There have been two free-breathing T_2* techniques published recently. In the first approach [86], image averaging is used to acquire T_2* images with free breathing. Here single-shot multi-gradient echo images were collected at each heart beat in diastole using parallel imaging [87] combined with repeat measurements to improve signal to noise ratio and in-plane respiratory motion was corrected using non-rigid image registration [88]. In the second approach, the free-breathing T_2* mapping approach was advanced by a gradient-echo echo-planar imaging (GRE-EPI) approach [89]. Here, single-shot single-gradient-echo echo-planar images were acquired at each heartbeat at diastole and multiple T_2*-weighted (with different echo times) acquired at different heartbeats were used to construct T_2* maps. A total of 64 heartbeats were acquired for post-acquisition motion correction and improvement of signal-to-noise ratio.

Both free-breathing T_2* techniques were tested on patients referred for clinical cardiac MR and showed the capability of providing free-breathing T_2* images with good image quality and reliable T_2* measurements. However, these techniques are not adequate for acute MI patients with IMH. For example, acquiring multiple measurements for averaging, SNR improvement or motion correction all increase the overall scan time. To acquire single-shot images at each heartbeat, the acquisition matrix sizes have to be limited, which can substantially reduce spatial resolution of images. The imaging resolutions of T_2* images from these methods were $2.25 \times 3.0 \times 8.0$ mm^3 and $1.9 \times 3.1 \times 10$ mm^3, respectively. Low spatial resolution can significantly impair imaging sensitivity and accuracy in quantifying regional iron overload in patients with myocardial infarctions, where the left ventricular walls are often thin in the chronic phase of infarction.

Furthermore, these recent approaches depend on reliable ECG gating and are not robust to irregular or high heart rate which are common in MI patients.

1.3.3.2 Low-rank Tensor Framework

Despite the advancements in cardiac T_2* MRI, major technical limitations exist if they are to be used for imaging of IMH. A more recently developed cardiovascular imaging technique using a low-rank tensor framework [90-96] is a promising direction in the development of free-breathing cardiac T_2* imaging.

In conventional MRI acquisitions, redundant data is often acquired multiple times to overcome the limitations of motion. For example, in cardiac imaging, although the heart beats in a regular pattern and the shape of the heart does not change much over time, this information is captured in every k-space readout. In LRT framework [92], the correlation between the shape of the heart and its dynamics over time is exploited in a multi-dimensional cardiovascular image, which substantially reduces redundant information enabling increased efficiency, permitting continuous motion-resolved, free-breathing, non-ECG-triggered 3D acquisition.

In this framework, a cardiovascular image can be represented as a multidimensional function $I(\mathbf{x}, t_1, t_2, \dots, t_N)$ of spatial location $\mathbf{x}$ and N time dimensions $t_1, t_2, \dots, t_N$. Typical time dimensions in cardiac MRI are cardiac motion, respiratory motion, T_1, T_2 and T_2* relaxation and so on. The image I can be represented in discretized form as an (N+1)-way tensor (or multidimensional array) A with elements $A_{jkm\dots q} = I(\mathbf{x}_j, t_{1,k}, t_{2,m}, \dots, t_{N,q})$, where the first tensor dimension indexes the set of J voxel locations $\{\mathbf{x}_j\}_{j=1}^{J}$ and every remaining tensor dimension indexes one of the time dimensions. For example, if t_1 corresponds to cardiac motion, $\{t_{1,k}\}_{k=1}^{K}$

indexes K cardiac phases. With Tucker form [97] of the LRT decomposition, A can be factorized as a product of a core tensor and N+1 factor matrices:

$$\mathbf{A}_{(1)} = \mathbf{U_x G}_{(1)}\left(\mathbf{U}_{t_N} \otimes \mathbf{U}_{t_{N-1}} \otimes \ldots \otimes \mathbf{U}_{t_1}\right)^T \tag{1.3}$$

where the $\otimes$ operator denotes the Kronecker product. The subscript (n) (in this equation (1)) denotes mode-n unfolding of the tensor into a matrix. The factor matrix $\mathbf{U_x} \in \mathbb{C}^{J \times L_0}$ contains L_0 spatial basis functions with J voxels each. Each factor matrix $\mathbf{U}_{t_i}$ contains L_i basis functions for the ith time dimension t_i. $G \in \mathbb{C}^{L_0 \times L_1 \times \ldots \times L_N}$ is the core tensor governing the interaction between factor matrices. With this form, the image tensor A can then be reconstructed by LRT completion[98]:

$$\hat{A} = \arg\min_A \left\|\mathbf{d} - \Omega\left(\mathbf{FSA}_{(1)}\right)\right\|_2^2 + \lambda \sum_{n=1}^{N+1} \left\|\mathbf{A}_{(n)}\right\|_* + R(A) \tag{1.4}$$

where vector **d** is the acquired multichannel magnetic resonance signal. **S** applies coil sensitivity maps to $\mathbf{A}_{(1)}$ and **F** applies Fourier encoding operator. $\Omega(\cdot)$ is the sampling operator corresponding to samples acquired and collected in the vector **d**. λ is the rank regularization parameter, $\|\cdot\|_*$ denotes the matrix nuclear norm and $R(\cdot)$ is an optional additional regularization function that can be employed to enforce complementary image properties such as transform sparsity.

However, it is still prohibitive to directly reconstruct A due to significant computational expense. In the LRT framework [92], A can be reconstructed in factored form using an explicit tensor subspace constraint[91]:

$$\hat{\mathbf{U}}_\mathbf{x} = \arg\min_{\mathbf{U_x}} \|\mathbf{d} - \Omega([\mathbf{FSU_x}]\mathbf{\Phi})\|_2^2 + R(\mathbf{U_x}), \tag{1.5}$$

where $\mathbf{\Phi}$ is constructed from the temporal factor matrices as $\mathbf{\Phi} = \mathbf{G}_{(1)}\left(\mathbf{U}_{t_N} \otimes \mathbf{U}_{t_{N-1}} \otimes \ldots \otimes \mathbf{U}_{t_1}\right)^T$.

Since $\mathbf{\Phi}$ doesn't contain spatial information, it can be reconstructed from a frequently sampled subset of data (the 'subspace training data') acquired at the center of k-space to resolve temporal dimensions. Even though, the subspace training data is frequently sampled, it still does not cover all combination of motion states. Therefore, the subspace training data tensor χ_{tr} needs to be recovered, which can be obtained by a small-scale LRT completion:

$$\hat{\chi}_{tr} = \arg\min_{\chi_{tr}} \|\mathbf{d}_{tr} - \Omega_{tr}(\chi_{tr})\|_2^2 + \lambda \sum_{n=1}^{N+1} \left\|\mathbf{X}_{tr,(n)}\right\|_* + R(\chi_{tr}) \quad (1.6)$$

Once the tensor is completed, matrix $\mathbf{\Phi}$ can be extracted from $\hat{\chi}_{tr}$ by higher-order singular value decomposition (HOSVD)[99].

The low-rank tensor framework has been proven to be efficient for resolving motion in many cardiovascular MR imaging applications [90-96]. We will use this approach to address the key technical limitations associated with imaging of IMH. To this end, we will develop, a non-ECG-gated free-breathing 3D cardiac T_2* imaging technique using the low-rank tensor framework and validate it using animal and human studies in Chapters 5 and 6.

1.3.4 Spatial Resolution

Spatial resolution plays an important role in diagnosis of focused lesions [100, 101] such as IMH. However, it is also a critical bottleneck for 2D cardiac T_2* imaging. Spatial resolution of 2D cardiac T_2* MRI is between 1.5 × 1.5 × 6.0 mm^3 to 2.5 × 2.5 × 10 mm^3. This relatively coarse spatial resolution stems from the need to balance spatial resolution and signal-to-noise ratio (SNR) since SNR per voxel is proportional to the voxel size, if other parameters are kept constant [102]:

$$\mathrm{SNR/voxel} \propto \frac{\Delta x \Delta y \Delta z \sqrt{N_{acq} N_x N_y N_z}}{\sqrt{BW_{read}}} \quad (1.7)$$

where Δx, Δy, and Δz are voxel size in frequency encoding, in-plane phase encoding and through-plane phase encoding directions. N_{acq} represents number of averages. N_x, N_y, and N_z are encoding steps in frequency encoding, in-plane phase encoding and through-plane phase encoding directions; and BW_{read} represents readout bandwidth.

In conventional breath-held 2D cardiac T_2* imaging, the SNR of T_2* images at long echoes can be significantly low level due to T_2* decay. Hence, spatial resolution can only be improved by increasing number of acquisitions, but it requires longer image acquisition time, therefore longer breath-holding time, which is not feasible in clinical applications.

However, in a free-breathing 3D acquisition, the breath-hold time is no longer a limitation. And at the same resolution, a 3D acquisition can increase SNR by $\sqrt{N_z}$ comparing to a 2D acquisition method where slice number (N_z) is 1. Therefore, we explored the possibility of high-resolution cardiac T_2* for imaging of IMH using 3D low-rank tensor approach in Chapters 5 and 6.

1.3.5 Off-resonance Artifacts

In addition to chemical shift, motion, and spatial resolution, off-resonance artifact is another major issue in cardiac T_2* imaging. Off-resonance artifact arises from susceptibility differences between myocardium and the air in the lungs or the deoxygenated blood in large cardiac veins [103-105]. These artifacts appear as signal voids invading the myocardium at the heart-lung interface, particularly at long echoes, which can grossly overestimate iron from IMH.

To date, there has not been a way to fully eliminate susceptibility artifacts in cardiac T_2* imaging. However, it can be mitigated, for example, by image acquisition at end-expiratory breath-hold

[106]. Also, susceptibility artifacts worsen on T_2* images with long echo times therefore influence T_2* measurement, when T_2* values are high. Although moderate echo times provides some immunity, it does so at the cost of trade-off of T_2* contrast [107-109]. B_0 correction based on post-processing strategies has been reported to be instrumental in T_2* mapping of brain [110-112], but it may not be sufficient in cardiac T_2* mapping given that the B_0 field inhomogeneity around the heart is of higher order. In the contrary, advanced shimming techniques are promising alternatives in B_0 correction to solve cardiac off-resonance issues [113] but have not become commonly available.

In this dissertation, a number of measures were taken to avoid the influence of off-resonance artifact on study results: (a) T_2* images were acquired at end-expiration; (b) moderate echoes were used to avoid severe off-resonance artifacts; and (c) Left-anterior descending coronary artery occlusions were carried out in animal models to limit MIs to anterior walls, which are relatively immune to off-resonance artifacts. When off-resonance artifacts were severe, sections with off-resonance artifacts were excluded in image analysis. In addition, higher spatial resolution was also attempted to minimize signal dropouts due to intravoxel dephasing induced by off-resonance [114].

1.4 Key Objectives of the Dissertation

The broad, long-term objective of this dissertation is to improve the diagnostic capability of MRI for prognosis and therapeutic care of patients with hemorrhagic myocardial infarction. Studies performed here address three major aspects of cardiac T_2* MRI as it is used today in imaging of hemorrhagic myocardial infarctions:

First, feasibility of dark-blood T_2* has not been validated for imaging of intramyocardial hemorrhage. The dark-blood T_2* technique based on a double-inversion-recovery preparation was first developed in 2007 [40]. Dark-blood T_2* images provide better delineation of myocardium

and blood pool. It has been shown to be beneficial in the assessment of global iron overload such as thalassemia. However, the tissue environment of intramyocardial hemorrhage is very different. For example, in hemorrhagic myocardial infarctions, iron depositions are locally distributed, and the identification of hemorrhage relies on the image contrast between myocardium and the IMH regions T_2* weighted images. The feasibility of dark-blood T_2* technique in characterization of intramyocardial hemorrhage remains to be evaluated. Therefore, in Chapter 2, we investigated the performance of dark-blood T_2* in clinical assessment of intramyocardial hemorrhage with a series of pre-clinical animal studies and clinical patient studies at 1.5T and 3.0T at acute and chronic phases of MIs. Signal-to-noise ratio and contrast-to-noise ratio were compared between bright-blood and dark-blood T_2* images. IMH extent and diagnostic accuracy were evaluated on dark-blood T_2* images and compared to bright-blood T_2* images both at 1.5T and 3.0T MR systems in pre-clinical and clinical studies, with ex-vivo animal data serving as validation. In Chapter 3, we explore the biophysical mechanisms contributing to the differences in diagnostic performance between bright- and dark-blood T_2* images. We investigate whether possible signal loss from double-inversion-recovery preparation and insufficient recovery time between dark-blood preparation and image acquisition can explain the observed differences in Chapter 2. To this end, phantoms were constructed and imaged to evaluate SNR and CNR after double-inversion-recovery preparation; various delay times between double-inversion-recovery preparation and readouts were used; and in-vivo animal studies were conducted. These studies allowed us to characterize the influence of double-inversion-recovery preparation on T_2* maps.

Second, fat infiltration was identified as a confounder in quantification of iron depositions in imaging of intramyocardial hemorrhage. Even though the mechanisms of fatty remodeling are still unclear, fat infiltration is a well-established, common phenomenon in chronic myocardial

infarctions. The presence of fat within hemorrhagic myocardial infarctions may confound T_2* fittings due to chemical shifts by protons in fatty tissues. However, it has been overlooked in the quantification of iron deposition in myocardial infarctions. In Chapter 4, studies were performed to evaluate the influence of fat infiltration on T_2* fitting when quantifying iron overload in chronic hemorrhagic MIs. A confounder-corrected water-fat separation algorithm was used to separate signals from fat and iron. Fat infiltration was evaluated through serial imaging of animals with and without hemorrhagic MIs. Regressions between fat infiltration and iron deposition was performed to evaluate association between the two components in hemorrhagic MIs. Simulations were performed to better understand chemical shifts induced T_2* fitting errors. R2* maps of intramyocardial hemorrhage were generated by two different methods: one with direct fitting of multi-gradient-echo images with different T_2* weighting; and the other generated from the chemical-shift-based water-fat separation algorithm. R2* values measured from different R2* maps were compared to identify chemical shift induced T_2* fitting error.

Third, technical challenges resulting from motion artifacts and limited spatial resolution of cardiac T_2* MRI were addressed in Chapter 5 and 6. Hemorrhagic myocardial infarctions lead to significant depletion of cardiac function. Patients with hemorrhagic MIs often have difficulties with holding their breath and experience arrhythmias during cardiac MR exams, both of which can cause artifacts in T_2* images. To address this critical issue, a 3D fully ungated free-breathing motion-resolved cardiac T_2* technique was developed based on a low-rank tensor framework. The proposed 3D LRT T_2* imaging approach was tested and validated in healthy volunteers and animals for image quality, signal-to-noise ratio, T_2* values in Chapter 5. Spatial resolution is also a common limitation in conventional 2D cardiac T_2* imaging, especially in the diagnosis of focused lesions such as IMH which is known to lead to myocardial wall thinning. Thus, limitations

in spatial resolution plays an important role in the diagnostic accuracy of T_2* cardiac MRI in the setting of hemorrhagic MIs. However, due to the proportional relationship between voxel size and signal-to-noise ratio, spatial resolution in conventional breath-held 2D cardiac T_2* imaging is very limited. A key benefit of a 3D free-breathing acquisitions is that image resolution can be improved, which is demonstrated in Chapter 5 using high-resolution, fully ungated 3D LRT T_2* approach. Image quality, SNR and T_2* measurements were evaluated on high-resolution LRT T_2* data comparing to conventional 2D breath-holding, ECG-gating cardiac T_2* images. In Chapter 6, the 3D LRT T_2* imaging technique developed in Chapter 5 was tested and validated in a large animal model of hemorrhagic MI. One set of LRT data was acquired with the same resolution as conventional 2D T_2* images, and another high-resolution LRT data was acquired with smaller slice thickness. Image quality, SNR, CNR, IMH extent and T_2* estimates were examined on both conventional (2D T_2*) and proposed (3D LRT T_2*) images. Diagnostic accuracy of conventional 2D T_2* and proposed 3D LRT T_2* imaging approaches was evaluated with ex-vivo T_2* images serving as ground truth.

Chapter 2: Assessment of Intramyocardial Hemorrhage with Dark-Blood T_2*-weighted Cardiac MRI

2.1 Introduction

Well before the strengths of T_2*-based MRI was recognized for IMH detection, T_2*-based cardiac MRI had become important in the standard of care in patients with global myocardial iron overload diseases such as thalassemia [24]. In this setting, T_2*-based MRI was originally performed with bright-blood approaches (with blood in LV chamber appearing bright), but later magnetization-prepared dark-blood T_2*-based cardiac MRI became common as it offered greater immunity to image artifacts [40-42]. More recently, this notion has also led to the use of dark-blood prepared T_2*-based cardiac MRI for the examination of IMH in MI patients [18, 43, 44]. However, the tissue environment of global iron loading and hemorrhagic MI are very different – unlike global iron overloading disorder, in hemorrhagic MI, there is gross increase in edema, localized wall motion abnormalities and only spatially localized increases in iron concentration. Given these differences, it is unclear whether dark-blood T_2*-based MRI can yield equivalent diagnostic information as bright-blood T_2*-based MRI in the detection and characterization of IMH. We hypothesized that dark-blood T_2*-weighted images do not provide equivalent information as bright-blood T_2*-weighted images with respect to assessment of IMH. We tested our hypothesis by performing a head-to-head comparison between bright- and dark-blood T_2*-weighted MRI in ST-elevation MI patients and validated large animal models with IMH in the acute and chronic phases of MI at 1.5T and 3.0T.

2.2 Methods

Both the clinical and animal studies were planned, prospective and randomized as described belo**w.**

2.2.1 Clinical Studies

Patient studies were approved by Institutional Review Boards. Following written informed consent, ST-elevation MI patients (n = 29) were enrolled consecutively after successful primary percutaneous coronary intervention (PCI). Patients were randomized for cardiac MRI at 1.5T (n = 14) or 3.0T (n = 15). Subsequently the patients underwent MRI scans in the acute phase of MI (7-10 days post MI). Patients (n = 20) with evidence of IMH on bright-blood T_2* MRI were followed up at 6-months post MI with a second MRI. MRIs were performed on 1.5T (Aera) or 3.0T (Verio) MRI systems (Siemens Healthcare, Erlangen, Germany). Following localizers and whole-heart shimming, slice-matched short-axis T_2*-weighted acquisitions were performed. All scans were terminated with late-gadolinium enhancement (LGE) cardiac MRI. T_2*-weighted images were acquired using gradient-recalled acquisitions. Dark-blood T_2*-weighted images were acquired with double-inversion-recovery (DIR) preparation applied at the R-wave. All T_2*-weighted images were acquired at mid diastole with 7-9 phase encoding lines per heartbeat to minimize motion artifacts. **1.5T**: T_2*-weighted MRI – number of segments = 9; TR / TE = 1 R-R interval / 14.5 ms; flip angle = 18°; bandwidth = 814 Hz/pixel; spatial resolution = 2.0x2.0x8.0 mm^3; GRAPPA accelerate factor = 2; slice thickness of dark-blood preparation = 200%; inversion time between double-inversion recovery pulses (DIR) and readout were between 550 to 700 ms, depending on heart rate. Segmented breath-held LGE images were acquired 10-min post-injection of 0.15mmol/kg gadolinium contrast agent (Magnevist; Bayer AG, Berlin, Germany) using segmented phase-sensitive inversion recovery (PSIR) reconstruction with gradient-recalled-echo readouts (TR / TE = 1 R-R interval / 3.2 ms, flip angle = 25°, bandwidth = 140 Hz/pixel, and

spatial resolution = 1.3x1.3x8.0 mm^3). **3.0T**: T_2*-weighted MRI – number of segments = 9; TR / TE = 1 R-R interval / 12.7 ms; flip angle = 10°; bandwidth = 1030 Hz/pixel; spatial resolution = 1.6x1.6x8.0mm^3; GRAPPA accelerate factor = 2; and slice thickness of dark-blood preparation = 200%; inversion time between double-inversion recovery pulses (DIR) and readout = 550 to 700 ms, depending on heart rate. LGE images were acquired with TR / TE = 1 R-R interval / 1.6ms; flip angle 20°; bandwidth = 465 Hz/pixel; and spatial resolution = 1.6x1.6x8.0 mm^3. T

2.2.2 Preclinical Studies

According to the protocol approved by the Institutional Animal Care and Use Committee, hemorrhagic MIs were created in canines (n = 11, all female) by occluding the left-anterior descending coronary artery (LAD) for 3 hours, followed by reperfusion [16]. Prior to MRI scans, all animals were intubated and anesthetized with isoflurane (1-1.5 %/volume). All animals were studied in a 3.0T MR system (Verio, Siemens Healthcare, Erlangen, Germany) in the acute phase (7 days post reperfusion) and in the chronic phase (>2 months post reperfusion). A subset of animals (n = 8) were also studied at 1.5T (Aera, Siemens Healthcare, Erlangen, Germany) in the acute phase and the chronic phases post MI. Slice-matched, breath-held, ECG triggered, bright-blood T_2*-weighted and DIR-prepared dark-blood T_2*-weighted images were acquired. All T_2*-weighted images were acquired at mid diastole with 7-9 phase encoding lines per heartbeat to minimize motion artifacts. At 1.5T, T_2*-weighted images were acquired with TR / TE = 1 R-R interval / 14.4 ms; segments = 7; flip angle = 20°; bandwidth = 815 Hz/pixel; and spatial resolution = 1.1x1.1x6.0mm^3; GRAPPA accelerate factor = 2; slice thickness of dark-blood preparation = 200%, inversion time between double-inversion recovery pulses (DIR) and readout = 500 to 700 ms. Scan parameters for LGE were TR / TE = 1 R-R interval / 3.3ms, flip angle = 20°, bandwidth = 235 Hz/pixel, spatial resolution = 1.1x1.1x6.0mm^3. At 3.0T, T_2*-weighted images were acquired

with TR / TE = 1 R-R interval / 11.5 ms; segments = 7; flip angle = 18°; bandwidth = 925 Hz/pixel; and spatial resolution = 1.1x1.1x6.0mm^3; GRAPPA accelerate factor = 2; slice thickness of dark-blood preparation = 200%, inversion time between double-inversion recovery pulses (DIR) and readout = 500 to 700 ms. LGE images were acquired at 3T with TR / TE = 1 R-R interval / 2.1 ms, flip angle = 20°, bandwidth = 287 Hz/pixel, spatial resolution = 1.1x1.1x6.0mm^3.

Following MRI scans in the chronic phase, animals were euthanized, hearts were explanted. Two of the hearts were cut into 10-mm-thick short axis rings and stained with triphenyltetrozolium chloride to delineate infarcted area for histology analysis. Hematoxylin-eosin and Perl staining were performed in representative samples of infarcted and remote myocardium to identify tissue damage and iron deposition, respectively. Nine of the hearts were fixed in 10% formalin solution and scanned at 3.0T for ex-vivo imaging. 3D T_2*-weighted images were acquired with spatial resolution = 1.0x1.0x1.5mm^3.

2.2.3 Image Analyses

Hemorrhage Detection: All image analyses were performed with CVI[42] (Circle Cardiovascular Imaging, Calgary, Alberta, Canada) by two expert readers and the results were averaged unless stated otherwise. Remote myocardium was identified as the region absent of hyperintensity on LGE images. MI zone was defined as the region with mean signal intensity (SI) of at least 5 standard deviations (SD) greater than that of a reference region of interest (ROI) drawn in remote myocardium [115]. MI zones were identified to be hemorrhagic if there were hypointense cores within MI on the bright-blood T_2*-weighted images (TE = 14.5 ms (patients) 14.4 ms (animals) at 1.5T and 12.7 ms (patients) and 11.5 ms (animals) at 3.0T) with a mean signal intensity 2-SD lower than that of the reference ROI in the remote myocardium [16, 23]. A TE of ~14 ms at 1.5T and ~12 ms at 3.0T were chosen to balance the image contrast and image artifacts based on

previous reports [16, 116]. Volume of IMH in each heart measured from T_2*-weighted images were normalized by the volume of myocardium and reported as IMH Extent.

Signal Characteristics: Signal intensity (SI) values of IMH regions and remote myocardium determined from T_2*-weighted images were used to compute signal-to-noise ratio (SNR), contrast-to-noise ratio (CNR) as:

$$\mathrm{SNR} = \frac{\mathrm{SI}_{\mathrm{remote}}}{\sigma_{\mathrm{air}}}, \tag{2.1}$$

$$\mathrm{CNR} = \frac{\mathrm{SI}_{\mathrm{remote}} - \mathrm{SI}_{\mathrm{IMH}}}{\sigma_{\mathrm{air}}}, \tag{2.2}$$

where $\mathrm{SI}_{\mathrm{remote}}$ is the mean intensity of remote myocardium, $\mathrm{SI}_{\mathrm{IMH}}$ is mean intensity of IMH region and σ_{air} is the SD of signal intensity of background air.

Relative SNR and Relative CNR were computed and reported as:

$$\text{Relative SNR} = \frac{\mathrm{SNR}_{\mathrm{DB}}}{\mathrm{SNR}_{\mathrm{BB}}} \times 100\%, \tag{2.3}$$

$$\text{Relative CNR} = \frac{\mathrm{CNR}_{\mathrm{DB}}}{\mathrm{CNR}_{\mathrm{BB}}} \times 100\%, \tag{2.4}$$

where $\mathrm{SNR}_{\mathrm{DB}}$ and $\mathrm{SNR}_{\mathrm{BB}}$ are signal-to-noise ratio determined from dark-blood (DB) and bright-blood (BB) T_2*-weighted images respectively. $\mathrm{CNR}_{\mathrm{DB}}$ and $\mathrm{CNR}_{\mathrm{BB}}$ are contrast-to-noise ratio determined from dark-blood and bright-blood T_2*-weighted images respectively. Coefficient of variations (COV) were computed as:

$$\mathrm{COV} = \frac{\sigma}{\mathrm{SI}}, \tag{2.5}$$

where SI is the mean signal intensity of the region of interest, and σ is the SD of signal intensity of region of interest.

2.2.4 Diagnostic Performance

Sensitivity and specificity of dark-blood T_2*-weighted images for detection of IMH for each subject were determined with bright-blood T_2*-weighted images serving as the ground truth. All bright-blood T_2*-weighted images positive for IMH were segmented according to the recommendation of American Heart Association (AHA). Segments were considered positive for IMH if the hypointense area exceeded 1% of the cross-sectional area of the segment. Segments affected by off-resonance, particularly near the heart-lung interface, were manually excluded. Accuracy was computed as a quotient of number of true positives and true negatives normalized by the total number of segments evaluated. The interobserver variability in IMH Extent was determined based on the independent assessment by the two expert readers.

2.2.5 Statistical Analyses

Statistical analysis was performed using IBM SPSS Statistics 23 (IBM Corp., Armonk, New York). Normality of continuous data was determined by using the Shapiro-Wilk test and quantile-quantile plots. Normally distributed variables were compared using repeated measures ANOVA. Repeated measures from each heart were nested for analysis. Pairwise comparisons for normal data were performed using paired t-test, and for non-normal data were performed using the Mann-Whitney U test. Inter-observer reliability in measuring IMH Extent was determined using intraclass correlation coefficient. Bland-Altman analysis of IMH Extent determined using dark- and bright-blood T_2*-weighted images was performed to determine the bias in measurements. IMH Extent determined using bright-blood T_2*-weighted images and using ex-vivo T_2*weighted images were regressed against one another to validate accuracy of in-vivo bright-blood T_2*-weighted images. Statistical significance was set at $p<0.05$.

2.3 Results

From the 29 patients undergoing MRI following acute MI, a total of 20 patients (17 male, 34-65 years, 58 to 92 kg) were identified to be positive for IMH and 10 patients were assigned to the 1.5T group and the remaining 10 were assigned to the 3.0T group. At the 6-month follow up, the same 10 patients were studied at 1.5T and 9 at 3.0T. From the 1.5T studies, 31 slices were positive for IMH in the acute phase and 21 were positive for iron in the chronic phase. From the 3.0T studies, 28 slices were positive for IMH in the acute phase and 17 were positive for iron in the chronic phase. A few slices were discarded from further analysis due to off-resonance artifacts (1.5T: 3 in acute phase and 2 in chronic phase; and at 3.0T: 1 slice from acute phase; none from chronic phase).

Table 2.1. Clinical features of patients (n = 20).

Parameter	1.5T (n = 10)	3.0T (n = 10)
Age	55 (34 – 65)	54 (42 – 65)
Male Sex	9	8
Weight (kg)	68.5 (58 – 82)	70.9 (61 – 85)
Infarct-related coronary artery	LAD (n = 8)	LAD (n = 7)
	LCX (n = 0)	LCX (n = 2)
	RCA (n =2)	RCA (n =1)
Time to reperfusion (hrs), median (IQR)	7.5 (4 – 18)	6.0 (4 – 8)
Modality of reperfusion	PCI (n =10)	PCI (n = 10)
Heart rate (beats per minute)	84 (64 – 90)	85 (75 – 108)
Antiplatelet medication	10	10

MVO volume (%LV)	9.1 ± 6.3	7.5 ± 5.8

All animals survived hemorrhagic MI and were studied at 3.0T (n = 11), and a subset of the same animals were also studied at 1.5T (n = 8). From the 1.5T studies, 27 slices were positive for IMH in the acute phase and 21 slices were positive for iron in the chronic phase. From the 3.0T data sets, 39 slices were positive for IMH in the acute phase and 29 were positive for iron in the chronic phase. From these data sets, 1 slice from acute phase was removed from further analysis due to off-resonance artifacts at 3.0T.

2.3.1 Case Examples

Representative bright- and dark-blood T_2*-weighted and LGE images acquired at 1.5T and 3.0T in the acute and chronic phases in patients with hemorrhagic MI are shown in Figure 2.1. Note that although the IMH region is accurately identified (as the region with mean signal intensity at least 2-SD lower than that of remote myocardium) in the dark-blood T_2*-weighted image, in relation to the bright-blood T_2*-weighted image, the extent of hemorrhage is visually smaller independent of MI age or field strength.

Representative bright- and dark-blood T_2*-weighted and LGE images acquired at 1.5T and 3.0T in the acute and chronic phases in canines with hemorrhagic MI are shown in Figure 2.2. Similar to the patient data in Figure 2.1, the extent of IMH is significantly smaller in dark-blood images independent of MI age and imaging field strength.

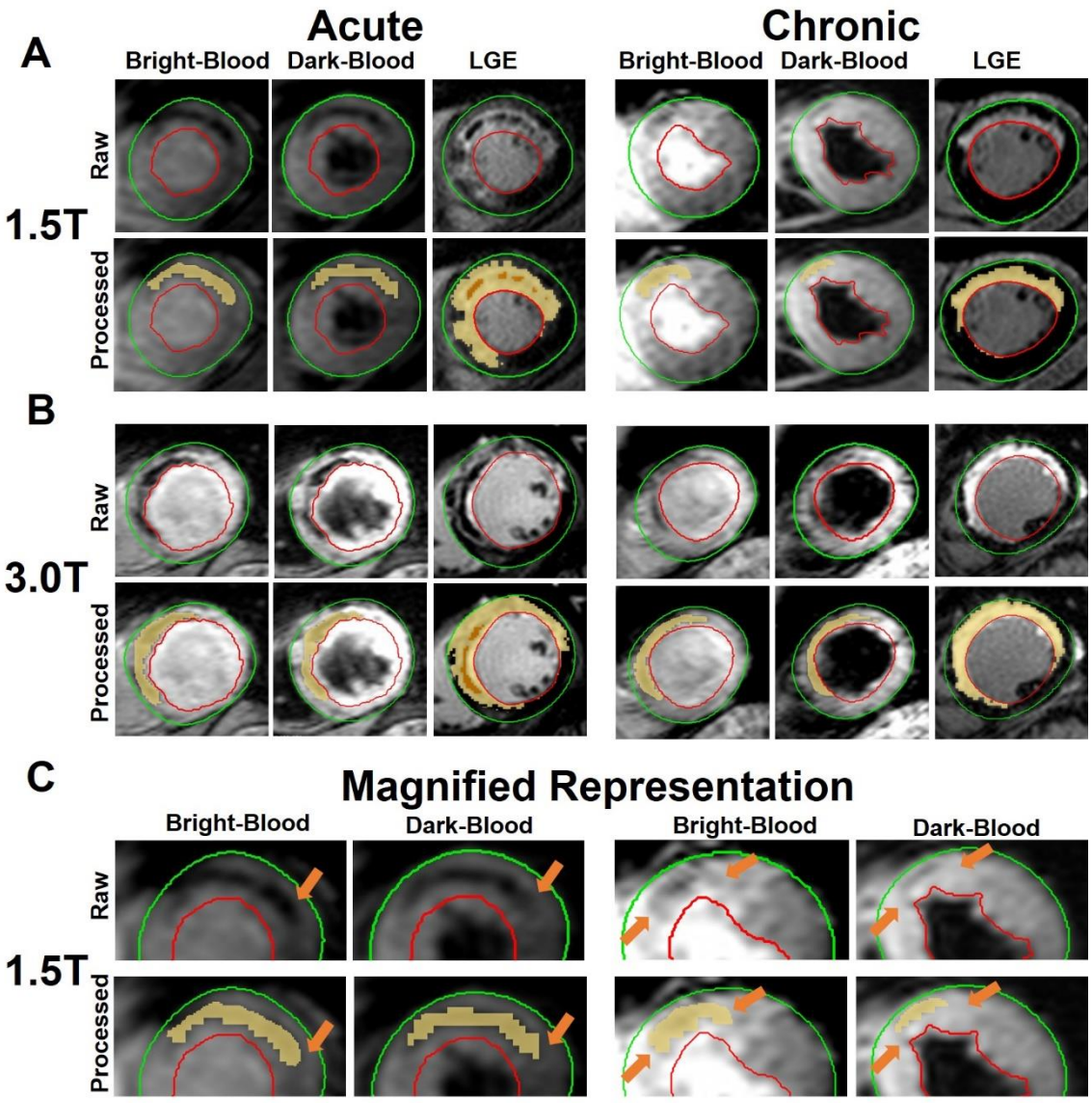

Figure 2.1. Bright-blood vs. Dark-blood T_2*-weighted MRI in Hemorrhagic MI Patients. Representative bright- and dark-blood T_2*-weighted and LGE images acquired from patients with hemorrhagic MIs in the acute and chronic phases of MI at 1.5T (55-year-old male; Panel **A**) and 3.0T (42-year-old male; Panel **B**) are shown. Panel **C** is magnified representation of the IMH detected on bright-blood and dark-blood T_2*-weighted images at 1.5T in acute and chronic phases. Arrows point to the regions where hypo-intensity is seen in bright-blood but not in dark-blood images.

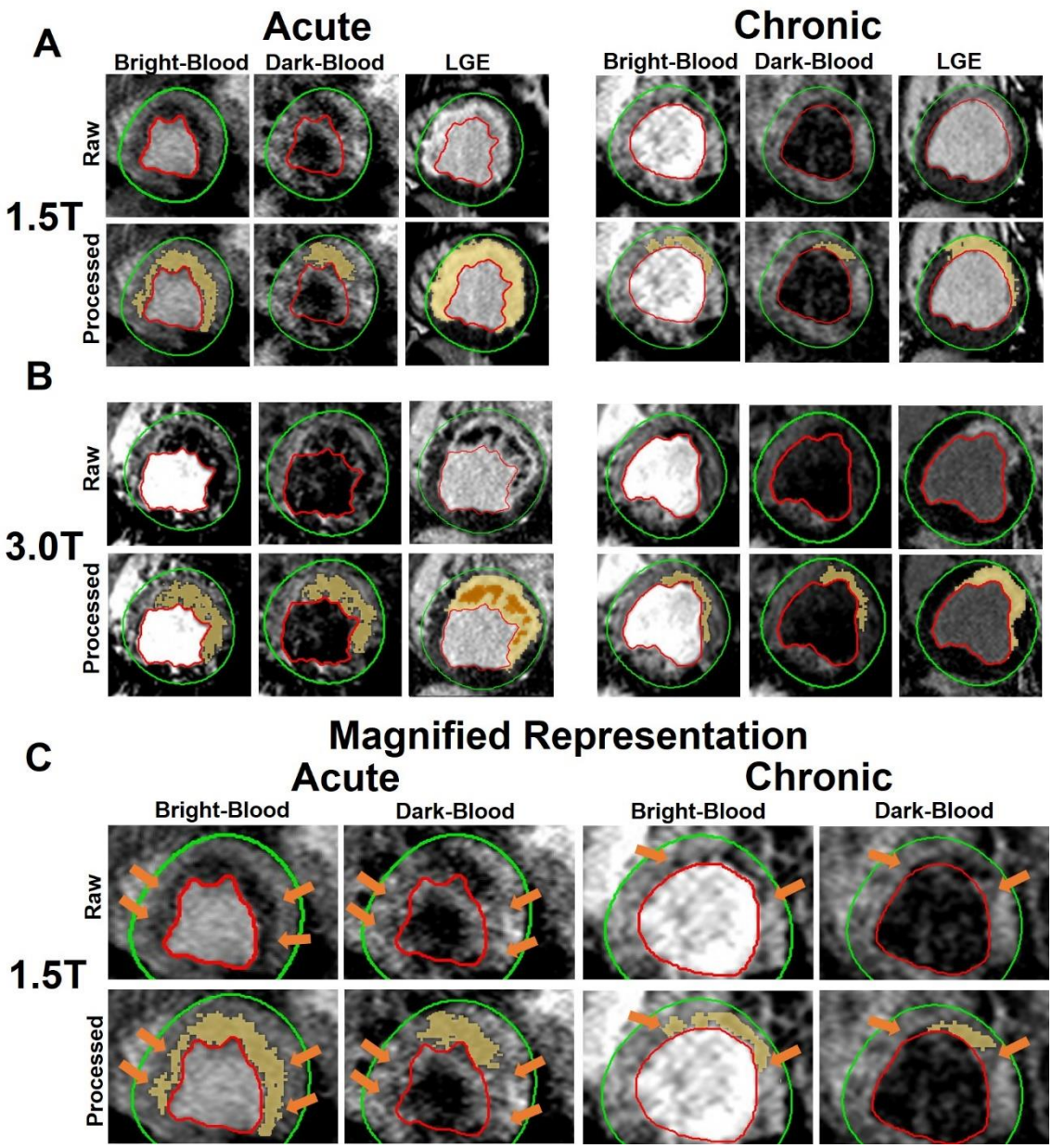

Figure 2.2. Bright-blood vs. Dark-blood T_2*-weighted MRI in Canines with Hemorrhagic MI. Representative bright- and dark-blood T_2*-weighted and LGE images from canines with hemorrhagic MI in the acute and chronic phase of MI at 1.5T (Panel **A**) and 3.0T (Panel **B**) are shown. Both raw and processed (details in text) images are shown with the processed images delineating the regions of hemorrhage (T_2*-weighted images) and MI (LGE) territories. Panel **C** is magnified representation of the IMH detected on bright-blood and dark-blood T_2*-weighted images at 1.5T in acute and chronic phases. Arrows point to the regions where hypo-intensity is seen in bright-blood but not in dark-blood images.

2.3.2 Relative SNR, Relative CNR and COV

The appearance of hemorrhage was evidenced as hypointense core on both bright- and dark-blood T_2*-weighted images at 1.5T and 3.0T, in the acute and chronic phases of MI. Relative SNR, relative CNR and COV relations between dark- and bright-blood T_2*-weighted images are shown in Figure 2.3.

Mean relative SNR of remote myocardium from bright- and dark-blood T_2*-weighted images at 1.5T and 3.0T in the acute and chronic phases of MI are shown in Figure 2.3 (panels A and C). The relative SNR of remote myocardium between the dark-blood and bright-blood T_2*-weighted images were 76.6 ± 11.8% ($p<0.05$) in acute phase and 79.7 ± 12.7% ($p<0.05$) in chronic phase at 1.5T. At 3.0T, the relative SNR between the dark-blood and bright-blood T_2*-weighted images was even lower (acute phase: 60.0 ± 9.1%, $p<0.05$; chronic phase: 64.2 ± 10.0%, $p<0.05$). Similar observations were evident in animals as well (Figure 2.3, panels E and G). Relative SNR values were 69.1 ± 9.9% ($p<0.05$) in acute phase and 77.2 ± 10.5% ($p<0.05$) in chronic phase at 1.5T. And at 3.0T, relative SNR in acute phase is 62.3 ± 10.2% ($p<0.05$), in chronic phase is 66.2 ± 10.1% ($p<0.05$).

Mean relative CNR between IMH and remote myocardium at 1.5T and 3.0T in patients are shown in Figure 2.3 (panels A and C). Compared to bright-blood T_2*-weighted images, dark-blood T_2*-weighted images showed significantly lower CNR at 1.5T. Relative CNR values are 74.7 ± 13.1% ($p<0.05$) in acute phase and 84.1 ± 12.6 % ($p<0.05$) in chronic phases of MI. Similar observations were found at 3.0T as well, with relative CNR values are 63.1 ± 15.8% ($p<0.05$) in the acute and 70.3 ± 9.6 % ($p<0.05$) in the chronic phases of MI. Results from animals (Figure 2.3 panels E and G) were consistent with patient studies. In animals, the relative CNR at 1.5T was 77.9 ± 15.8 %

($p<0.05$) in acute phase; and 78.8 ± 17.3 % ($p<0.05$), in chronic phase; and at 3.0T, 59.8 ± 12.2 % ($p<0.05$) in acute phase; and 71.4 ± 14.4 % ($p<0.05$) in chronic phase.

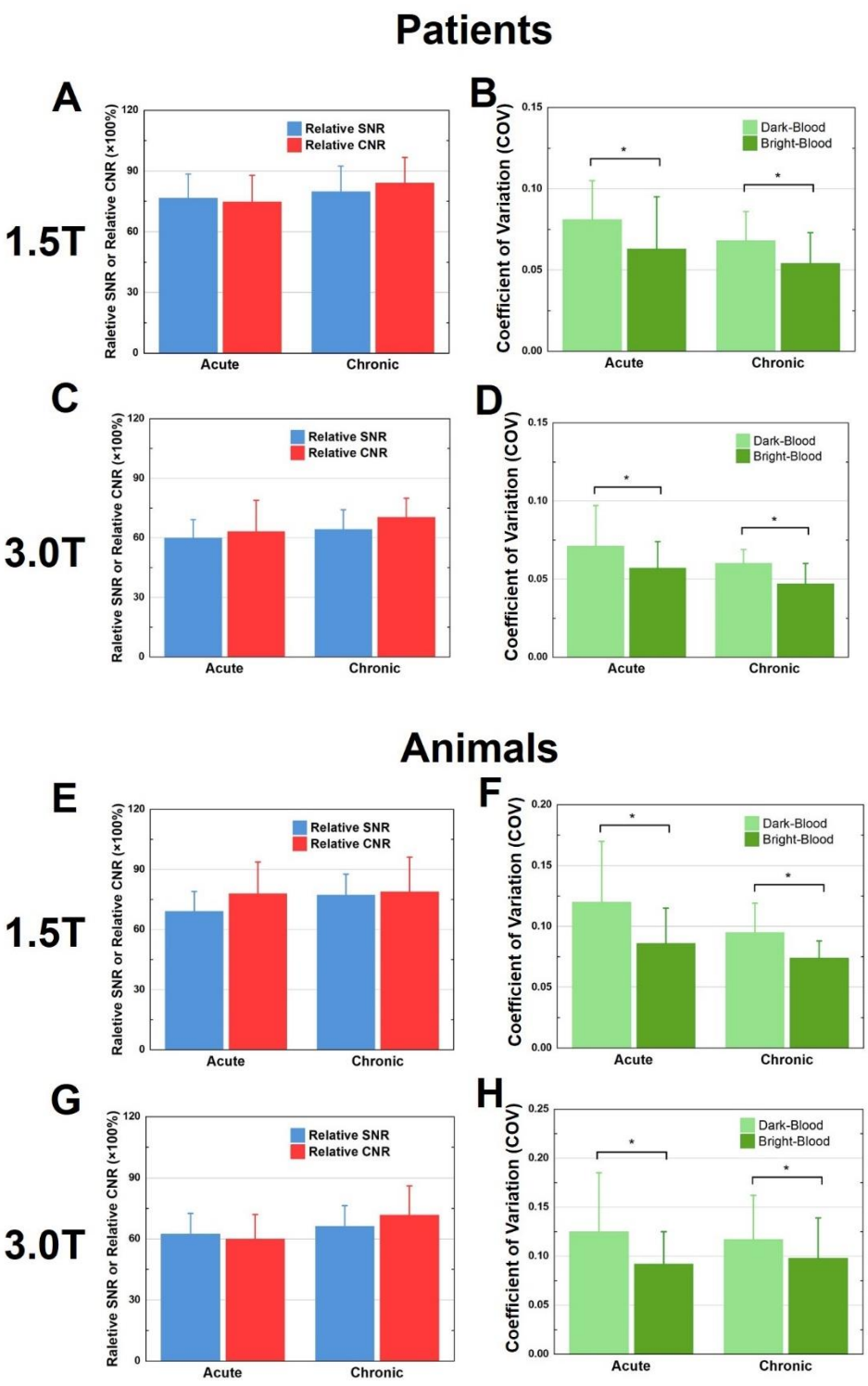

Figure 2.3. Effect of Dark-Blood Magnetization Preparation on T_2*-weighted Signal Characteristics. Relative SNR, Relative CNR and COV (definitions in text) computed from T_2*-weighted images in patients at 1.5T (Panels A and B, respectively) and 3.0T (Panels C and D, respectively) and animals at 1.5T (Panels

E and F, respectively) and 3.0T (Panels G and H, respectively) in the acute and chronic phases of hemorrhagic MI are shown. All Relative SNR and Relative CNR were found to be less than 100 ($p<0.05$); and * denotes that the measures being compared are statistically different ($p<0.05$).

COV of remote myocardium at 1.5T and 3.0T in patients are shown in Figure 2.3 (panels B and D). COV was higher in dark-blood T_2*-weighted images than that on bright-blood T_2*-weighted images in general. At 1.5T, COV was 32.1 ± 65.0 % ($p<0.05$) and 27.1 ± 55.1 % ($p<0.05$) higher on dark-blood T_2*-weighted images in acute and chronic phase respectively. At 3.0T, COV was 26.5 ± 30.2 % ($p<0.05$) greater in the acute phase and 38.7 ± 52.3 % ($p<0.05$) greater in the chronic phase of MI. Similar results were found in animals (Figure 2.3, panels F and H). COV was 49.4 ± 65.2% ($p<0.05$) greater on dark-blood T_2*-weighed images than that on bright-blood T_2*-weighted images in the acute phase of MI and 33.0 ± 41.8% ($p<0.05$) greater in the chronic phase of MI at 1.5T. At 3.0T, COV increased by 35.6 ± 40.0% ($p<0.05$) in the acute phase and by 37.0 ± 55.3% ($p<0.05$) in the chronic phase of MI.

2.3.3 Quantification of IMH Extent

Consistent with the reduction in SNR and CNR and amplification on COV of the remote myocardium, IMH Extent was significantly smaller on dark-blood T_2*-weighted images compared to bright-blood T_2*-weighted images (Figure 2.4), independent of field strength or age of MI in both patients and animals. In patients at 1.5T, IMH Extent in dark-blood T_2*-weighted was reduced by 18.7 ± 12.9% ($p<0.05$) in acute phase and by 12.7 ± 8.1% ($p<0.05$) in the chronic phase of MI relative to bright-blood T_2*-weighted images. At 3.0T, the IMH Extent on dark-blood T_2*-weighted images were reduced by 21.6 ± 11.8% ($p<0.05$) in the acute phase and by 17.4 ± 12.6% ($p<.05$) in the chronic phase compared to bright-blood T_2*-weighted images. In animals, at 1.5T, IMH Extent measured from dark-blood T_2*-weighted images were reduced by 30.2 ± 13.1%

($p<0.05$) and by 23.2 ± 11.0% ($p<0.05$) compared the corresponding bright-blood T_2*-weighted images in the acute and chronic phases, respectively. At 3.0T, the IMH Extent on dark-blood T_2*-weighted images were reduced by 21.3 ± 6.9% ($p<0.05$) in the acute phase and 20.6 ± 12.1% ($p<0.05$) in the chronic phase compared to the corresponding bright-blood T_2*-weighted images.

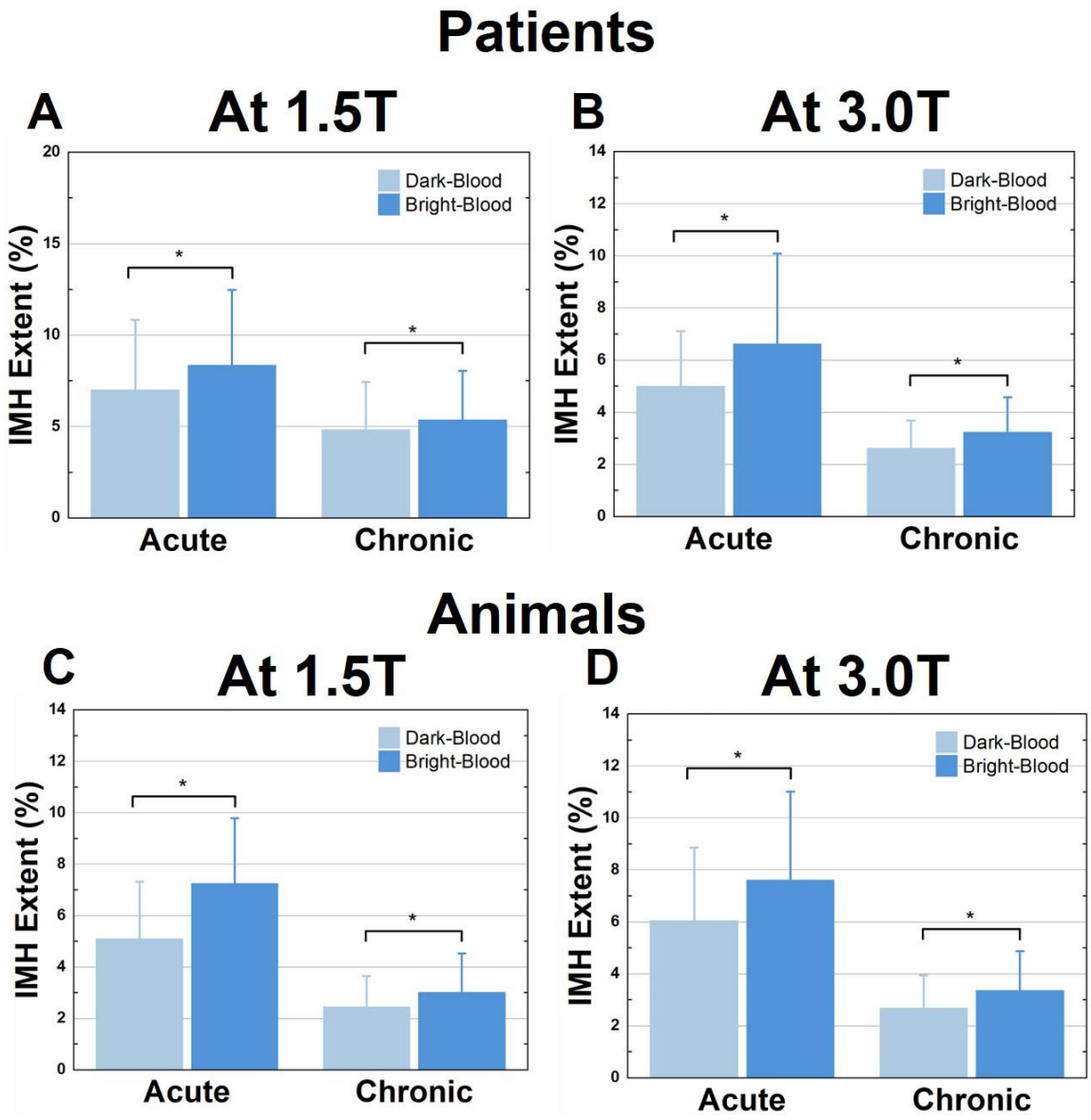

Figure 2.4. Impact of Dark-Blood Preparation on IMH Extent Determined from T_2*-weighted MRI in Patients and Animals. IMH Extent in patients is underestimated by dark-blood-prepared T_2*-weighted images at 1.5T and 3.0T (Panels A and B, respectively). IMH Extent in animals is underestimated by dark-

blood-prepared T_2*-weighted images at 1.5T and 3.0T (Panels C and D, respectively). *denotes statistically significant difference ($p<0.05$) between bright- and dark-blood images.

Bland-Altman analysis (Figure 2.5) showed a modest bias between the IMH Extent between the two approaches as well. An average of bias of 1.3 ± 0.7% were found between dark-blood and bright-blood T_2*-weighted images of IMH Extent at 1.5T in acute phase of MI and 0.5 ± 0.2% in chronic phase of MI in patients. At 3.0T, the bias is 1.6 ± 1.6% in acute phase and 0.6 ± 0.6% in chronic phase of MI. In animal studies, bias of IMH Extent determined from bright- and dark-blood T_2*-weighted images is 2.2 ± 1.3% in acute phase and 0.6 ± 0.5% in chronic phase at 1.5T, and 1.5 ± 0.6% in acute phase and 0.6 ± 0.3% in chronic phase of MI at 3.0T.

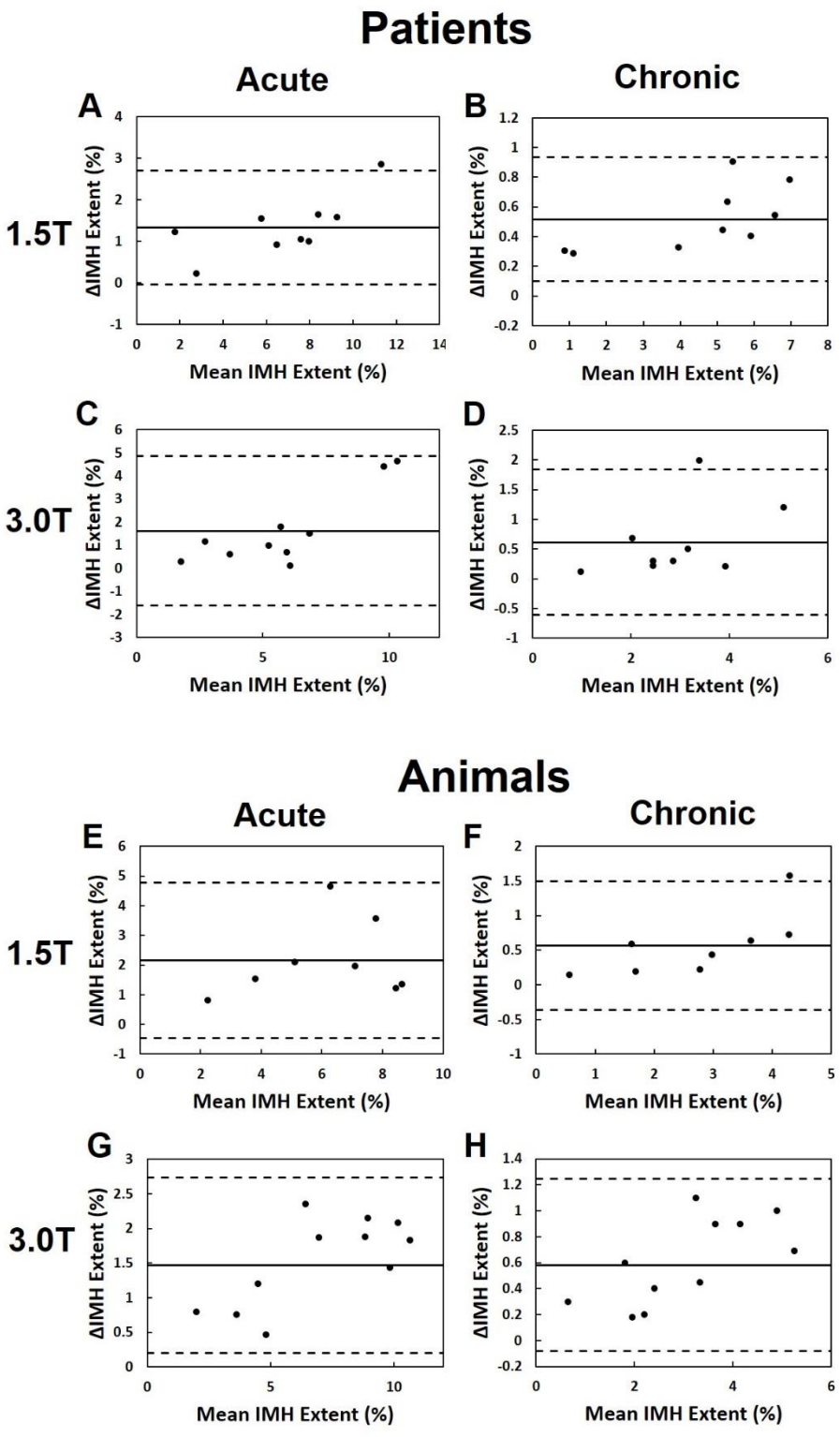

Figure 2.5. Bland-Altman plots of IMH Extent Determined from Bright- and Dark- Blood T_2*-weighted MRI in Patients and Animals. Moderate bias in IMH Extent was found between bright- and

dark- blood T_2*-weighted images in patients and animals at 1.5T and 3.0T in the acute and chronic phases of MI.

2.3.4 Qualitative Observations

Example bright- and dark-blood T_2*-weighted and LGE images obtained from an infarcted animal with IMH in the acute and chronic phase of MI are shown in Figure 2.6. A common observation in dark-blood T_2*-weighted images (as visualized in Figure 2.6) was the appearance of stagnant blood obscuring the boundary between blood and myocardium, likely from compromised contraction of the infarct wall. Another key difficulty observed with dark-blood T_2*-based imaging is that IMH appearing hypointense makes it difficult to visually appreciate the presence of IMH (or residual iron) when it is found in the subendocardial wall.

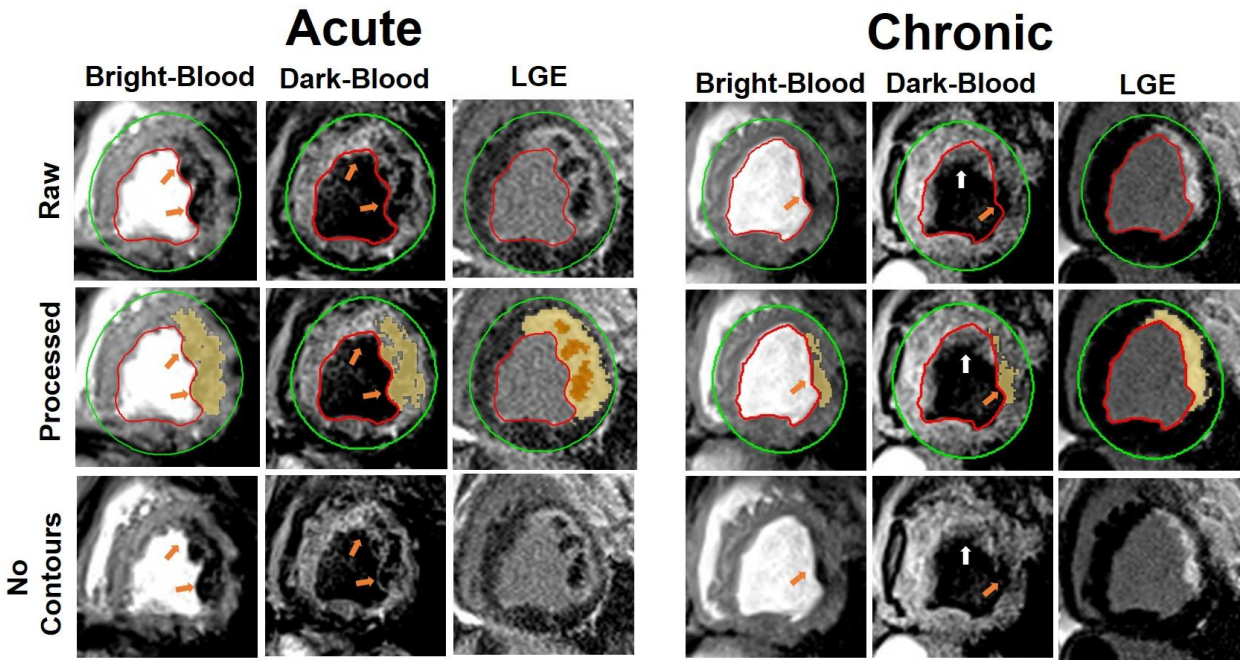

Figure 2.6. Qualitative Differences in Dark-blood vs. Bright-blood T_2*-weighted MRI. A representative case from a canine with acute IMH and chronic ensuing iron deposition demonstrating evidence of stagnant blood in the MI zone and hypointense appearance of IMH, both contributing to the

compromised visual delineation of IMH on dark-blood T_2*-weighted MRI compared to bright-blood T_2*-weighted MRI.

2.3.5 Inter-observer Variability

Inter-observer variability in IMH Extent measured by two expert readers is reported as intraclass correlation coefficients with 95% confidence interval in Table 2.2. In both patients and animals, there was good to excellent agreements in IMH Extent determined by the two expert reviewers when bright-blood T_2*-weighted images were used. However, dark-blood T_2*-weighted images, although lead to modest to good agreement, they performed consistently weaker compared to bright-blood T_2*-weighted images with respect to IMH Extent.

Table 2.2. Inter-observer Variability in Quantifying IMH Extent with Dark-Blood and Bright-Blood T_2*-weighted MRI.

		MI Age	**Dark-blood**	**Bright-blood**
Patients	1.5T	Acute	0.790 (0.345 – 0.932)	0.903 (0.697 – 0.969)
		Chronic	0.756 (-0.544 – 0.965)	0.809 (-0.898 – 0.980)
	3.0T	Acute	0.842 (0.358 – 0.957)	0.922 (0.726 – 0.979)
		Chronic	0.640 (-0.275 – 0.916)	0.801 (-0.230 – 0.968)
Animals	1.5T	Acute	0.813 (-0.180 – 0.956)	0.933 (0.555 – 0.982)
		Chronic	0.688 (0.104 – 0.894)	0.843 (-0.162 – 0.965)
	3.0T	Acute	0.849 (0.026 – 0.969)	0.935 (0.533 – 0.987)
		Chronic	0.607 (-0.233 – 0.895)	0.812 (-0.169 – 0.965)

Numbers reported in parenthesis represent the 95% confidence interval

2.3.6 Validation to ex-vivo T_2*-weighted imaging

Paraffin-fixed sections of the heart stained with Prussian blue from the animals are shown in Figure 2.7(A, B). Hemorrhage was confirmed by the evidence of iron. Representative images of formalin fixed sample of canine heart with chronic MI were show in Figure 2.7(C, D). Good correlation of IMH Extent between in-vivo bright-blood T_2*-weighted images and ex-vivo T_2*-weighted images was shown in Figure 2.7(E). An example of AHA segmentation of IMH in chronic phase of MI from ex-vivo T_2*-weighted, bright-blood T_2*-weighted and dark-blood T_2*-weighted images at 3.0T was shown in Figure 2.7(F).

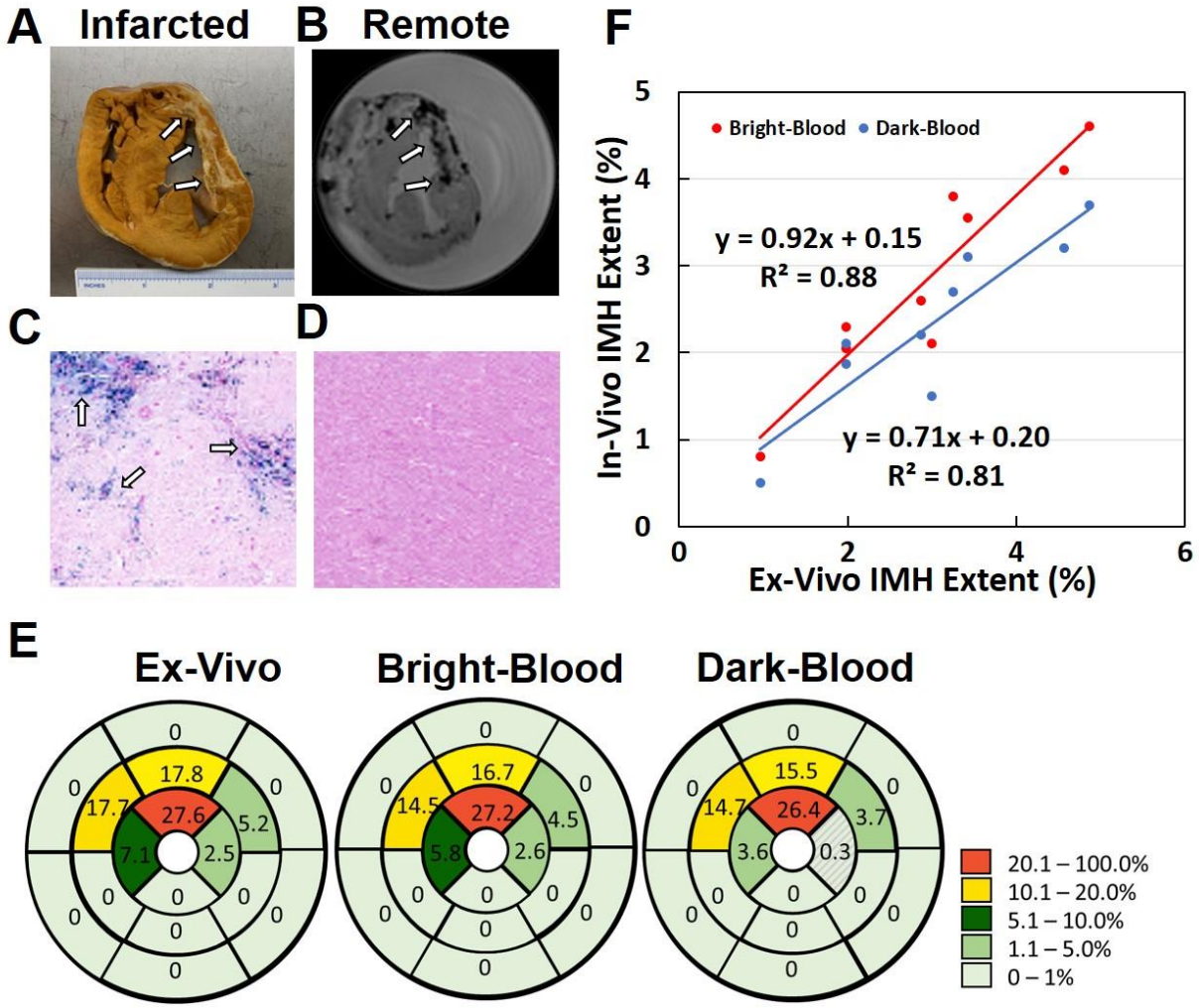

Figure 2.7. Ex-vivo validation of T_2*-weighted MRI for detection of intramyocardial hemorrhage. A short-axis view of a formalin fixed heart from an animal captured with a photograph (Panel A) and 3.0T ex-vivo MRI (Panel B) in the chronic phase MI from one animal are shown. Arrows point to chronic MI territories with history of hemorrhagic MI. Paraffin-fixed myocardial sections (infarcted and remote) stained with Prussian blue from an animal are shown (Panel C and D). Note that the infarcted regions show evidence of iron (blue stains, arrow heads, Panel C) consistent with history of hemorrhagic infarction, which is not evident in the remote territory (Panel D). Panel E shows the AHA segmentation with IMH Extent within each segment. Generally, there was good agreements of segmental IMH Extent between ex-vivo segments and bright- and dark-blood images. However, one of the segments in dark-blood T_2*-weighted images was not identified to be positive for IMH (<1%) relative to the ex-vivo and bright-blood T_2*-weighted images. Panel F shows strong correlation of IMH Extent (as fraction of whole LV volume) between in-vivo bright-blood T_2*-weighted MRI and ex-vivo T_2*-weighted MRI across all animals (y =

0.92x + 0.15, R2= 0.88, $p<0.05$). The same panel also shows very good correlation between in-vivo dark-blood T_2*-weighted MRI and ex-vivo T_2*-weighted MRI across all animals ($y = 0.71x + 0.20$, $R2 = 0.81$, $p<0.05$).

Comparing to ex-vivo validation, sensitivity and specificity for detection of IMH based on bright-blood T_2*-weighted images are both 100%, which verifies the accuracy of IMH Extent measured from bright-blood T_2*-weighted images. Therefore, bright-blood T_2*-weighed images are used as reference for diagnostic performance in patient and animal studies at 1.5T and 3.T in acute and chronic phase of MI.

2.3.7 Diagnostic Performance

Table 2.3 shows sensitivity, specificity, accuracy and AUC for detection of IMH in patients and animals based on dark-blood T_2*-weighted images, with bright-blood T_2*-weighted images serving as the ground truth. In patients, at 1.5T, dark-blood T_2*-weighted images showed moderate sensitivity, good specificity and moderate accuracy for detection of IMH in acute phase of MI; and moderate sensitivity, specificity and accuracy in chronic phase for detection of residual iron in the chronic phase of hemorrhagic MI. At 3.0T, dark-blood T_2*-weighted images showed moderate sensitivity, good specificity and accuracy for detection of hemorrhage in acute phase of MI, and good sensitivity, specificity and accuracy in chronic phase for detection of residual iron in the chronic phase of hemorrhagic MI. In animals, at 1.5T, dark-blood T_2*-weighted images showed excellent sensitivity, moderate specificity and good accuracy for detection of IMH in acute phase of MI; and moderate sensitivity, specificity and accuracy in chronic phase for detection of residual iron in the chronic phase of hemorrhagic MI. At 3.0T, dark-blood T_2*-weighted images showed excellent sensitivity, good specificity and accuracy for detection of hemorrhage in acute phase of

MI, and moderate sensitivity, specificity and accuracy in chronic phase for detection of residual iron in the chronic phase of hemorrhagic MI.

Table 2.3. Diagnostic Performance of Dark-blood T_2*-weighted MRI for Detecting IMH

		Age of MI	Sensitivity (%)	Specificity (%)	Accuracy (%)	AUC
Patients	1.5T	Acute	82.6 ± 15.8*	95.7 ± 8.1	87.5 ± 9.4*	0.892 ± 0.091*
		Chronic	83.7 ± 13.9*	93.4 ± 10.7	83.3 ± 11.3*	0.886 ± 0.098*
	3.0T	Acute	73.5 ± 20.0*	94.7 ± 8.2	88.8 ± 8.0*	0.841 ± 0.138*
		Chronic	87.1 ± 21.6*	92.6 ± 10.1	91.3 ± 10.2*	0.899 ± 0.137*
Animals	1.5T	Acute	88.1 ± 8.0*	94.1 ± 6.8	92.9 ± 5.8*	0.911 ± 0.068*
		Chronic	86.1 ± 10.6*	94.4 ± 11.0	90.4 ± 11.8*	0.903 ± 0.128*
	3.0T	Acute	89.6 ± 9.0*	95.0 ± 8.7	91.6 ± 7.2*	0.923 ± 0.006*
		Chronic	85.7 ± 12.9*	92.9 ± 18.8	89.7 ± 12.9*	0.893 ± 0.142*

***** denotes $p<0.05$

2.4 Discussion

Intramyocardial hemorrhage, which can be noninvasively detected using T_2*-based MRI, has emerged as one of the strongest predictors of adverse outcome in post MI patients [15-18, 117]. However, likely driven by the general consensus [42] in the field that dark-blood T_2* cardiac MRI is preferable over bright-blood T_2* cardiac MRI for imaging cardiac iron overload (such as in thalassemia), a number of recent studies have adopted dark-blood T_2* MRI for imaging IMH [18,

43, 44]. To date however, only bright-blood T_2*-based MRI has been validated for imaging IMH [23, 116] and the relative performance of dark-blood T_2*-based MRI against bright-blood T_2*-based MRI for IMH detection is not known. To address this gap, we investigated the relative performance of dark-blood T_2*-weighted MRI against bright-blood T_2*-weighted MRI for imaging IMH. To this end, we examined the image characteristics and diagnostic performance of dark-blood-prepared T_2*-weighted MRI against bright-blood T_2*-weighted MRI in MI patients and large animal models with IMH in the acute and chronic phases at 1.5T and 3.0T. Independent of subject cohort studied (patients or animals with hemorrhagic MI), field strength (1.5T or 3.0T) and age of MI (acute or chronic MI), we found that SNR and CNR were significantly lower in dark-blood T_2*-weighted MRI compared to the bright-blood counterpart. We also found that the variability of signal in T_2*-weighted images to be greater in dark-blood prepared images compared to the bright-blood images. Notably, we found that IMH Extent, characterized as relative size of IMH to MI, was reduced in dark-blood T_2*-weighted images compared to bright-blood T_2*-weighted images. The observations on the reduced IMH Extent is consistent with the observed loss in SNR and CNR in the dark-blood images. As discussed later, these discrepancies likely also facilitated a compromise in the diagnostic performance of dark-blood T_2*-based MRI for classifying MIs as hemorrhagic versus non-hemorrhagic.

The SNR losses observed in dark-blood T_2*-weighted MRI may be explained on the basis of the double-inversion-recovery (DIR) preparation to attain the appearance of dark blood within the LV chamber. DIR preparation employs two adiabatic inversion pulses, which are applied at the R-wave of a heartbeat. Adiabatic RF pulses are longer than conventional RF pulses to ensure that the adiabatic condition (preservation of the direction of the effective magnetic field during a period of precession around effective field) is met. This can lead to significant loss of magnetization after

inversion [118, 119], which is amplified when two adiabatic inversion pulses are used, as is the case with DIR preparations. This is consistent with our observations of lower SNR we observed with dark-blood T_2*-weighted images compared to a bright-blood T_2*-weighted images, where no DIR preparation is applied. This effect is more pronounced at 3.0T compared to 1.5T as the duration of the adiabatic inversion pulse is typically doubled at 3.0T, which likely explains the greater SNR loss in dark-blood images at 3.0T compared to 1.5T.

Application of dark-blood prepared T_2*-based MRI in the assessment of global iron overload in thalassemia has proven to be beneficial since it provided a means to improve the delineation of the boundary between the blood pool and the myocardium [120]. However, this does not appear to be the case in hemorrhagic MIs, where the iron comprising components of IMH are only found in focal MI regions within the myocardium. Notably, IMH which appears as a hypointense core in the myocardium emanates from the sub-endocardium, which can be incorrectly visualized as part of the blood pool appearing dark in images with the dark-blood preparation. Also, the appearance of dark blood pool within the LV chambers is premised on sufficient cardiac contraction to wash out the blood in the slice of interest, which then is replaced with blood that experienced the first (non-selective) inversion pulse in DIR preparation. In the setting of MI, infarcted walls have compromised contraction. This results in static or slow-moving blood at the infarct border to be only incompletely washed out with each heartbeat, thus giving the impression of a thicker wall. One important consequence of this is that it limits accurate border delineation between the myocardium and blood pool. The appearance of slow-moving blood at the MI zone to mimic tissue has been previously reported in cases where DIR pulses are used for T_2-based acquisition in the heart and large blood vessels [121, 122]. These observations likely explain the weaker inter-

observer reliability in dark-blood prepared T_2*-weighted MRI compared bright-blood T_2*-weighted MRI.

One of the key findings from this study is that the size of IMH is significantly reduced in the dark-blood T_2*-weighted images compared to bright-blood T_2*-weighted images. The reduction in IMH size likely stems from reduced SNR and CNR due to DIR preparation. The loss of contrast between IMH and remote myocardium results in the underestimation of IMH Extent when quantification of hemorrhage is performed using the validated mean-2SD approach, since by definition this approach is sensitive to increased SD. Our observation here highlights an important limitation of dark-blood T_2*-weighted MRI; that is, the reduction in IMH size implies that dark-blood T_2*-weighted MRI can increase the false negatives of IMH, which is consistent with the observed significant reduction in sensitivity, accuracy and AUC compared to bright-blood T_2*-weighted images. Another practical consequence of using dark-blood T_2*-weighted approach is that the associated increase in false negatives with the approach would necessitate larger sample size for investigations aiming to modulate iron within MI in the pre-clinical and clinical settings.

Even though, the disparity between the findings in dark-blood versus bright-blood T_2*-based MRI are smaller at 1.5T, the negative impact of dark-blood technique on IMH detection is not negligible. Our findings support the notion that dark-blood and bright-blood images do not provide equivalent information with respect to IMH with the dark-blood T_2*-based MRI carrying the risk of under diagnosing IMH. Hence, we recommend that among the T_2* variants currently available, bright-blood T_2*-based MRI should be the method of choice for identifying hemorrhagic MIs.

2.5 Study Limitations

Our study was limited to a small number of patients and animals as it was designed to evaluate the merits of dark-blood T_2*-based approach against the conventional bright-blood T_2*-based imaging

in both clinical and preclinical settings [123]. Next, the findings from this study are only limited to the differences between bright- and dark-blood prepared T_2*-based MRI. As such, our findings here do not reflect the existing limitations, particularly off-resonance issues compromising image quality in cardiac T_2* imaging, that are also common to both bright- and dark-blood T_2*-based imaging. Although the off-resonance issue may be mitigated by further innovations in shimming or imaging processing, such approaches are not yet available. Thus, we acquired both dark- and bright-blood T_2* images with the state-of-the art shimming approaches currently available. To minimize the influence of these artifacts in this study, we (a) used only moderate TEs (~14 ms at 1.5T and ~12 ms at 3.0T) to balance image contrast against large signal voids; (b) studied both patients (24 of the 29) and animals (all) primarily with LAD infarctions to mitigate against prominent off-resonances artifacts at inferior and inferolateral walls [104]; and (c) excluded the inferior and inferolateral segments in image analysis when off-resonance artifacts were present. These efforts allowed us to selectively study the effects of dark-blood preparation while minimizing any confounding effects from off-resonance artifacts.

2.6 Conclusions

While IMH can be visible on dark-blood T_2*-weighted MRI, the overall conspicuity of IMH is significantly reduced compared to that observed in bright-blood T_2*-weighted images, across infarct age in clinical and preclinical settings at 1.5T and 3.0T. Hence, dark-blood T_2*-weighted MRI should be used with the understanding that it carries the potential to misclassify hemorrhagic MIs as non-hemorrhagic MIs.

Chapter 3: Mechanism of Signal Loss in Dark-Blood T_2* Cardiac MRI of Intramyocardial Hemorrhage

3.1 Introduction

In Chapter 2, we showed that compared to bright-blood T_2*, double-inversion-recovery (DIR) prepared dark-blood cardiac T_2*-weighted images reduces image contrast of hemorrhagic lesions resulting in compromised diagnostic capability for detection of IMH [46]. In this chapter, we explore the mechanisms of signal loss in double-inversion-recovery prepared dark-blood T_2* images.

The dark-blood preparation with DIR pulses [40] consists of one non-selective 180° inversion adiabatic pulse, which is immediately followed by a selective 180° inversion adiabatic pulse. Adiabatic pulses are utilized to take advantage of their relative insensitivity to B_1 inhomogeneity. However, to ensure the adiabatic condition, the RF pulses are much longer (10 – 20 ms) than conventional RF pulses. Given that two consecutive adiabatic inversion pulses are required, during the inversion periods T_1 and T_2 relaxations will be inevitable, especially in the myocardium where T_2 is typically around short (50 ms) [118]. This can compromise both the SNR and CNR.

Here we hypothesize that the image contrast loss on dark-blood cardiac T_2*-weighted images of intramyocardial hemorrhage originates from spin relaxation during double-inversion-recovery preparation, and it can be recovered by increasing the delay time between DIR preparation and acquisition. We will test the hypothesis using phantoms and validate our findings in an animal model. We will also evaluate the influence of DIR preparation on T_2*-weighted images and T_2* maps.

3.2 Methods

3.2.1 Phantom Study

Phantoms were constructed using agar (Figure 3.1) to verify the magnetization loss due to DIR preparation and the recovery periods by varying delay times between DIR and image acquisition. Iron-oxide (Feromoxytol) was used to reduce relaxation times of Tube 1 which was made of 2% agar gel and 0.5 mmol/L Ferumoxytol resulting in T_1 of 840.3 ± 26.8 ms and T_2 of 32.0 ± 1.8 ms. Tube 2 was made of pure 2% agar gel (with no Ferumoxytol), which resulted in T_1 of 1834.2 ± 34.9 ms and T_2 of 39.4 ± 1.8 ms.

Phantoms were immersed in water and imaged at 3.0T MR system (Verio, Siemens Healthcare, Erlangen, Germany) with simulated ECG signals at a heart rate of 67 beats per minute. Multi-echo T_2*-weighted images with and without DIR preparation were acquired (TE = 1.58, 2.91, 4.24, 5.57, 6.90, 8.23, 9.58, and 10.89 ms; TR = 12.97 ms, segments = 7, flip angle = 18°, bandwidth = 925 Hz/pixel, spatial resolution = 1.1x1.1x6.0 mm^3, GRAPPA accelerate factor=2, 200% of dark-blood slice thickness were used for the second inversion pulse in DIR preparation). To evaluate the effect of delay times, images were acquired with various delay times (TD = 0, 100, 200, 300, 400, 500, 600, 700, 860, 1060, 1260, 1460, 1660 ms) between DIR preparation and readout (Figure 3.1). DIR prepared images with TD < 700 ms were acquired with readout at every heartbeat. DIR prepared images with TD > 700 ms were acquired with readout at every other heartbeat. For reference, T_2*-weighted images without DIR preparation were acquired with readout at every heartbeat. T_2* maps were generated by pixel wised fitting in CVI[42] (Circle Cardiovascular Imaging, Calgary, Alberta, Canada).

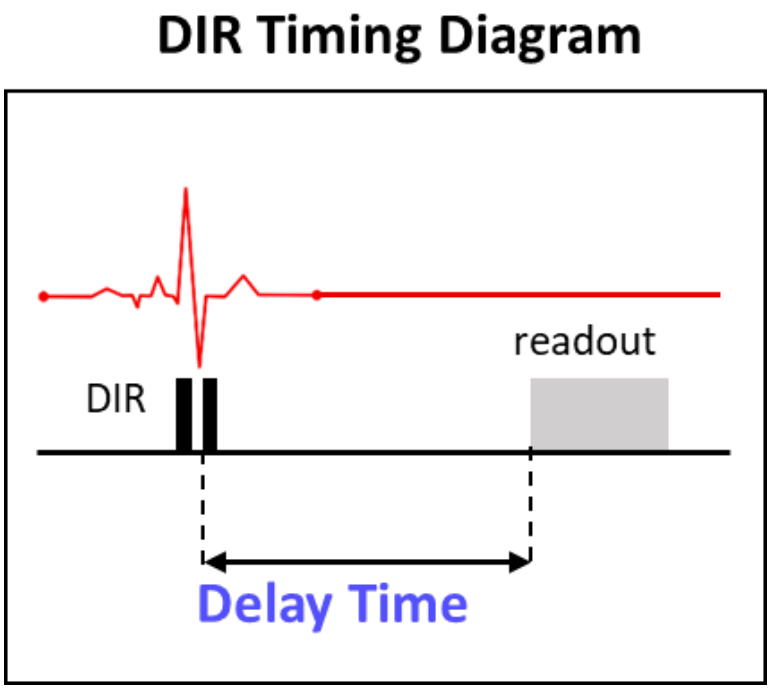

Figure 3.1. Illustration of timing of DIR and delay time (TD) between DIR pulses and readout.

3.2.2 Animal Study

Consistent with the protocol approved by the Institutional Animal Care and Use Committee (IACUC), hemorrhagic MIs were created in canines (n = 6) by occluding the left-anterior descending coronary artery (LAD) for 3 hours, followed by reperfusion. Animals were allowed to recover for 2 months. All animals were intubated and anesthetized with isoflurane (1-1.5 %/volume) and slice-matched, breath-held, ECG triggered, multi-echo bright-blood T_2*-weighted and DIR-prepared T_2*-weighted images were acquired. Animals were studied in the chronic phase at 2 months post MI. As per findings in Chapter 2, bright-blood T_2* images were used for validation.

All T_2*-weighted images were acquired at diastole with in-phase echo times (TE = 2.32, 4.64, 6.96, 9.28, 11.60, 13.92 ms and TR = 15.83 ms) and slice thickness of 200% of dark-blood preparation. DIR prepared dark-blood T_2*-weighted images were acquired with short (TD = 280 ms), medium (TD = 500 - 700 ms) and long (TD = 1200 ms) delay times between DIR and readout. Timing of DIR preparation was adjusted to match the delay time required for short and long TD groups. Images with short and medium TD were acquired with readout performed at every heartbeat. Due to variation of heart rate in animals, TD was adjusted between 500 to 700 ms for medium TD group. Images with long TD were acquired by performing readout every other heartbeat at diastole and DIR preparation during the previous heartbeat. T_2* maps were generated by pixel-wise fitting in CVI[42] (Circle Cardiovascular Imaging, Calgary, Alberta, Canada). LGE images were acquired as reference of MI at 3T with TR/TE = 1 R-R interval/2.1 ms, flip angle = 20°, bandwidth = 287 Hz/pixel, spatial resolution = 1.1x1.1x6.0 mm^3.

3.2.3 Image Analysis

All image analyses were performed with CVI[42] (Circle Cardiovascular Imaging, Calgary, Alberta, Canada). Remote myocardium was identified as the region absent of hyperintensity on LGE images. MI zone was defined as the region with mean signal intensity (SI) of at least 5 standard deviations (SD) greater than that of a reference region of interest (ROI) drawn in remote myocardium.

IMH was identified by two different methods (Mean – 2SD and T_2* < 20 ms). For the Mean – 2SD approach, MI zones were identified to be hemorrhagic if there were hypointense cores within MI on T_2*-weighted images (TE = 13.92 ms) with a mean signal intensity 2 SD lower than that of the reference region in the remote myocardium. Subsequently, territories positive for IMH were copied onto T_2* maps for determination of T_2*. For T_2* < 20 ms, IMH was identified as the region

on T_2* maps with T_2* values less than 20 ms within MI zones. All following analysis were performed based on the two different methods.

Area of IMH on each slice measured from T_2*-weighted images and T_2* maps were normalized by the area of MI measured from the corresponding slice-matched LGE images and reported as IMH Extent. SNR and CNR values were computed from T_2*-weighted images. All SNR and CNR were normalized by SNR and CNR measured from bright-blood T_2*-weighted images respectively and reported as relative SNR and relative CNR.

3.2.4 Statistical Analysis

Statistical analysis was performed using IBM SPSS Statistics 23 (IBM Corp., Armonk, New York). Normality of continuous data was determined by using the Shapiro-Wilk test and quantile-quantile plots. Normally distributed variables were compared using repeated measures ANOVA. Repeated measures from each heart were nested for analysis. Pairwise comparisons for non-normal data were performed using the Mann-Whitney U test.

3.3 Results

3.3.1 Phantom Study

Figure 3.2A shows first echo of T_2*-weighted images (TE = 1.58 ms) of agar phantoms with various TD (windowed to the same level) along with corresponding T_2* maps. Visible signal loss was observed on DIR prepared images in both tubes. Relative SNR of each tube is shown in Figure 3.2B. There was nearly a 40% SNR loss on images acquired immediately following DIR preparation. Figure 3.2B shows that SNR is recovered with increased TD between DIR and readout. For both tubes, recovering SNR with increasing TDs showed similar trend with T_1 relaxation curve.

T_2* values of the two tubes with different imaging protocols are shown in Figure 3.2C. No significant differences were found between groups with resepect to T_2* values.

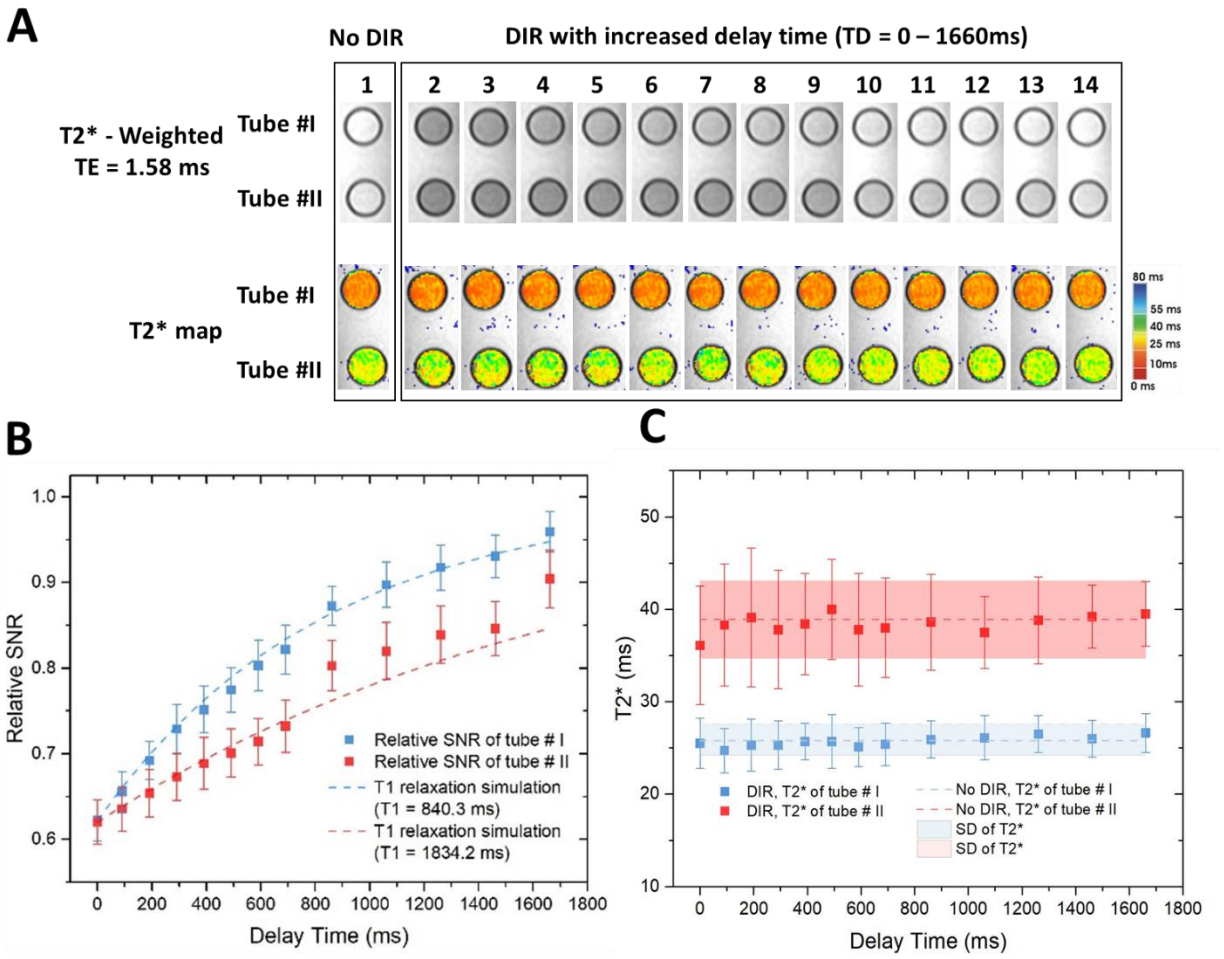

Figure 3.2. A. T_2*-weighted images and T_2* maps of phantom study with DIR preparation following by readout in different delay time. Delay time = 0 (3), 100 (4), 200 (5), 300 (6), 400 (7), 500 (8), 600 (9), 700 (10), 860 (11), 1060 (12), 1260 (13), 1460 (14), 1660 (15) ms. **B.** Relative SNR of DIR prepared images. Dotted lines are theoretical T_1 relaxation curves. **C.** T_2* from DIR prepared and non-DIR-prepared scans.

3.3.2 Influence of Delay Time - Representative T_2*-weighted and T_2* maps

Representative T_2*-weighted (TE = 13.92 ms) and LGE images from a canine acquired with different TDs are shown in Figure 3.3. IMH determined using T_2*-weighted images using Mean-

2SD method is highlighted in yellow in the processed images of Fig. 3.3. Corresponding T_2* maps with varying delay times are shown at the bottom row in Figure 3.3.

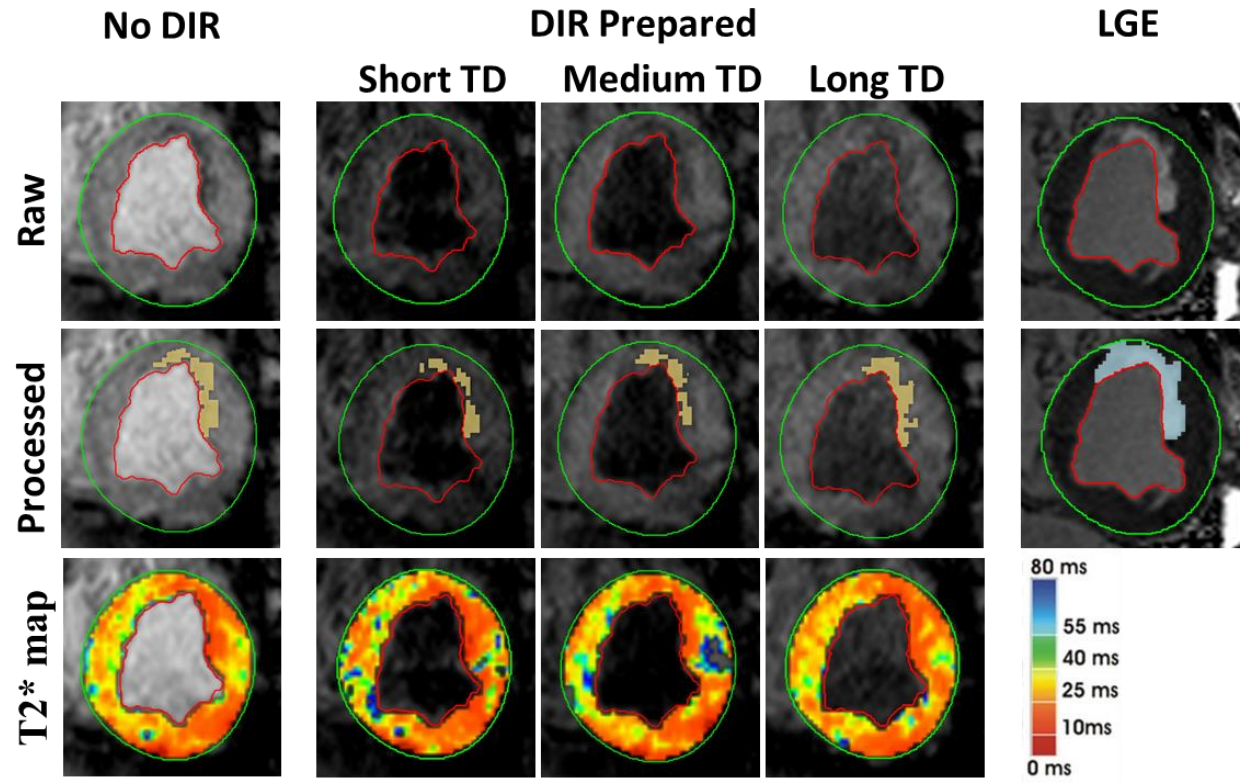

Figure 3.3. Representative T_2*-weighted images and corresponding T_2* maps in a canine with hemorrhagic MI acquired with no DIR, with DIR at different TD and LGE images. IMH identified using Mean-2SD criteria is highlighted in yellow (Processed, middle row).

3.3.3 Relative SNR and CNR

Figure 3.4 shows relative SNR (Figure 3.4A) and relative CNR (Figure 3.4B) measured from DIR-prepared T_2*-weighted images normalized to bright-blood T_2*-weighted images. Compared to bright-blood T_2*-weighted images, significant reduction of SNR was found on DIR-prepared T_2*-weighted images with short and medium TDs. On average, SNR was reduced on DIR prepared T_2*-weighted images by 41.0% (short TD) and 28.4% (medium TD) compared to bright-blood T_2*

images. No significant difference in SNR was found between bright-blood group and DIR-prepared long TD group. Similar results were found on CNR analysis. Compared to that bright-blood images, CNR was significantly reduced by 22.1% (short TD) and 17.8% (medium TD). CNR of DIR-prepared T_2*-weighted images recovered to the same level of that on non-DIR-prepared T_2*-weighted images with long TD.

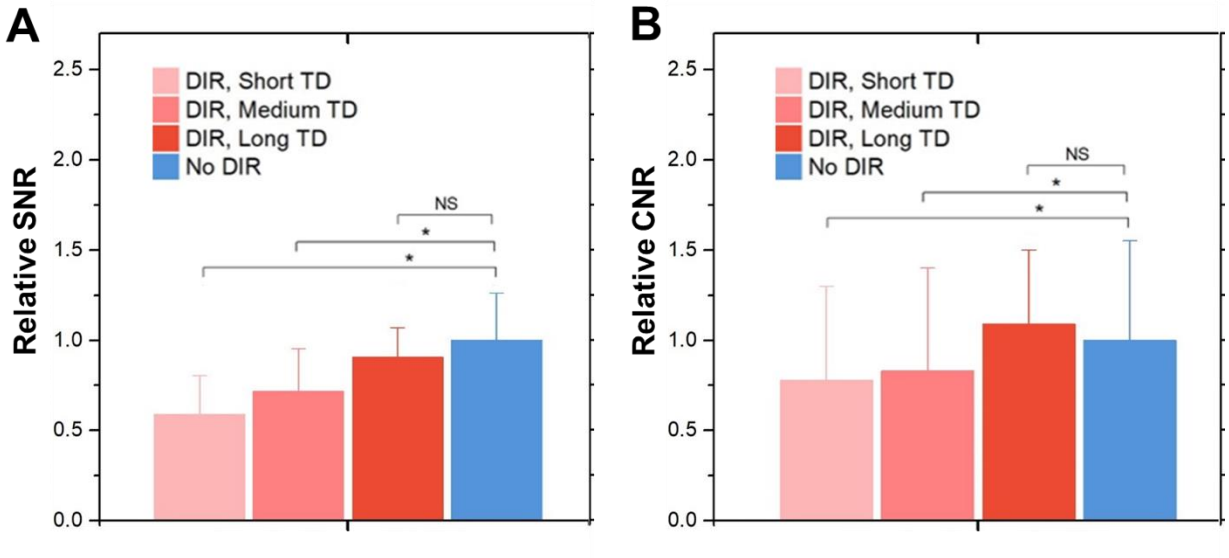

Figure 3.4. A. Relative SNR of DIR-prepared T_2*-weighted images (TE = 13.92 ms) with short, medium, and long delay times (TD) normalized by SNR from non-DIR prepared T_2* images. **B.** Relative CNR of DIR-prepared T_2*-weighted images (TE = 13.92 ms) with short, medium, and long delay times (TD) normalized by CNR from non-DIR prepared T_2* images. Significant differences of relative SNR and CNR were found between non-DIR prepared group and DIR prepared group with short and medium TD (* $p<0.05$).

3.3.4 IMH Extent

IMH extent was evaluated using Mean-2SD criterion on T_2*-weighted images and T_2*<20 ms threshold on T_2* maps. Results are shown in Figure 3.5. Figure 3.5A shows IMH extent measured using Mean-2SD criterion on T_2*-weighted images acquired with various delay times. On average, IMH extent was significantly underestimated on DIR-prepared T_2*-weighted images with short (38%) and medium (33%) TD, respectively. No significant difference was found between group of DIR-prepared images with long TD and without DIR preparation. Figure 3.5B shows IMH extent measured using T_2*<20 ms approach on T_2* maps generated from T_2*-weighted images without DIR preparation, and DIR-prepared groups with short, medium, and long TD. No difference in IMH Extent was found between the groups.

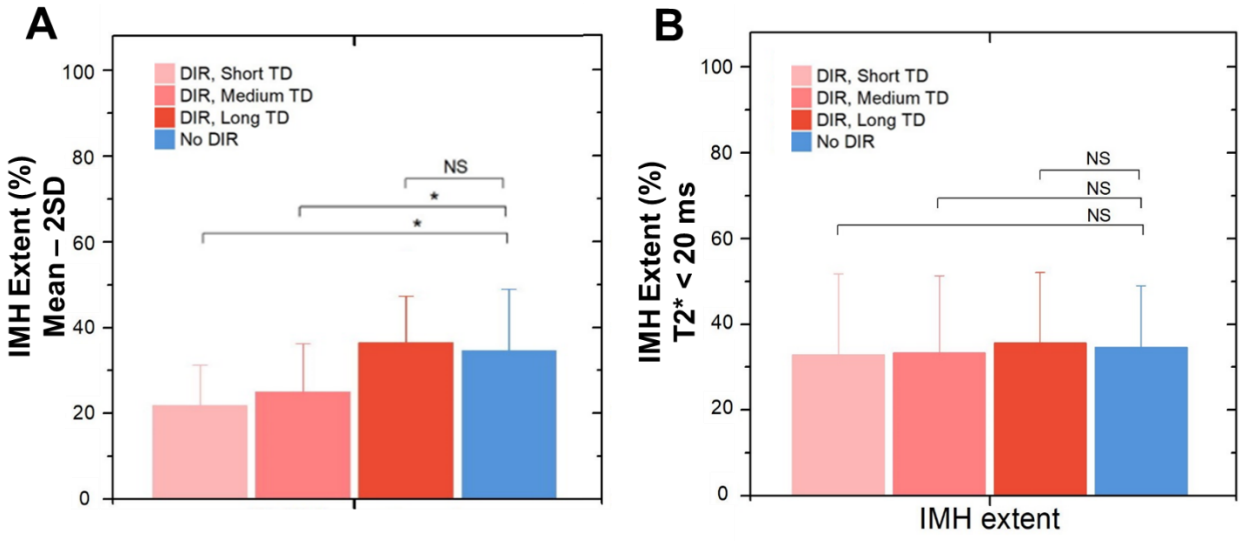

Figure 3.5. IMH Extent based on Mean-2SD criterion on T_2*-weighted images (A) and by T_2*<20 ms approach (B). IMH was significantly underestimated when Mean-2SD criterion was applied to T_2*-weighted images with short or medium delay TD relative to no DIR preparation (* $p<0.05$). No difference in IMH Extent was found between groups when T_2*<20 ms was used on T_2* maps.

3.3.5 T_2* Measurement

T_2* of IMH and remote myocardium is listed in Table 3.1. No difference was found between T_2* values of remote myocardium measured from DIR-prepared T_2* maps and non-DIR-prepared T_2* maps. T_2* values of IMH regions determined using Mean-2SD criteria on DIR-prepared images with short TD was 16.2 ± 1.9 ms, which was significantly lower than that measured from images acquired without DIR preparation (T_2* = 18.7 ± 2.4 ms, $p<0.05$). Similar observation was made of T_2* values of IMH determined from DIR-prepared images with medium TD, which was 17.2 ± 2.9 ms and significantly lower ($p<0.05$) than that from bright-blood T_2*. T_2* of IMH determined using Mean-2SD criteria on long TD DIR-prepared T_2* maps were not different from T_2* maps acquired without DIR preparation. T_2* values of IMH determined using T_2*<20 ms criterion from all four groups showed no significant difference between each other.

Table 3.1. T_2* of remote myocardium and IMH identified using Mean-2SD and T_2*<20 ms criteria.

T_2* (ms)	DIR-prepared			No DIR Preparation
	Short TD	Medium TD	Long TD	
Remote Myocardium	28.7 ± 2.6	28.1 ± 1.7	27.8 ± 2.4	27.7 ± 2.1
IMH (Mean-2SD)	16.2 ± 1.9 *	17.2 ± 2.9 *	18.7 ± 3.0	18.7 ± 2.4
IMH (T_2*<20m)	18.7 ± 2.0	18.3 ± 2.1	18.4 ± 3.0	18.3 ± 2.4

3.4 Discussion

Phantom studies confirmed signal losses from the double-inversion-recovery preparation and the hypothesis that if delay time between DIR preparation and readout is increased, signal loss can be mitigated. T_2* measured from the phantoms showed no significant difference in T_2* values supporting the notion that the signal losses induced by DIR did not affect T_2* decay. In-vivo findings were consistent with phantom studies. SNR was measured in remote myocardium on DIR prepared T_2*-weighted images and normalized by SNR from bright-blood T_2*-weighted images. With short and medium TD, when signal loss from DIR has not fully recovered, significant reduction in SNR was found on DIR-prepared T_2*-weighted images (Figure 3.2B). With long TD of 1200 ms, SNR recovered to the near equivalent level as T_2*-weighted images without DIR preparation.

To evaluate the effect of signal loss from DIR preparation on both T_2*-weighted images and T_2* maps in the assessment of IMH, two different methods commonly employed in the field were used. Our finding of reduced SNR and CNR on T_2*-weighted images, which lead to reduction in IMH Extent measured using Mean-2SD method was in line with results from Chapter 2. When SNR and CNR recovered to the same level as T_2*-weighted images acquired without DIR preparation, the underestimation of IMH Extent was marginalized, further supporting our hypothesis.

Comparing to T_2* values within IMH territories measured from non-DIR prepared T_2* maps, T_2* values of IMH measured from DIR-prepared T_2* maps with short and medium TDs by mean-2SD are significantly lower. It is because iron depositions in intramyocardial hemorrhage are distributed heterogeneously. Significant SNR loss on DIR-prepared T_2* images impaired sensitivity for IMH detection so that only more severe iron deposition can be identified on DIR-prepared T_2* images with insufficient delay time.

Both phantom and animal studies showed that DIR preparation did not affect T_2* values on T_2* maps. Since DIR preparation did not affect the measurement of IMH Extent or T_2* evaluation based on T_2*<20 ms method, T_2* maps based on DIR preparation may be an alternative, however this approach should still be carried out with caution. First, DIR induced signal loss on T_2*-weighted images can impair the goodness of T_2* fitting. This is evidence by the blue and black areas on T_2* maps (see Figure 3.3) with DIR-preparation at short and medium TDs indicating the failure of T_2* fitting with $r < 0.5$ threshold. In some cases, when SNR is reduced below critical thresholds at long echo times, it can introduce unexpected bias in T_2* analysis. Second, T_2* maps are significantly affected by the off-resonance artifacts from the heart-lung interface compared to T_2*-weighted images (See Figure 3.3), which makes it nearly impossible to discriminate between regions affected by off-resonance and non-hemorrhagic MI territories when using the T_2*<20 ms approach for T_2* analysis.

3.5 Conclusion

In this Chapter, mechanism contributing to signal loss on dark-blood T_2* images were shown to result from signal loss during double-inversion-recovery preparation and that it can be mitigated by imposing a significantly longer recovery time between DIR and readout. However, this has the added disadvantage of missing the blood-nulling point, ultimately compromising the value of dark-blood T_2*-based approach. It can also increase scan time which is not desirable in clinical settings for imaging of patients with intramyocardial hemorrhage. IMH assessment on T_2* maps can be used as an alternative to T_2*-weighted images when DIR-prepared dark-blood T_2* imaging technique is used; however, SNR levels, goodness of T_2* fitting and off-resonance artifacts should be carefully considered.

Chapter 4: Fat Corrected Myocardial T_2* Mapping for Chronic Hemorrhagic Myocardial Infarction

4.1 Introduction

Myocardial infarction leads to scarring of myocardial tissue, which at times can be infiltrated by fat [52-54], which is known to significantly impair cardiac function and is a strong predictor of chronic heart failure [124]. Both computed tomography (CT) [125, 126] and magnetic resonance imaging [127] can be used for detection of myocardial fat but the use of non-invasive imaging for characterizing myocardial fat is relatively new and remains to be developed [128]. For MR-based characterization of fatty infiltration within the scar, particularly in the setting of hemorrhagic infarction, remains unexplored despite the understanding that the presence of fat may confound the quantification of iron due to chemical shifts.

In this Chapter, we investigated the separability of hemorrhagic remnants and potential fatty infiltration in the chronic phase of infarction using a multi-echo chemical-shift-based water-fat separation algorithm [82] as described in Chapter 1. Specifically, we assessed the relationship between iron deposition and fat infiltration in MIs for a better understanding of the progressive development of lipomatous metaplasia within the infarct-related scar.

4.2 Method

4.2.1 Animal Model

According to the protocol approved by the Institutional Animal Care and Use Committee, MIs were created in 11 dogs (20 - 25 kg, all female) by 3 hours of LAD occlusion, followed by reperfusion. Prior to MRI scans, all animals were intubated and anesthetized with isoflurane (1-

1.5 %/volume). Cardiac MRI was performed at 3 days post reperfusion (acute phase) and at early (8 weeks) and late (6 months) chronic phases of MI.

4.2.2 Image Acquisition

Breath-held, ECG-gated, contiguous, 2D slice-and-resolution matched, short-axis multi-gradient-echo T_2* and LGE images covering whole LV were acquired at 3.0T MR system (Biograph mMR, Siemens, Erlangen, Germany). Multi-gradient-echo T_2* images were acquired with 6 echoes, TE = 3.3 – 13.3 ms, ΔTE = 2.2, TR = 20 ms, flip angle = 12º, image resolution 1.5 × 1.5 × 6.0 mm^3. LGE images were acquired with inversion-recovery preparation and balanced steady-state free precession readout, TR = 3.42 ms, TE = 1.47 ms, flip angle = 20º, image resolution 0.7 × 0.7 × 6.0 mm^3.

4.2.3 Image Analysis

LGE images were used as reference for identification of MI. Regions with signal intensity 5 standard deviation higher than remote myocardium on LGE images were considered as infarcted areas. Direct fitting R2* ($1/T_2$*) maps (referred as DF-R2*) were generated from multi-gradient echo (mGRE) images by directly fitting to a mono-exponential model using MATLAB. Using a chemical-shift-based water-fat separation algorithm (as outlined in Chapter 1), confounder-corrected R2* (CC-R2*) and proton density fat-fraction (PDFF) maps were reconstructed with mGRE images.

Mean R2* values of MI regions determined using DF-R2* maps were compared with R2* values from CC-R2* maps at acute, early and late chronic phases of MI. The time dependent relationship between iron deposition and fat infiltration were evaluated by linear regression using CC-R2* and PDFF at different time points.

4.2.4 Statistical Analysis

Statistical analysis was performed using IBM SPSS Statistics 23 (IBM Corp., Armonk, New York). Normality of continuous data was determined by using the Shapiro-Wilk test and quantile-quantile plots. Normally distributed variables were compared using repeated measures ANOVA. Repeated measures from each heart were nested for analysis. Pairwise comparisons for non-normal data were performed using the Mann-Whitney U test. DF-R2*, CC-R2* and PDFF measurements were reported as mean ± SEM unless stated otherwise. Linear regression analyses were performed to evaluate the relation between CC-R2* and PDFF at day 3, week 8 and month 6. Statistical significance was set at $p<0.05$.

4.3 Results

4.3.1 Simulations

Simulations were performed in MATLAB to assess the effect of chemical shift on pixel-wise mono-exponential T_2* fitting. Assumptions made were as follow: main magnetic field is 2.89T, initial magnetization (M0) contributed from overall water and fat is 1, proton density fat fraction (PDFF) is 0.3, T_2* relaxation time is dominated by iron within the voxel and used as 20 ms for both water and fat magnetizations, chemical shift between water and fat was set as 420 Hz, and inter-voxel magnetic field inhomogeneity and noise were assumed to be insignificant.

Figure 4.1 shows the influence of chemical shift on MR signals within a voxel containing 30% of fat. A fluctuation of magnetization (magnitude, grey line) was observed with increasing echo times. Simulations also showed that in-phase and out -of-phase echoes occurred every 2.38 ms. Mono-exponential fitting of the in-phase echoes (blue line, Fig. 4.1) and out-of-phase echoes (yellow line, Fig. 4.1) resulted in T_2* of 20.00 ms and 20.02 ms, respectively, with both fits of r^2

of 1.00. Red circles (Fig. 4.1) represent simulated magnetization magnitude at practical TEs (3.3 to 13.3 ms evenly distributed with 2.0 ms interval). T_2* fitting using these echoes (red line in Fig. 4.1) resulted in T_2* of 25.42 ms but with r^2 of 0.05.

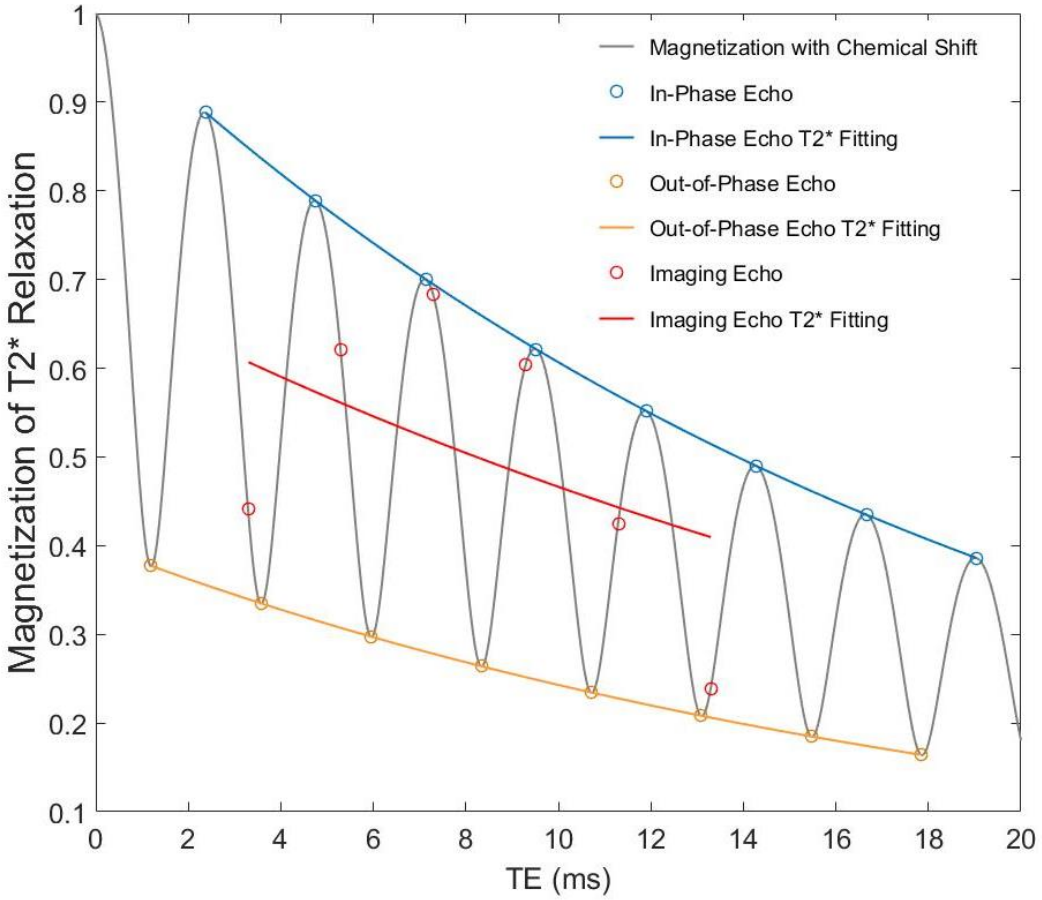

Figure 4.1. Simulation of free-induction decay in the presence of chemical shift with 30% of proton density from fat. Chemical shift = 420 Hz. T_2* relaxation started at 0 ms and lasts for 20 ms. No noise or inter-voxel magnetic field inhomogeneity was considered. Out-of-phase echo first appeared at TE = 1.19 ms and in-phase echo first appeared at TE = 2.48 ms. They both recurred every 2.48 ms. T_2* fitting by all in-phase echoes perfectly aligned with theoretical exponential decay with T_2* relaxation time of 20 ms starting at M0 = 1 (blue line, y = exp(-x/20.00), r^2 = 1.00). T_2* fitting by all out-of-phase echoes also followed an exponential decay with T_2* relaxation time of 20 ms (yellow line, y = 0.40*exp(-x/20.02), r^2

= 1.00). At echo times in practice used for this study, best T_2* fitting was y = 0.69*exp(-x/25.42), r^2 = 0.05 (red line).

4.3.2 Iron and fat quantification

Figure 4.2 showed an example of hemorrhagic MI imaged at 3 days, 8 weeks and 6 months post reperfusion. MI were identified on LGE images. Confounder- corrected R2* and proton density fat fraction maps are generated by chemical-shift-based water-fat separation algorithm. Average DF- R2*, CC-R2* and PDFF within MI zone and remote myocardium were measured and reported in Table 4.1.

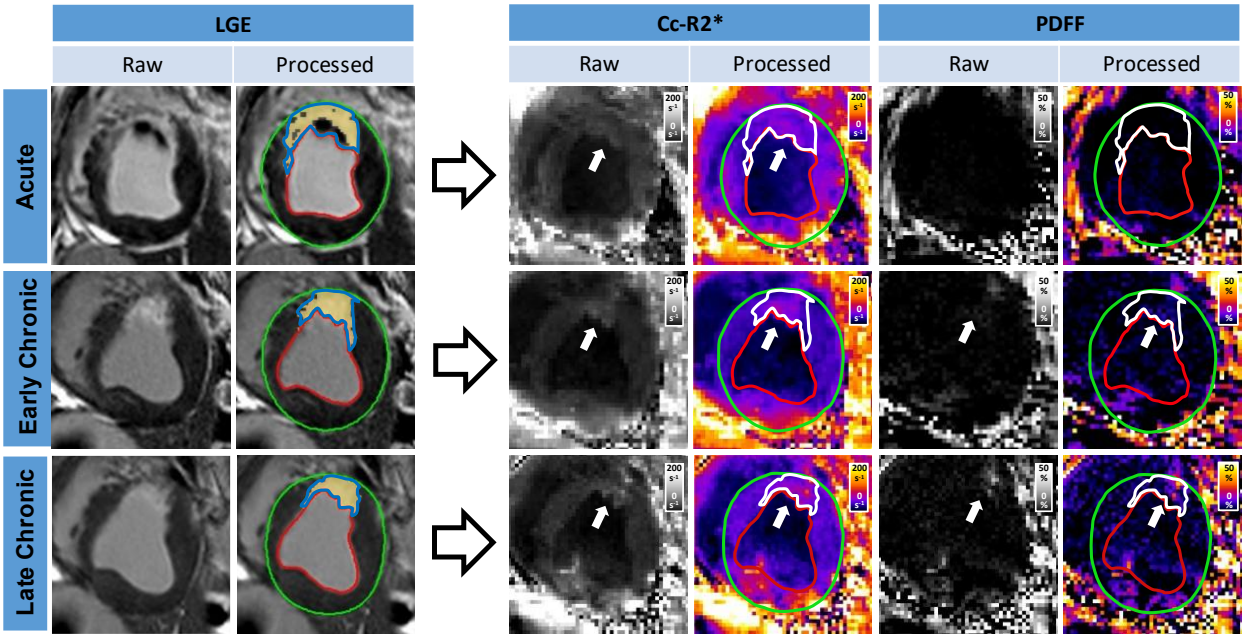

Figure 4.2. An example of hemorrhagic MI from acute to late chronic phases with iron and fat quantification by water-fat separation algorithm. LGE images of MI were used to identify MI zones (blue contours). ROI were drawn on LGE images and forwarded to confounder-corrected R2* and PDFF maps which were generated by chemical-shift-based water-fat separation algorithm using mGRE T_2* images. Arrows point to iron deposits on CC-R2* maps and fat infiltration on PDFF maps.

Table 4.1.DF-R2*, CC-R2* and PDFF measured from T_2* images acquired at acute, early chronic, and late chronic phases of MI. * denotes significate differences of DF-R2*, CC-R2* and PDFF measured in hemorrhagic MI zones and from remote myocardium. # denotes differences between DF-R2* and CC-R2* using the same set of T_2* images.

	DF-R2* (s^{-1})		CC-R2* (s^{-1})		PDFF (%)	
	Mean	SEM	Mean	SEM	Mean	SEM
Acute MI – hMI	43.6*	2.9	43.9*	3.0	1.88	0.11
Acute MI – Remote Myocardium	33.8	0.7	33.8	0.7	1.78	0.13
Early Chronic MI – hMI	44.2*#	2.7	45.5*	2.6	2.52*	0.19
Early Chronic MI – Remote Myocardium	33.6	0.8	33.7	0.9	1.85	0.12
Late Chronic MI – hMI	45.6*#	2.8	47.1*	3.1	4.62*	0.40
Late Chronic MI – Remote Myocardium	33.3	0.9	33.5	1.0	1.95	0.16

Plots of PDFF in acute, early chronic, and late chronic phases of MI were shown in Figure 4.3. Baseline of fat content in remote myocardium was constant across time: 1.78 ± 0.13 % in acute phase, 1.85 ± 0.12 % in early chronic phase, 1.95 ± 0.16 % in late chronic phase of MI. No significant difference was found between groups with respect to PDFF measured from remote myocardium over time. On the contrary, PDFF measured from hemorrhagic MI zones increased from 1.88 ± .011 % in acute phase of MI to 2.52 ± 0.19 % and 4.62 ± 1.95 % in early chronic and late chronic phases of MI respectively. Significant differences ($p<0.05$) were found between PDFF in MI zone and in remote myocardium in early and late chronic phases of MI.

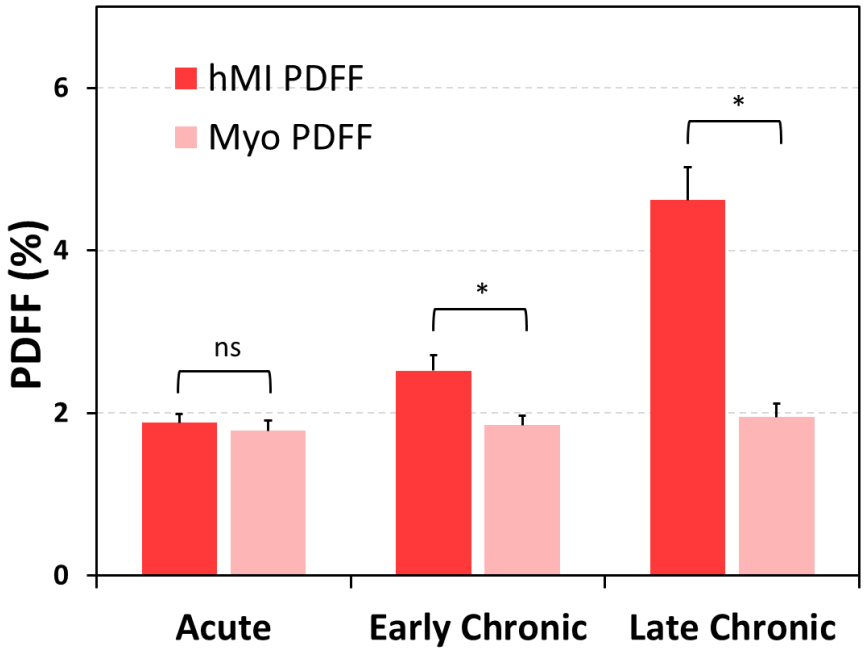

Figure 4.3. Proton density fat fraction (PDFF) measured within MI and remote myocardium territories in acute, early chronic, and late chronic phases of MIs. Significant increase of PDFF were found in MI zones in early and late chronic phases of MI comparing to remote myocardium indicating fat infiltration (* $p<0.05$).

Bar-plots of R2* from direct fitting method and water-fat separation algorithm are shown in Figure 4.4. Baseline of myocardium R2* kept steady in a range of 30 to 35 s^{-1} in all scenarios. No difference was found in remote myocardium R2* measured by different methods or in different MI phases. Expected higher R2* (comparing to R2* in remote myocardium) increased by iron deposition were found in hemorrhagic MI zones by both R2* mapping methods ($p<0.05$, * in Table 4.1). In acute phase of MI at 3 days post reperfusion, average R2* of hemorrhagic MI (hMI) territories in DF-R2* maps and CC-R2* maps remained the same. In DF-R2* map, average R2* was 43.6 ± 2.9 s^{-1} and 43.9 ± 3.0 s^{-1} in cc-R2* map. However, R2* values were underestimated (overestimation for T_2*) on DF-R2* maps comparing to that from CC-R2* maps at 8-week and 6-

month time points ($p<0.05$, # in Table 4.1). At week 8, average R2* in DF-R2* map was 44.2 ± 2.7 s^{-1}, which was found significantly lower than that of 45.5 ± 2.6 s^{-1} in CC-R2* maps with average bias of 1.2 ± 0.36 s^{-1}. At month 6 in late chronic phase of MI, bias between R2* measurement increased to 1.6 ± 0.48 s^{-1} between groups. In DF-R2* map, average R2* of MI zones was 45.6 ± 2.8 s^{-1} and 47.1 ± 3.1 s^{-1} in cc-R2* maps.

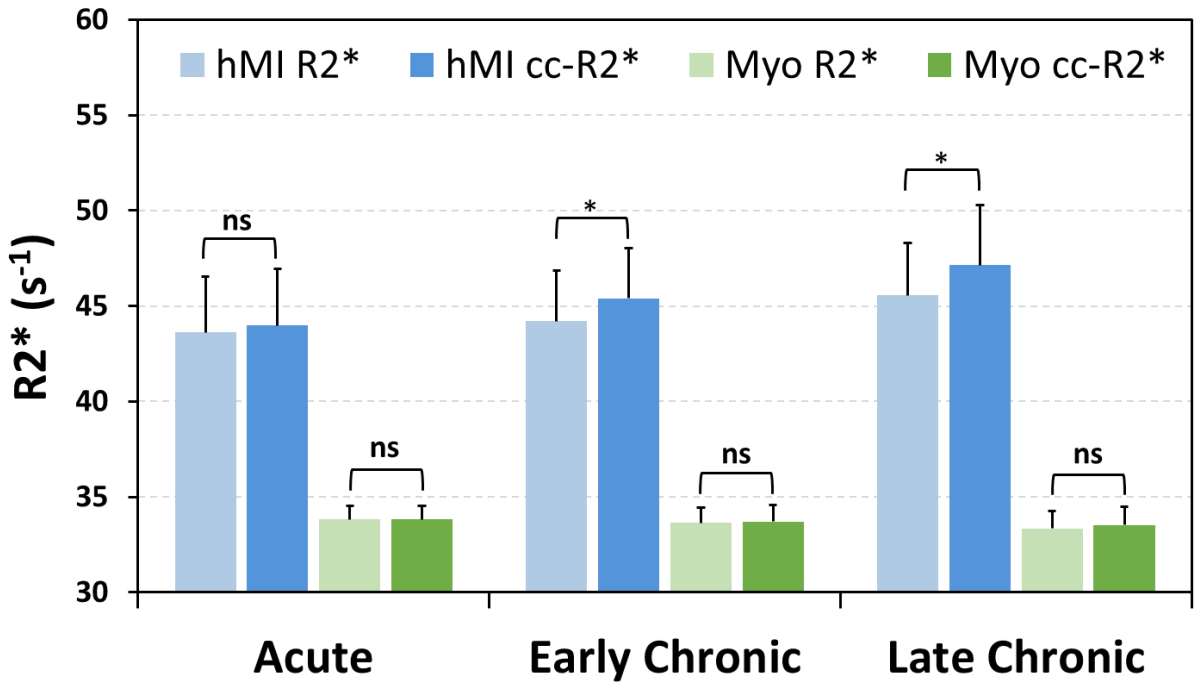

Figure 4.4. Bar-plot of R2* from direct fitting comparing to confounder-corrected R2* by water-fat separation measured in hemorrhagic myocardial infarctions (hMI) and remote myocardium (Myo) regions. Results were plotted with mean ± SEM as listed in Table 4.1. Significant differences were found between hMI R2* and hMI CC-R2* in early and late chronic phases of MIs (* $p<0.05$). Differences between other groups were not significant (ns).

Correlation between cc-R2* and PDFF of hemorrhagic MI territories on day 3, week 8 and month 6 were shown in Figure 4.5. No correlations were found between cc-R2* and PDFF in acute phase of MI ($y = 1.5 + 0.0080x$, $r^2 = 0.16$, $p = 0.38$). Moderate correlations were found between cc-R2* and PDFF in early chronic phase of MI ($y = -0.33 + 0.063x$, $r^2 = 0.64$, $p<0.01$). Strong correlations were found between cc-R2* and PDFF in late chronic phase of MI ($y = -3.7 + 0.19x$, $r^2 = 0.87$, $p<0.01$).

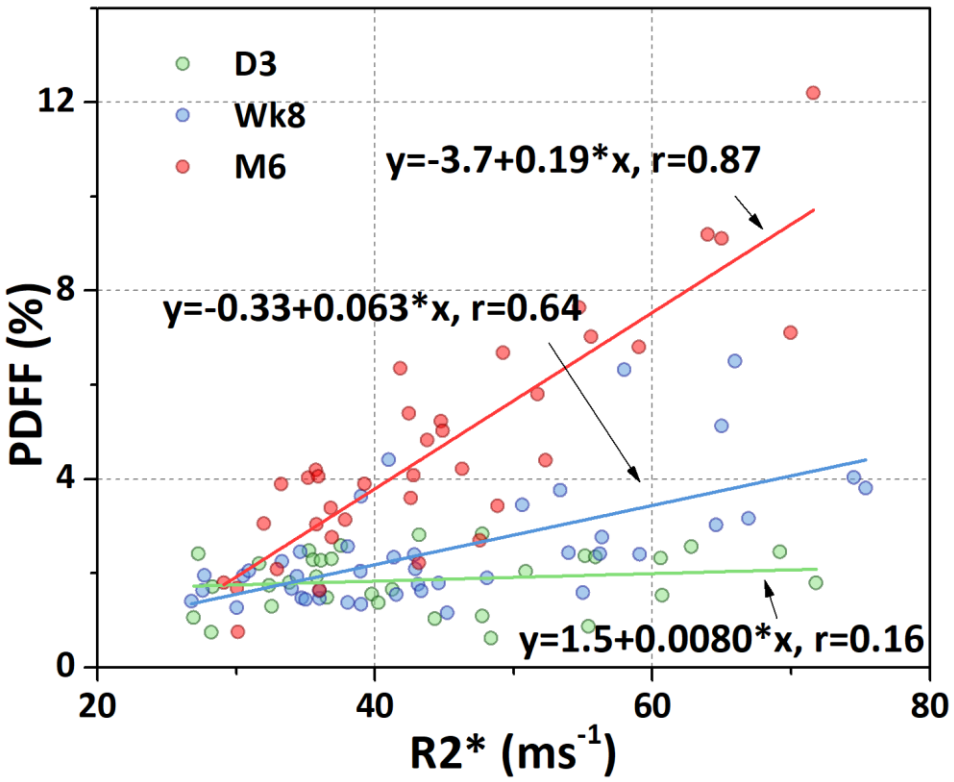

Figure 4.5. Linear regression between CC-R2* and PDFF in acute (D3, green line, $y = 1.5 + 0.0080x$, $r2 = 0.16$, $p = 0.38$), early chronic (Wk8, blue line, $y = -0.33 + 0.063x$, $r2 = 0.64$, $p<0.01$), and late chronic phases (M6, red line, $y = -3.7 + 0.19x$, $r2 = 0.87$, $p<0.01$) of MIs.

4.4 Discussion

According to the simulation (grey line in Figure 4.1), signal intensity that lacks phase information does not necessarily follow a standard T_2* decay with increasing echo times because of phase oscillation originating from chemical shift. The amplitude of the chemical shift induced by the oscillation will increase if fat content increases. As a result, T_2* fittings may be biased and less reliable (see red line in Figure 4.1). Based on the simulation, all in-phase, all out-of-phase, or echoes apart by one in-phase cycle (2.48 ms as per Figure 4.1) are preferred choices to avoid unwanted chemical shift oscillation. However, there are a number of practical considerations, which can limit these conditions from being realized. First, under certain imaging requirements such as imaging resolution, bandwidth, FOV, application of flow compensation, it may be difficult to acquire multi-gradient-echo images at TEs exactly apart by one in-phase cycle. Second, the simulation in Figure 4.1 assumes the ideal condition with no noise or inter-voxel field inhomogeneity, which is hardly the case in-vivo especially in hemorrhagic MI T_2* scans with long TEs. With disturbance from noise or significant field inhomogeneity, echo times when water and fat signals are on resonance will be hard to determine. Third, studies have shown that fatty tissues often contain different types of chemical bonds which leads to multiple peaks in spectrometry [82, 129]. With multiple fat peaks contributing to heterogenous chemical shifts, the voxel signal intensity can be much more complicated (Figure 4.6). Hence, the in-phase or out-of-phase echoes will inevitably lose efficiency. It's worth mentioning that the confounded T_2* by fat signals may not necessarily be overestimated. Green line in Figure 4.6 shows a T_2* fitting curve with magnetization at 6 TEs from 2.2 to 13.2 with 2.2 ms interval. From the T_2* fitting, T_2* relaxation time was 9.92 ms with r^2 of 0.98. At these TEs, a dramatically underestimated T_2* was fitted even with high goodness of fitting. When appropriate measures are not taken to minimize the

contribution from chemical shift, the choice of TEs determine whether a T_2* relaxation by mono-exponential fitting is over-or under-estimated. Specifically, T_2* will be overestimated if short TEs are chosen closer to in-phase echoes and long TEs are chosen closer to out-of-phase echoes which will add the signal loss from phase difference between water and fat to the relaxation decay leading to a faster T_2* decay curve. On the contrary, T_2* will be underestimated if greater signal loss from phase difference between water and fat results in early echoes.

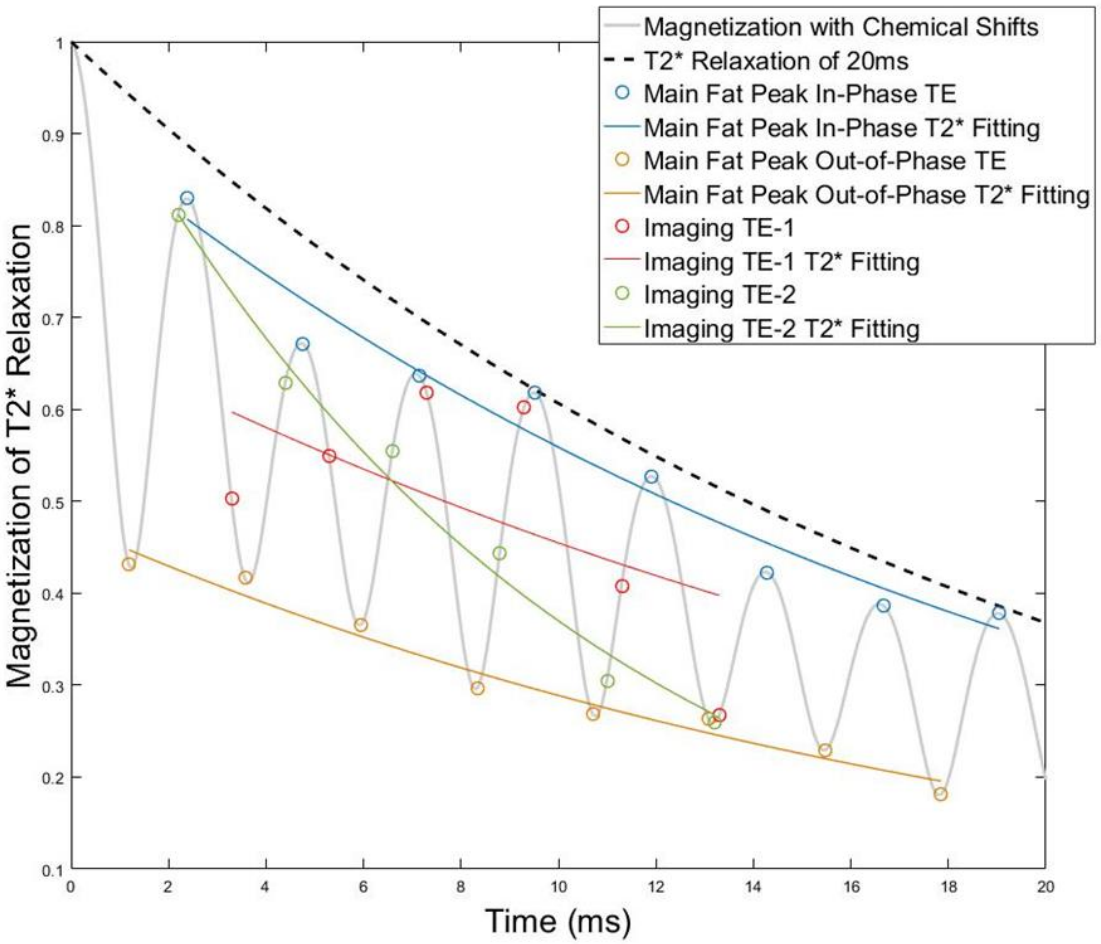

Figure 4.6. Simulation of T_2* relaxation with chemical shift. Overall initial magnetization = 1, overall fat proton density = 0.3 (fat component density: CH_2 = 0.75, chemical shift = 420HZ; CH_2COOR = 0.17,

chemical shift = 318Hz; CH=CH = 0.08, chemical shift = -94Hz [82, 129, 130]). Main fat peak in-phase T_2* fitting: T_2* = 20.74 ms, r^2 = 0.95. Main fat peak out-of-phase T_2* fitting: T_2* = 20.15 ms, r^2 = 0.96. Imaging echo-1 T_2* fitting: T_2* = 24.59 ms, r^2 = 0.20. Imaging echo-2 fitting: T_2* = 9.92 ms, r^2 = 0.98.

In animal studies, fat infiltration was observed to progressively increase from acute phase of MI to early and chronic phases of MI (Figure 4.3) and correlated with iron deposition (Figure 4.5). In consistent with simulations, R2* values were underestimated on direct fitting of multi-gradient-echo T_2* images comparing to those from confounder-corrected R2* maps after separation of water and fat signal in early and late chronic phases of MIs when fat infiltration as observed. Higher bias of R2* were found in late chronic phase of MIs when more fat was observed.

4.5 Conclusion

Fat was observed in chronic MI zones. According to results of R2* measurement, iron quantification can be biased and unreliable with the presence of fat. It is necessary to correct for fat induced chemical shifts in assessment of intramyocardial hemorrhage in chronic phases of MIs.

Chapter 5: Development of 3D fully ungated free breathing T_2* mapping technique using a low-rank tensor framework

5.1 Introduction

As described in Chapter 1, the clinical used T_2* imaging is based on a 2D breath-held, ECG-triggered, segmented, multi-gradient-echo sequence. However, it has important shortcomings. For example, breath-hold is not feasible in myocardial infarction patients who find it difficult to hold their breath. ECG triggering is unreliable in patients with irregular heart rate induced by heart diseases. Furthermore, resolution in through plane direction is limited (6 – 8 mm) in 2D MRI images which can reduce sensitivity and accuracy in quantifying local iron overload such as intramyocardial hemorrhage. There have been published studies on free-breathing cardiac T_2* techniques such as respiratory motion-corrected averaging and gradient-echo echo-planer imaging (GRE-EPI) to address the first issue. But there haven't been any developed techniques to evaluate cardiac T_2* without ECG-gating or with higher resolution at 3T MR system.

In this Chapter, we developed a fully ungated 3D cardiac multi-gradient-echo T_2* mothed addressing all the issues above based on a low-rank tensor (LRT) framework. The LRT method requires no breath-holding or ECG-gating. And as a benefit of 3D acquisition, the LRT method has enabled a higher imaging resolution at 3T.

5.2 Method

5.2.1 Sequence design and Sampling pattern

A continuous randomized Gaussian-distributed Cartesian k-space distribution pattern is used to avoid synchronization between sampling and periodic motion. As shown in Figure 5.1, sampling pattern follows a Gaussian variable density distribution along both phase (ky) and partition (kz)

encoding directions. In this way, the center of k-space, which contains most imaging contrast information, will be densely sampled while the edge of k-space is under sampled. The order of k-space lines will follow a randomized pattern. Each readout consists of 8 gradient echoes. K-space center line (shown as blue lines in Figure 5.1) is collected interleaved with every other readout line (shown as black lines in Figure 5.1). A subset data with k-space center lines will be used to resolve temporal dynamics $\mathbf{U}_{\mathrm{R}}$, $\mathbf{U}_{\mathrm{C}}$, therefore k-space center lines are collected more frequently.

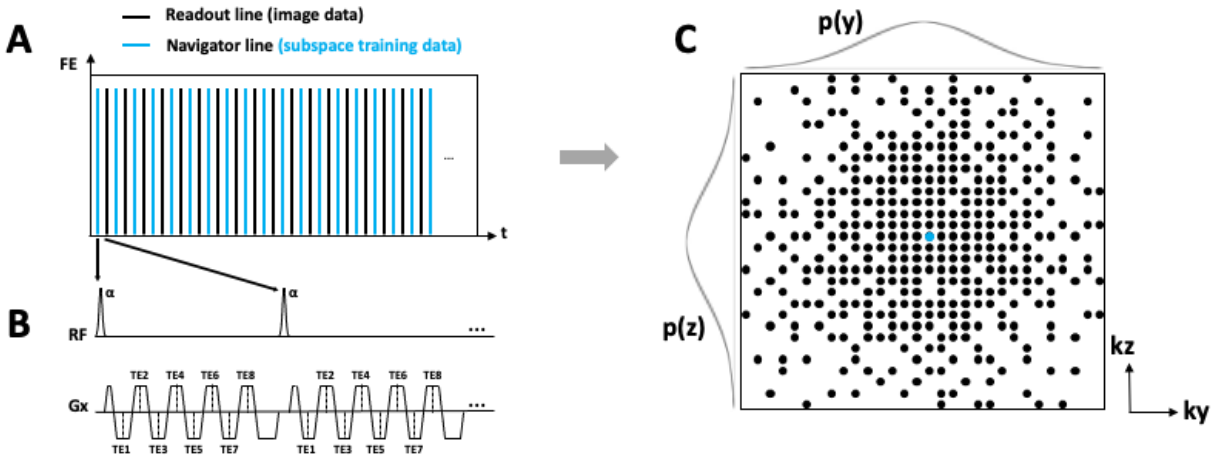

Figure 5.1. Illustration of sequence design and k-space sampling. A. Continuous k-space readout along frequency encoding (FE) direction. B. Eight echoes will be acquired at each readout. C. Gaussian variable density k-space sampling pattern on ky-kz plane.

5.2.2 Imaging Model and Reconstruction

Based on the LRT framework, cardiovascular T_2* image A is represented as a 4-dimensional function $\mathrm{I}(\mathbf{x}, \mathrm{R}, \mathrm{C}, \mathrm{T})$ of spatial location $\mathbf{x}$ and 3 time dimensions which are respiratory motion R, cardiac motion C and T_2* decay T as:

$$\mathbf{A}_{(1)} = \mathbf{U}_{\mathbf{x}}\mathbf{G}_{(1)}(\mathbf{U}_{\mathrm{R}} \otimes \mathbf{U}_{\mathrm{C}} \otimes \mathbf{U}_{\mathrm{T}})^{\mathrm{T}} \tag{5.1}$$

where the ⊗ operator denotes the Kronecker product. The subscript (n) (in this equation (1)) denotes mode-n unfolding of the tensor into a matrix. The factor matrix $\mathbf{U_x} \in \mathbb{C}^{J \times L_0}$ contains L_0 spatial basis functions with J voxels each. Each factor matrix $\mathbf{U_R}, \mathbf{U_C}, \mathbf{U_T}$ contains basis functions for the time dimension R, C and T. G is the core tensor governing the interaction between factor matrices.

A is reconstructed in factored form using an explicit tensor subspace constraint:

$$\widehat{\mathbf{U}}_\mathbf{x} = \arg\min_{\mathbf{U_x}} \|\mathbf{d} - \Omega([\mathbf{FSU_x}]\mathbf{\Phi})\|_2^2 + \mathrm{R}(\mathbf{U_x}), \tag{5.2}$$

where $\mathbf{\Phi}$ is constructed from the temporal factor matrices as $\mathbf{\Phi} = \mathbf{G}_{(1)}(\mathbf{U_R} \otimes \mathbf{U_C} \otimes \mathbf{U_T})^{\mathrm{T}}$.

An interleaved subset of training data which consists of k-space center lines is acquired to reconstruct motion states of the image tensor by a small-scale LRT completion.

$$\hat{\chi}_{\mathrm{tr}} = \arg\min_{\chi_{\mathrm{tr}}} \|\mathbf{d}_{\mathrm{tr}} - \Omega_{\mathrm{tr}}(\chi_{\mathrm{tr}})\|_2^2 + \lambda \sum_{n=1}^{4} \left\|\mathbf{X}_{\mathrm{tr},(n)}\right\|_* + \mathrm{R}(\chi_{\mathrm{tr}}) \tag{5.3}$$

Once the tensor is completed, the matrix Φ can be extracted from $\hat{\chi}_{\mathrm{tr}}$ by higher-order singular value decomposition (HOSVD).

5.2.3 Animal Study

The proposed fully ungated free-breathing 3D LRT T_2* imaging technique was first tested on animals. According to the protocol approved by the Institutional Animal Care and Use Committee, swines (n = 10, 28 – 32 kg, all female) were recruited and scanned at 3.0T MRI system (Verio, Siemens). Prior to MRI scans, all animals were intubated and anesthetized with isoflurane (1-1.5 %/volume). Conventional breath-held, ECG-triggered 2D multi-gradient-echo short-axis T_2* images of whole left ventricle were acquired. All 2D T_2* images were acquired at mid to late diastole with 7 segments. With the same image resolution, fully ungated whole heart 3D LRT data

was acquired with free breathing. A set of high through-plane resolution fully ungated 3D LRT data was also acquired with free breathing covering middle of left ventricle. Detailed image parameters of both approaches are shown in Table 5.1.

Table 5.1. Imaging parameters.

	Conventional 2D	Proposed 3D LRT
FOV (mm)	300 × 300	300 × 300
Matrix size	192 × 192	192 × 192 × 14
Resolution (mm^3)	1.6 × 1.6 × 6.0	1.6 × 1.6 × 6.0 1.6 × 1.6 × 3.0 (High-Res)
Flip angle (°)	18	8
TE (ms)	Baseline: 1.41, 3.38, 5.39, 7.40, 9.41, 11.42, 13.43, 15.44 Post-Contrast: 1.41, 2.64, 3.87, 5.10, 6.33, 7.56, 8.79, 10.02	
TR (ms)	1 R-R interval	17.11(Baseline) 11.70 (Post-Contrast)
Bandwidth (Hz/Pixel)	1184	1184
Segments	7	--
GRAPPA accelerate factor	2	--
Overall acquisition time	~10 min	~5 min

After baseline scans, iron-oxide contrast was given to animals (n = 5) by intravenous infusion (Ferumoxytol injection, Feraheme, 4ml/kg, 1-20 dilution, 100ml/hour infusion rate). Post-contrast conventional 2D T_2* images were acquired at middle ventricle post infusion. Fully ungated, free breathing, 3D LRT data were acquired with regular and high resolutions. TEs of post-contrast T_2* images were adjusted based on faster T_2* decay (Table 5.1).

5.2.4 Human Study

Human study was approved by Institutional Review Boards. All subjects gave written informed consent before participating in the study. Healthy volunteers (n = 11) were recruited and scanned at 3.0T MR system (Verio, Siemens). Following localizers and whole-heart shimming, conventional short-axis, breath-held, ECG-gated, multi-gradient-echo T_2* images were acquired. Same resolution, fully ungated 3D LRT T_2* data was acquired with free breathing covering whole left ventricle. High resolution, fully ungated 3D LRT T_2* was acquired covering middle ventricle.

5.2.5 Image Analysis

All 3D LRT T_2* images were reconstructed using MATLAB.

Image quality of native T_2*-weighted images was assessed by 2 experienced reviewers based on a 5-point scale: 1 – very poor image quality, unable to identify myocardium; 2 – less than adequate image quality with substantial artifact in myocardium region; 3 – adequate image quality with moderate artifact; 4 – good image quality with minimal artifact; 5 – Excellent image quality with no significant artifact. A consensus image quality score between 2 reviewers were recorded for each T_2*-weighted images.

Coefficient of variation was evaluated in septum on each short-axis T_2*-weighted images as standard deviation of signal intensity (σ_{SI}) over mean signal intensity (SI) of the region of interest.

$$\mathrm{COV} = \frac{\sigma}{\mathrm{SI}} \tag{5.4}$$

Short-axis T_2* maps were generated from T_2*-weighted images with adequate image quality (image score > 2) in MATLAB by mono-exponential pixel-wise fitting. Septal T_2* were recorded for comparison.

5.2.6 Statistical Analysis

Image quality scores and COV were compared between conventional 2D approach and proposed 3D LRT approach using Wilcoxon signed rank test. Paired t-test was used to test difference between average T_2* measured from T_2* maps by different approaches. Linear regression analysis was performed to evaluate correlation between T_2* measured from two different imaging approaches. Bland-Altman analysis was performed to determine the bias in measurement between different imaging approaches. Statistical significance was set at $p<0.05$.

5.3 Results

5.3.1 Animal Study

In animal studies, scan time of a full stack of 2D short-axis breath-holding ECG-gated cardiac T_2* images is around 10 minutes including recovery between breath-holds. At baseline, with the same resolution as conventional 2D approach, a total of 14 partitions were acquired for 3D LRT data covering the whole LV. Total acquisition time for each LRT data at baseline is 4 minutes and 38 seconds. Respiratory motion was clustered into 4 motion states and cardiac motion was clustered into 16 motion states. The under-sampling rate of LRT data relative to a full tensor is 3.1%. High-resolution LRT data was acquired at through plane resolution of 3 mm, same temporal resolution and under-sampling rate. Post-contrast LRT data was acquired with adjusted echo times (Table 5.1), temporal resolution of 23.40 ms, and same under-sampling rate as pre-contrast studies for all LRT data.

5.3.1.1 Image Quality and COV

Figure 5.2 shows a set of T_2* images from conventional 2D and proposed 3D LRT imaging methods from animal studies at baseline. Same-resolution T_2*-weighted images of base, middle

and apex of left ventricle along with T_2* maps were shown. At the same resolution, T_2* images reconstructed from proposed LRT approach showed better image quality than that of conventional 2D approach group. Image quality score in LRT approach is 3.7 ± 0.3 and the average score in conventional 2D approach is 3.3 ± 0.4 ($p<0.05$). COV was reduced on 3D LRT reconstructed T_2* images within region of interest in septum. Average COV measured on conventional 2D T_2* images is 0.10 ± 0.04 which is significantly higher than that on 3D LRT T_2* images (0.06 ± 0.02, $p<0.05$) at the same resolution.

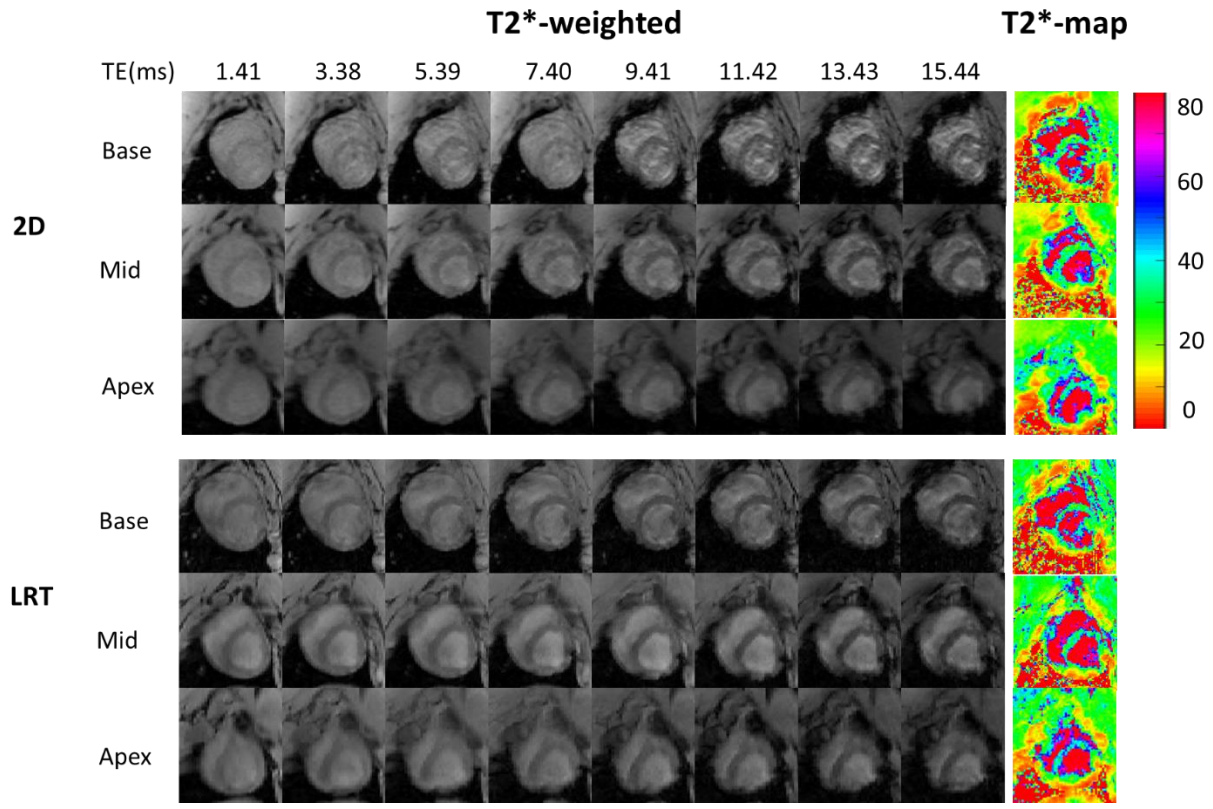

Figure 5.2. Representative T_2*-weighted images acquired at the same resolution by conventional 2D approach and proposed LRT approach and corresponding T_2* maps of base, mid and apex of left ventricle of an animal.

High-resolution T_2* images acquired by 3D LRT imaging approach are shown in Figure 5.3. Average image quality score of high-resolution T_2* images by LRT approach is 3.8 ± 0.4 which is significantly higher than conventional 2D group ($p<0.05$). Lower coefficient of variation (0.07 ± 0.03, $p<0.05$) was also found on high-resolution T_2* images reconstructed by 3D LRT framework.

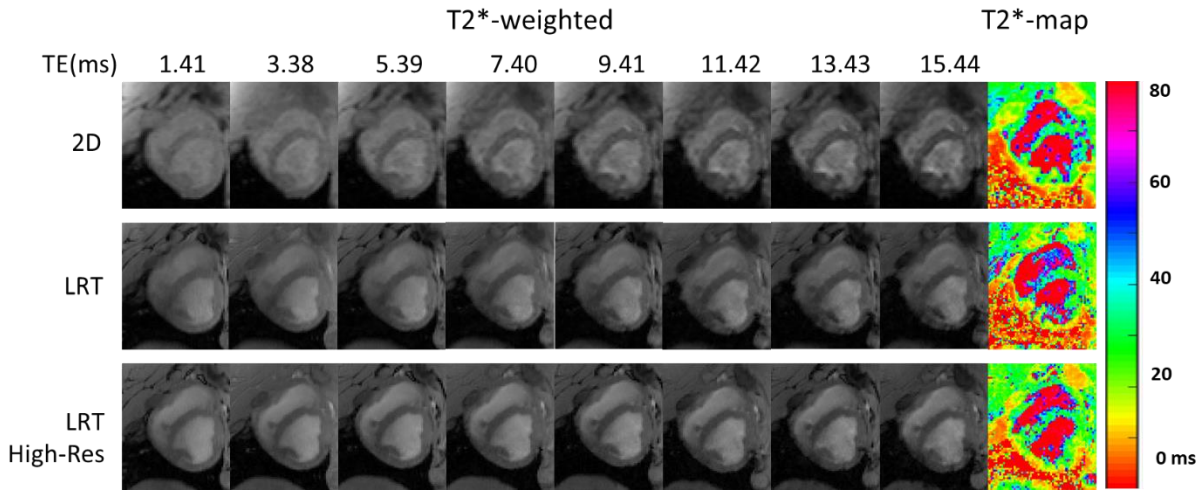

Figure 5.3. Representative T_2*-weighted images acquired by conventional 2D approach and proposed LRT approach with same and high resolution, and corresponding T_2* maps of middle ventricle of an animal.

5.3.1.2 T_2* measurement

Figure 5.4 shows example T_2* images acquired after iron-oxide contrast. T_2*-weighted images and T_2* maps acquired by conventional 2D, proposed 3D LRT and high-resolution 3D LRT imaging approach are demonstrated. Due to infusion of iron-oxide, myocardial T_2* was significantly reduced as shown in T_2* maps in Figure 5.4.

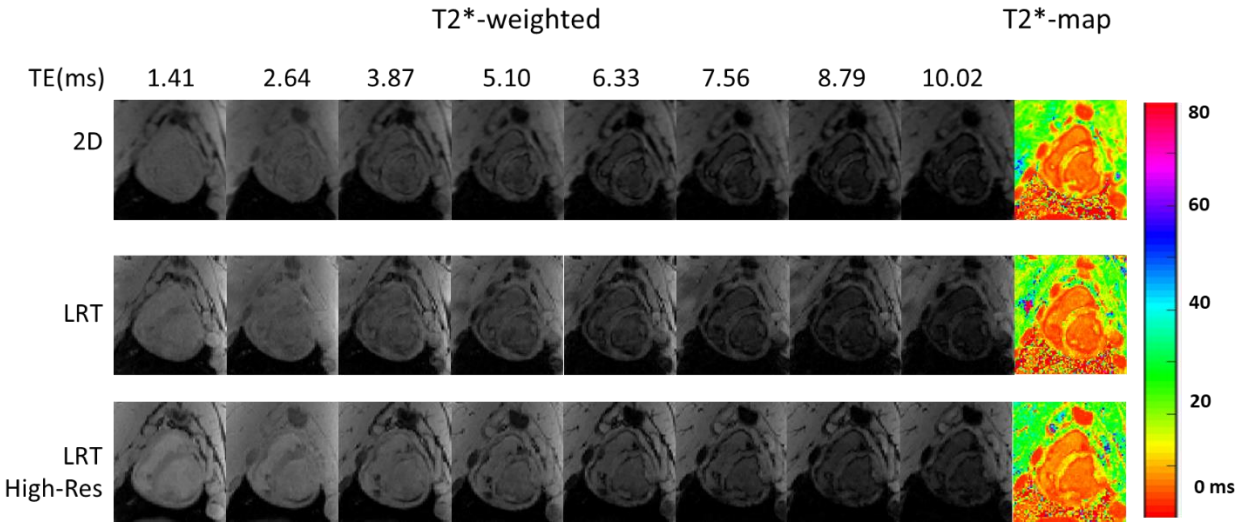

Figure 5.4. Post-contrast T_2*-weighted images and T_2* maps of an animal.

In animal studies, no differences were found between T_2* values measured from conventional 2D approach and proposed 3D LRT approach in both pre- and post-contrast conditions despite different resolutions. At baseline, average T_2* of septum from conventional 2D approach is 28.4 ± 1.8 ms and average T_2* measured from images in proposed 3D LRT group at the same resolution is 28.0 ± 1.6 ms ($p = 0.67$), at high resolution is 28.3 ± 2.1 ms ($p = 0.38$). Post-contrast T_2* measured from images by conventional 2D approach is 12.0 ± 1.3 ms and 11.6 ± 1.5 ms by proposed 3D LRT approach ($p = 0.76$) at the same resolution, and 11.2 ± 1.7 ms at high resolution ($p = 0.21$).

Linear regression was performed with both pre- and post-contrast results. At the same resolution, T_2* between two approaches showed excellent correlation in Figure 5.5A ($y = 0.99x - 0.17$, r2 =

0.99, $p<0.05$). Bland Altman plot with mean of differences and 95% confidence interval is shown in Figure 5.5B. T_2* values from two approaches showed excellent agreement with average bias of -0.39 ± 0.81 ms. Linear regression between T_2* from conventional 2D approach and high-resolution 3D LRT approach is shown in Figure 5.5C. Excellent correlation was found between T_2* values measured by two approaches ($y = 1.02x – 0.82$, $r2 = 0.96$). Bland Altman plot with mean of differences and 95% confidence interval is shown in Figure 5.5D. Excellent agreement was found between T_2* values from conventional 2D approach and high-resolution LRT approach. Average bias between T_2* is -0.05 ± 1.5 ms.

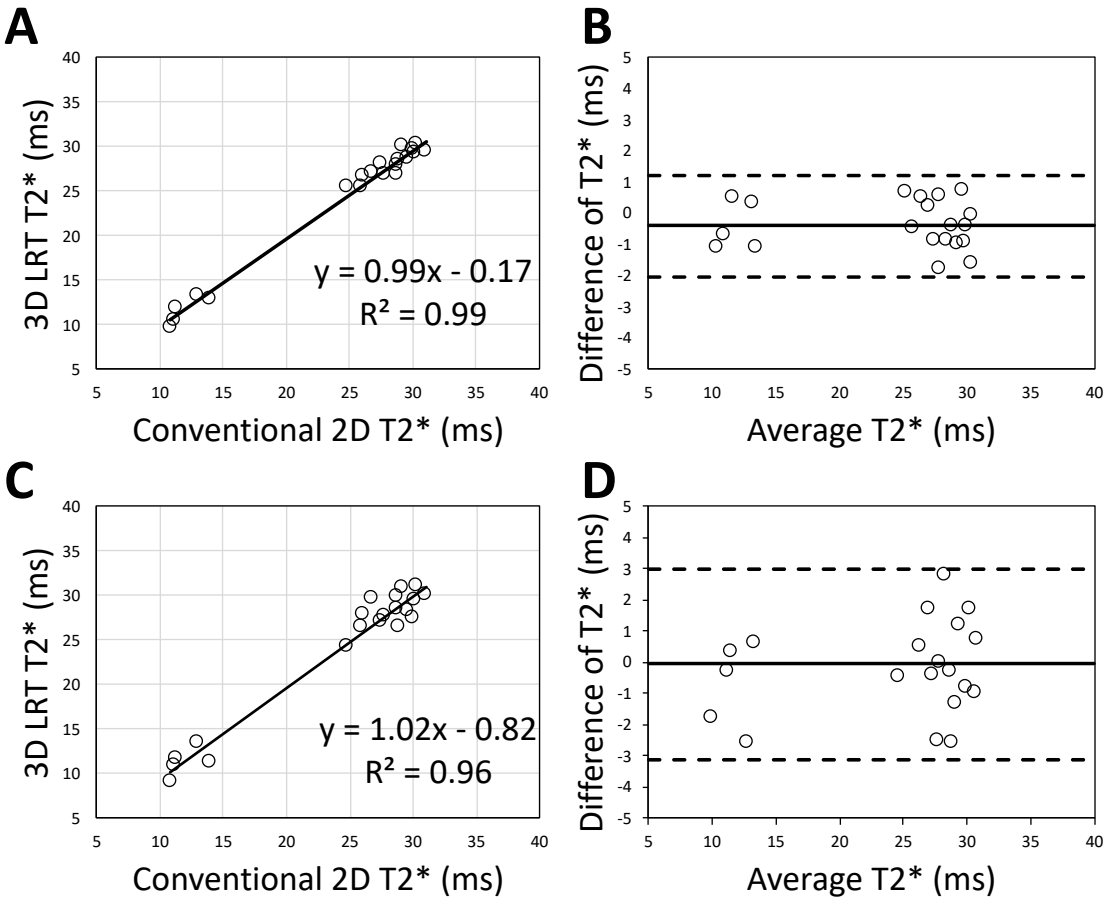

Figure 5.5. Animal Study: A. Regression of T_2* measured from images by conventional 2D approach and proposed 3D LRT approach at the same resolution. B. Bland-Altman plot of difference of T_2* measured from two approaches at the same resolution. C. Regression of T_2* measured from images by conventional 2D approach and proposed 3D LRT approach at high resolution. B. Bland-Altman plot of difference of T_2* measured from two approaches at high resolution.

5.3.2 Human Study

In human studies, it takes 10 to 12 minutes to acquire a full stack of breath-holding 2D cardiac T_2* images covering whole LV based on size of LV, heat rate and recovering time after each breath-

hold. At the same through-plane resolution, a total of 16 partitions were acquired in each LRT scan in human study to cover whole LV. Total acquisition time of proposed free-breathing 3D LRT approach is 5 minutes and 15 seconds.

5.3.2.1 Image Quality and COV

Figure 5.6 shows representative T_2*-weighed images of a healthy volunteer imaged by conventional 2D approach and proposed 3D LRT approach at the same resolution at 3.0T. Short axis view of base, mid and apex of left ventricle are shown. T_2* maps were demonstrated on the side. All short-axis slices of T_2* images in conventional 2D and proposed 3D LRT groups were scored. At the same image resolution, higher image quality scores were found in images from proposed LRT approach. Average score of image quality of conventional 2D approach is 3.3 ± 0.3 and that of proposed 3D LRT approach is 3.7 ± 0.2 ($p<0.05$). Lower COV was found on 3D LRT T_2* images which is 0.08 ± 0.03, and COV on conventional 2D T_2* images was 0.13 ± 0.06 ($p<0.05$).

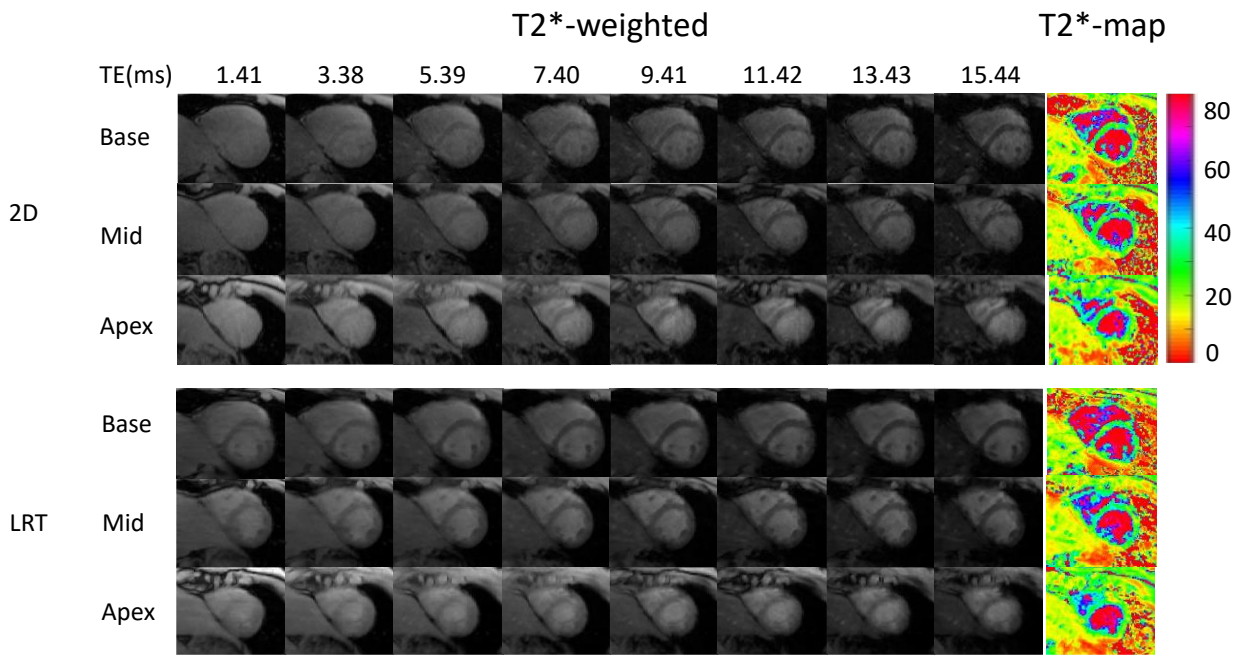

Figure 5.6. Representative T_2*-weighted images acquired by conventional 2D approach and proposed LRT approach and corresponding T_2* maps of base, mid and apex of left ventricle of a healthy volunteer.

High-resolution T_2* images acquired by 3D LRT imaging approach from a healthy volunteer are shown in Figure 5.7. Average image quality score of high-resolution T_2* images by LRT approach is 3.6 ± 0.4 which is significantly higher than conventional 2D group ($p<0.05$). SNR was found reduced as a result of increased resolution on high-resolution 3D LRT T_2* images. COV measured in septum was 0.09 ± 0.03 which is significantly lower than that from conventional 2D T_2* images.

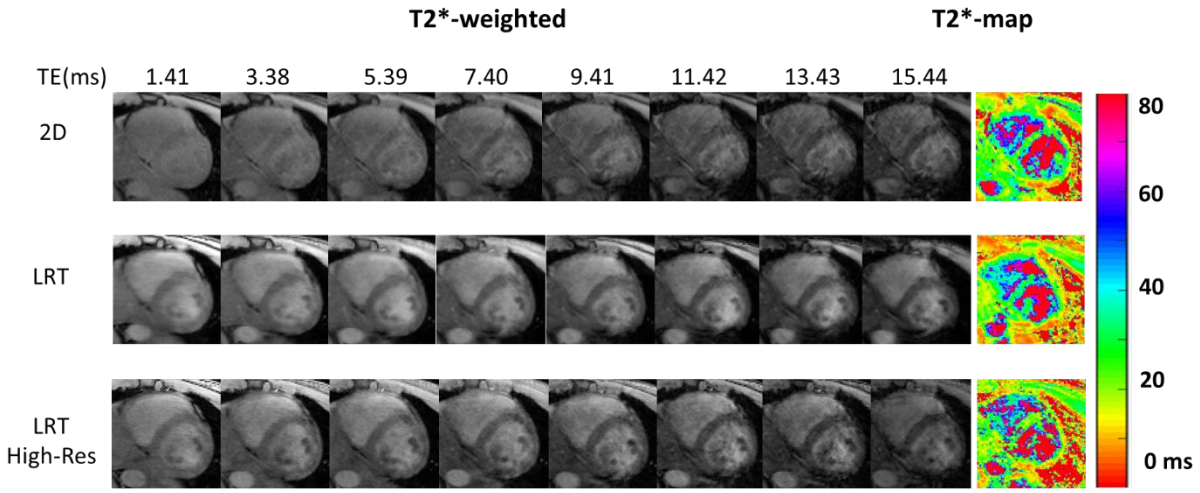

Figure 5.7. Representative T_2*-weighted images acquired by conventional 2D approach and proposed LRT approach with same and high resolution, and corresponding T_2* maps of middle ventricle of a healthy volunteer.

5.3.2.2 T_2* Measurement

In human studies, no differences were found between T_2* values from conventional 2D and proposed LRT approaches. The average T_2* of septum of volunteer from conventional 2D images was 28.8 ± 1.7 ms, and average T_2* from proposed 3D LRT images at the same resolution was 28.5 ± 1.6 ms. In high-resolution 3D LRT T_2* images, septal T_2* was 29.3 ± 1.9 ms.

5.4 Discussion

By using the low-rank tensor framework, a 3D fully ungated free-breathing multi-echo cardiac T_2* imaging technique was developed and validated both on animal and human subjects. With less time, the proposed 3D LRT approach was able to reconstruct T_2* images with similar SNR as conventional 2D T_2* images at the same resolution.

Breathing and cardiac motion is one of the most important reasons for degradation of image quality of T_2* images by conventional 2D approach. At the same resolution, the motion-resolved 3D LRT approach can provide better quality T_2* images as a result of minimizing motion artifacts in both animal and human studies.

Off-resonance caused by susceptibility difference between heart-lung interfaces is another type of artifacts which can severely affect T_2* image quality and diagnostic reliability. There hasn't been any fully effective technique to address this issue. But the susceptibility artifacts can be mitigated by increasing image resolution due to reduced intravoxel dephasing. Due to SNR trade-off, the resolution of conventional 2D cardiac T_2* imaging is limited to 6 – 8 mm of slice thickness. However, as a benefit of free-breathing 3D acquisition, high-resolution cardiac T_2* images were reconstructed using proposed 3D LRT framework. High-resolution 3D LRT T_2* images showed better image quality and lower COV than conventional 2D T_2* images.

The newly developed fully ungated free-breathing 3D LRT T_2* imaging technique is shown to be able to generate accurate T_2* maps for iron quantification in myocardium. In animal studies, iron-oxide contrast was given to animal to create myocardial iron overload imaging condition. Excellent correlation and agreement of T_2* have been found between conventional 2D approach and the proposed 3D LRT approach in pre- and post- iron-oxide contrast scans. T_2* measured from regular and high-resolution 3D LRT T_2* approach both have shown great correlation with T_2* measured from conventional 2D T_2* images. However, we did notice some baseline T_2* maps by high-resolution 3D LRT T_2* images to be noisy which increased standard deviation of bias of T_2* values between conventional 2D T_2* and high-resolution 3D LRT T_2* images in Bland-Altman plot.

5.5 Conclusion

To conclude, the proposed fully ungated, free-breathing T_2* approach can overcome image artifacts caused by motion due to failure of breath-holding and ECG gating. It is reliable to produce accurate T_2* maps for assessment of intramyocardial iron overload. The proposed 3D approach allows a high resolution cardiac T_2* imaging which provides better image quality and clinical potentials.

Chapter 6: Application of fully ungated free-breathing 3D LRT cardiac T_2* in imaging of intramyocardial hemorrhage

6.1 Introduction

In Chapter 5, a fully ungated free-breathing 3D cardiac T_2* technique was developed based on a low-rank tensor framework. The newly developed 3D LRT cardiac T_2* imaging technique was tested on healthy volunteers and animals. Results showed that, comparting to conventional 2D breath-hold ECG-gated cardiac T_2* imaging mothed, the proposed 3D LRT approach can provide T_2* images with better image quality as a result of cardiac and respiratory motion resolvent both in human and animal studies. Myocardial T_2* values measured from the proposed method were in excellent agreement with T_2* measured from conventional method before and after iron-oxide infusion. Furthermore, as benefit from a 3D acquisition, high-resolution cardiac T_2* images were acquired by the proposed LRT approach. Even though with a trade-off of signal to noise ratio, T_2* images with higher resolution can still provide equivalent image quality and T_2* values comparing to conventional 2D T_2* method.

In this Chapter, to further validate the diagnostic capability, the newly developed fully ungated free-breathing 3D LRT cardiac T_2* imaging technique was applied on imaging of intramyocardial hemorrhage using a well-established animal model.

6.2 Method

6.2.1 Animal Study

According to the protocol approved by the Institutional Animal Care and Use Committee, hemorrhagic MIs were created in canines (n=9, all female) by 3 hours of LAD occlusion, followed by reperfusion. Prior to MRI scans, all animals were intubated and anesthetized with isoflurane (1-

1.5 %/volume). Cardiac MRI scans were performed 3 to 5 days after reperfusion in acute phase of MI. One heart was explanted after acute MRI scan and kept in 10% formaldehyde solution. Ex-vivo imaging was performed for validation.

6.2.2 Image acquisition

After localizer, contiguous whole heart short-axis slice-matched conventional multi-gradient echo T_2*, 3D LRT multi-gradient echo T_2*, high-resolution 3D LRT multi-gradient echo T_2* data were acquired before injection of contrast. Gd contrast (Magnevist, Bayer AG, Berlin, Germany) was given to animals at 0.2 mmol/kg. Full stack of contiguous short-axis slice-matched short-axis late-gadolinium-enhancement images were acquired 10 to 15 minutes after injection. Other than LRT T_2* data (with regular resolution and high resolution), all cardiac MRI images were acquired with breath-held, ECG-gated, 2D acquisition. LRT T_2* data were acquired with 3D acquisition at free-breathing and no ECG gating. Ex-vivo scan was performed by immersing the explanted heart in 10% formaldehyde solution. Detailed imaging parameters are reported in Table 6.1.

Table 6.1. Imaging parameters

	Conventional 2D	Proposed 3D LRT
FOV (mm)	300 × 300	300 × 300
Matrix Size	192 × 192	192 × 192
Resolution (mm^2)	1.6 × 1.6 × 6.0	1.6 × 1.6 × 6.0 1.6 × 1.6 × 3.0
Flip Angle (º)	18	8
TE (ms)	1.41, 3.38, 5.39, 7.40, 9.41, 11.42, 13.43, 15.44	
TR (ms)	1 R-R interval	17.11
Segments	7	-
Bandwidth (Hz/Pixel)	1184	1184
Imaging time	5-8 seconds/slice	~5 minutes/stack

6.2.3 Image reconstruction

All LRT T_2* images were reconstructed based on the low-rank tensor framework described in Chapter 5 using MATLAB. Based on size (20 – 25 kg) and heart rate of dogs (89.4 ± 12.7 bpm), respiratory motion was binned into 4 phases and cardiac motion was binned into 18 phases.

6.2.4 Image Analysis

Image quality of all T_2*-weighted images was assessed by 2 experienced reviewers based on criteria described in Chapter 5.

Myocardial infarction was identified by mean + 5SD on post-contrast LGE images. Intramyocardial hemorrhage was identified on T_2*-weighed images (TE = 13.43 ms) as regions within MI territories, with mean signal intensity 2 standard deviation lower than that of remote myocardium. IMH extent was evaluated as volume% of whole LV.

T_2* maps were generated from T_2*-weighted images with adequate image quality (image score > 2) in MATLAB by mono-exponential pixel-wise fitting. T_2* of remote myocardium and hemorrhage regions were recorded and compared between conventional 2D T_2* and proposed 3D LRT T_2* approaches.

Diagnostic accuracy for IMH detection by conventional 2D T_2*, proposed 3D LRT T_2*, and high-resolution 3D LRT T_2* images were assessed by evaluating diagnostic sensitivity and specificity using ex-vivo T_2* as ground truth. Each short-axis T_2* image was segmented into six regions as anterior, anteroseptal, inferoseptal, inferior, inferolateral and anterolateral [131]. Each region was segmented into 3 layers as endocardium, myocardium, and epicardium. As ground truth, the ex-vivo heart was segmented and registered to in-vivo images. Each region is considered positive if over 5% of the entire region was highlighted by mean-2SD criteria, otherwise, it was considered

negative. Criteria of mean-2SD, mean-3SD, mean-4SD, mean-5SD, mean-6SD were used as different thresholds for hemorrhage detection in in-vivo T_2* images.

6.3 Results

Figure 6.1 shows an example of imaging results. Conventional 2D, proposed 3D LRT and high-resolution T_2*-weighted images with 8 different echoes and T_2* maps of hemorrhage were showed with LGE image as reference of MI territory.

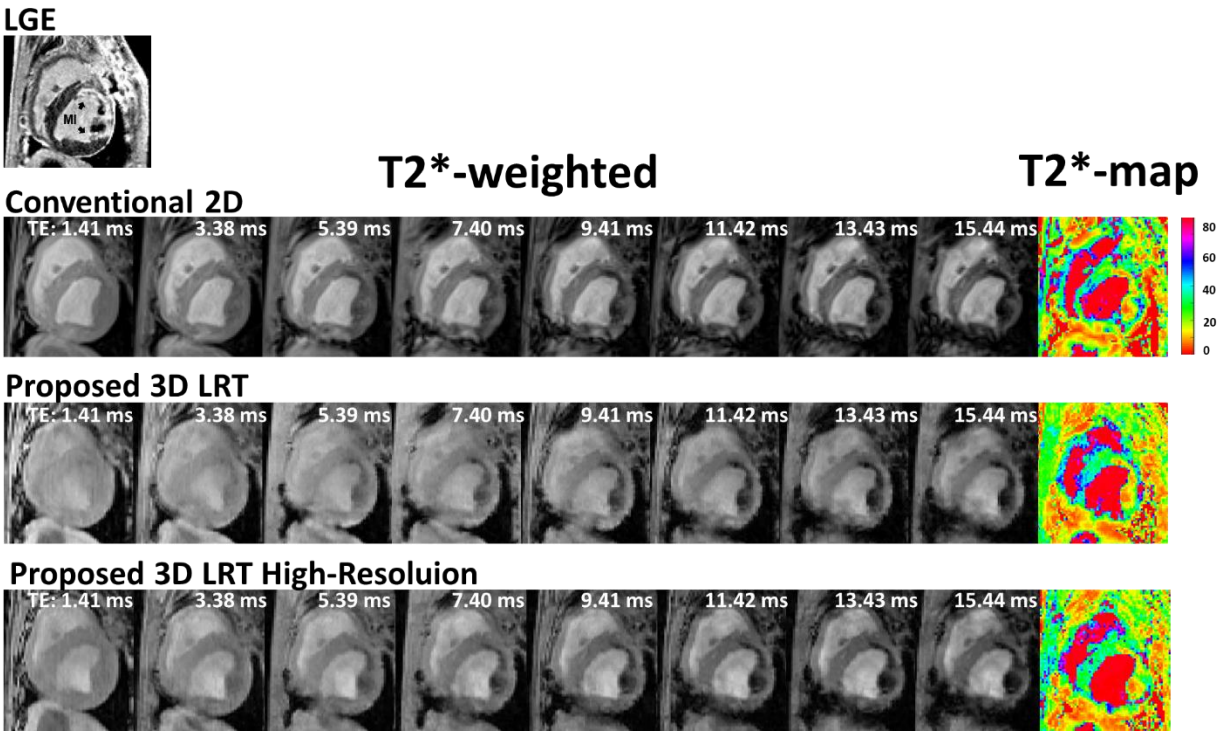

Figure 6.1. Example of multi-echo T_2*-weighted images and T_2*-maps by conventional 2D, proposed 3D LRT and high-resolution 3D LRT approaches. Slice-matched LGE image is displayed on top as reference of MI.

6.3.1 Image Quality

By scoring all T_2* images on a 1-5 scale, image quality in conventional 2D groups is 3.5 ± 0.5, which is lower than that in proposed 3D LRT group (3.8 ± 0.3, $p<0.05$). The highest image quality scores were found in high resolution 3D LRT group with average image quality of 3.9 ± 0.5 ($p<0.05$).

Table 6.2. Results of image quality, relative SNR and T_2* of IMH and remote myocardium.
* denotes significant difference of image quality comparing to conventional 2D approach.

	Conventional 2D	Proposed 3D LRT	High-res 3D LRT
Image Quality	3.5 ± 0.5	3.8 ± 0.2*	3.9 ± 0.5*
T_2* of IMH (ms)	13.4 ± 3.6	13.9 ± 3.6	13.8 ± 3.5
T_2* of Remote Myocardium (ms)	28.5 ± 2.0	28.2 ± 2.1	28.6 ± 2.3

6.3.2 T_2* Measurement

T_2* of hemorrhage and remote myocardium were measured on T_2* maps from all groups and reported in Table 6.2. No difference of T_2* values of remote myocardium or hemorrhage were found between groups. Regression and Bland-Altman analysis were performed between conventional 2D and proposed 3D LRT approach at the same image resolution with both T_2* values measured in remote myocardium and hemorrhage (Figure 6.2). T_2* measured from two approaches showed excellent correlation ($y = 0.98x + 0.60$, $r^2 = 0.98$, $p<0.01$). Bland-Altman blots indicated an excellent agreement with average bias of 0.34 ± 1.11 over all T_2* measured from IMH and remote myocardium between conventional 2D and proposed 3D LRT approaches.

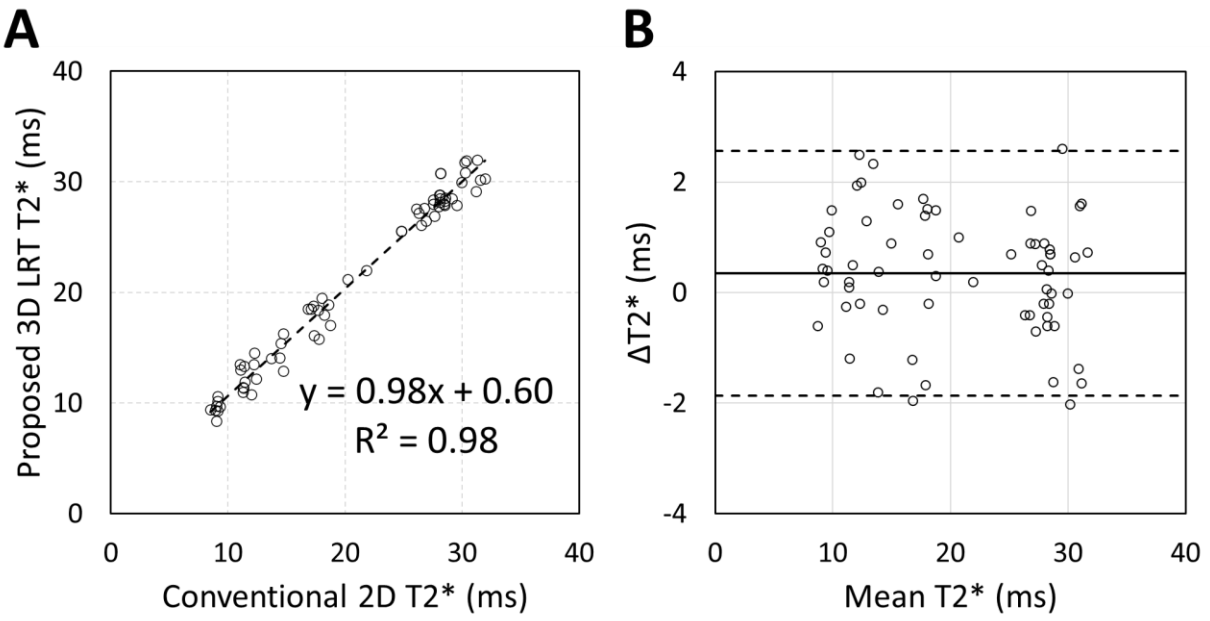

Figure 6.2. Regression (A) and Bland-Altman plots with 95% confidence interval (B) of T_2* values of IMH and remote myocardium measured on T_2* maps by conventional 2D and proposed 3D LRT T_2* imaging methods. T_2* values measured from two different T_2* imaging approaches followed linear regression of $y = 0.98x + 0.60$, $r^2 = 0.98$, $p < 0.01$. In Bland-Altman plot, average bias of T_2* between two T_2* imaging approaches was 0.34 ± 1.11 ms.

6.3.3 IMH Extent

Results of IMH extent measured from different imaging approaches were shown in Figure 6.3 as regression and Bland-Altman plots. Excellent correlation and agreement were found between conventional 2D and proposed 3D LRT groups at the same resolution. An average bias of 0.19 ± 0.64 % were found between IMH extent measured from two T_2* approaches. No significant differences of IMH extent were found between groups. Similar results were found between groups of conventional 2D T_2* and high-resolution 3D LRT T_2*. IMH extent showed excellent correlation

and agreement between groups with an average bias of 0.34 ± 0.91 % and no significant differences were found.

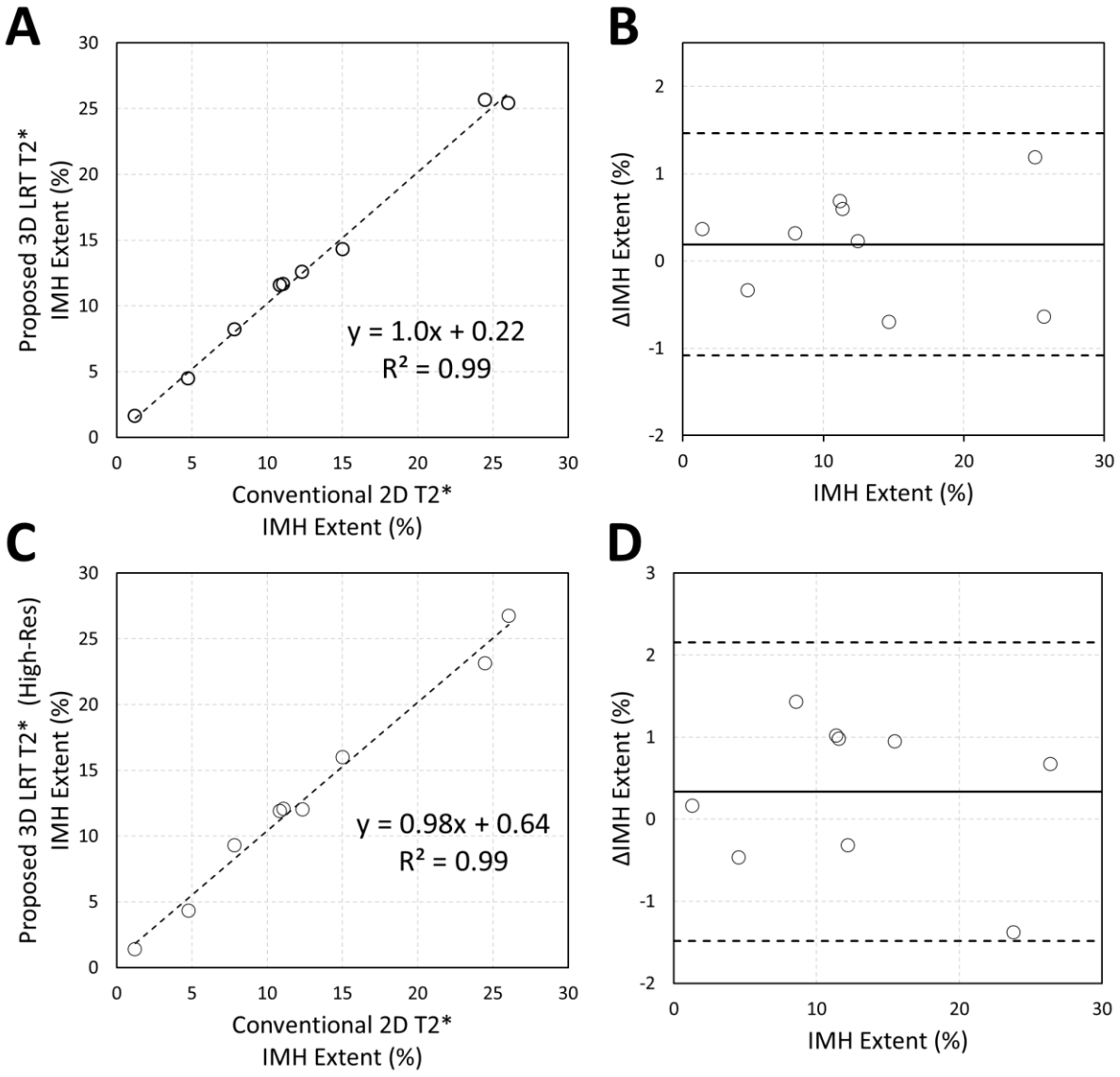

Figure 6.3. A. Linear regression (y = 1.0x + 0.22, r2 = 0.99, p<0.05) of IMH extent measured from conventional 2D T_2* and proposed 3D LRT T_2* at the same imaging resolution. **B.** Bland-Altman plot of differences of IMH extent measured from conventional 2D T_2* and proposed 3D LRT T_2* images with 95% confidence interval. Average bias of IMH extent between imaging approaches was 0.19 ± 0.64 %. **C.** Linear regression (y = 0.98x + 0.64, r2 = 0.99, p<0.05) between IMH extent measured from conventional 2D T_2* and proposed high-resolution 3D LRT T_2* images. **D.** Bland-Altman plot of differences of IMH

extent measured from conventional 2D T_2* and high-resolution 3D LRT T_2* images with 95% confidence interval. Average bias of IMH extent between the imaging approaches was 0.34 ± 0.91 %.

6.3.4 Diagnostic Accuracy

Sensitivity and specificity were analyzed for IMH detection on conventional 2D, proposed 3D LRT and high-resolution 3D LRT T_2* images using ex-vivo T_2* as ground truth. Results were shown as an ROC plot in Figure 6.4. The area under the curve (AUC) were calculated. AUC of conventional 2D approach is 0.67, of 3D LRT approach is 0.76 and of high-resolution 3D LRT approach is 0.79.

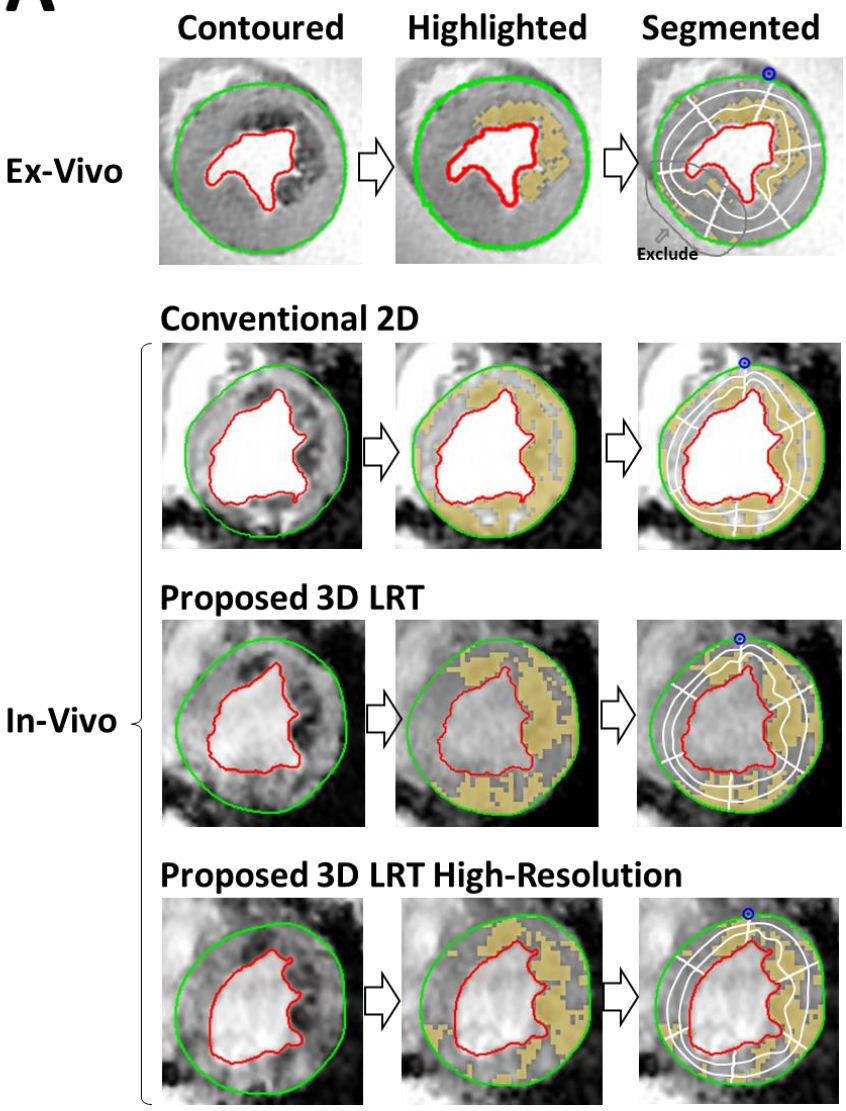
A
Contoured
Highlighted
Segmented
Ex-Vivo
Exclude
Conventional 2D
In-Vivo
Proposed 3D LRT
Proposed 3D LRT High-Resolution

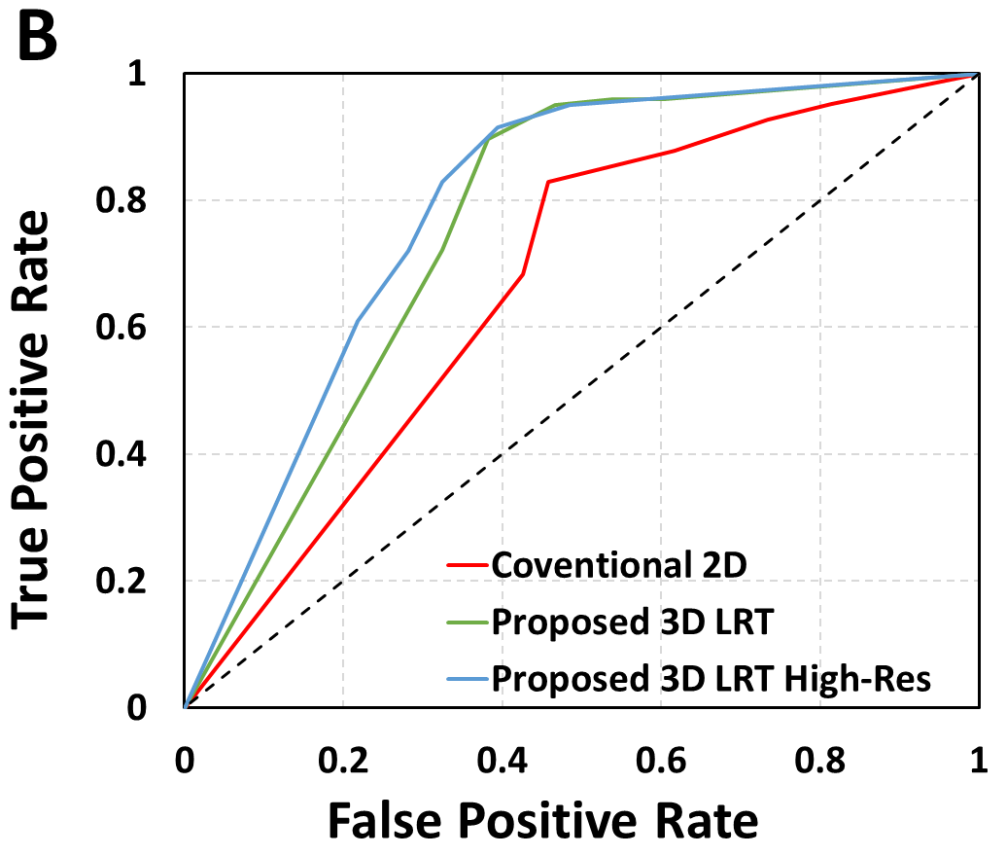

Figure 6.4. Results of diagnostic accuracy of IMH detection by conventional 2D, proposed 3D LRT and high-resolution 3D LRT T_2* imaging methods. Panel A. Ex-vivo and short-axis in-vivo T_2* images of myocardium were segmented as shown. Regions with signal intensity 2 standard deviation lower than remote myocardium were highlighted. Sensitivity and specificity of all in-vivo imaging approach for detection of IMH were analyzed using ex-vivo T_2* images as ground truth. **Panel B.** ROC curves of IMH detection by conventional 2D, proposed 3D LRT and high-resolution 3D LRT imaging methods.

6.4 Discussion

At the same resolution, 3D fully ungated LRT T_2* images showed better image quality than conventional 2D T_2* images with breath-holding and ECG-gating. The lower image quality on conventional 2D T_2* images were due to motion artifacts from unsuccessful breath-holding and ECG-gating. Especially at long echo times, as a combination of motion and off-resonance, the

susceptibility induced signal void at heart-lung interface were invading more into the myocardium as a fringe pattern.

By using a free-breathing 3D acquisition, LRT approach was able to overcome the limitations for higher resolution acquisition in 2D breath-held cardiac MR imaging. Image quality analysis showed that high-resolution 3D LRT T_2* images demonstrated better image quality than conventional 2D T_2* images. One reason that better image quality scores were given to high-resolution 3D LRT T_2* images was for a better delineation of endo- and epicardium as a benefit of imaging resolution. Another reason was that higher resolution mitigated intra-voxel dephasing caused by susceptibility difference between heart-lung interfaces or B_0 inhomogeneity, which better preserved the myocardium. Figure 6.5 shows T_2* images acquired by conventional 2D and proposed 3D LRT imaging approaches at different image resolution. T_2* images with higher image resolution of voxel size of 1.6 × 1.6 × 1.6 were reconstructed by the LRT approach. Arrows point to off-resonance artifacts near heart-lung interfaces. The off-resonance artifacts were significantly reduced on high resolution T_2* images by LRT approaches.

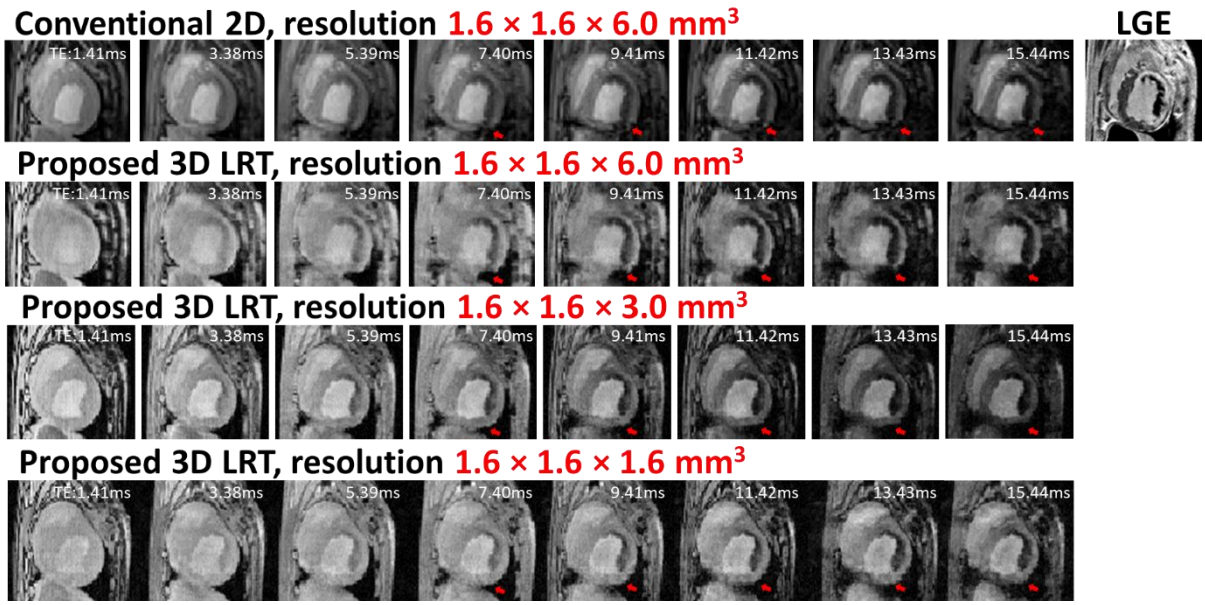

Figure 6.5. Comparison between T_2* images of IMH at different imaging resolution with LGE as reference of MI. In-phase resolution was 1.6 × 1.6 for all imaging methods. Conventional 2D T_2* images were acquired with slice thickness of 6.0 mm. T_2* images with slice thickness of 6.0, 3.0, and 1.6 mm were acquired using LRT T_2* technique. Arrows pointed to areas where off-resonance artifacts were mitigated by less intravoxel dephasing with smaller voxel size, high-resolution T_2* imaging.

No differences were found between groups with respect to T_2* measurement of remote myocardium and hemorrhage. Over a wide range (from ~13 ms in hemorrhage to ~28 ms in remote myocardium), T_2* values measured from LRT data showed excellent correlation and agreement with those from conventional 2D data at the same resolution. This was in consistent with results in Chapter 5. It's worth mentioning that no regression and Bland-Altman plots were evaluated between conventional 2D and high-resolution LRT data. Because iron deposition in intramyocardial hemorrhage is in heterogeneous distribution in a focal area within MI zones [16]. T_2* evaluated under different resolutions will introduce unpredictable variations. Individual comparison by point-to-point regression and Bland-Altman plots are not suitable ways of

validation. We reported an overall average of T_2* values of hemorrhage zones in Table 6.2 to compare T_2* measured under different resolution and results showed no difference between groups. Therefore, the newly developed LRT T_2* technique was proven to be able to provide validating T_2* values for evaluation of iron overload in the application for imaging of intramyocardial hemorrhage.

IMH extents measured in conventional 2D, proposed 3D LRT and high-resolution 3D LRT T_2* images showed no differences between each other, suggesting that the proposed LRT T_2* approaches were capable for accurately detecting intramyocardial hemorrhage.

The ROC and AUC results indicated that the proposed 3D LRT T_2* imaging method had better diagnostic capability in terms of intramyocardial detection comparing to conventional 2D T_2* imaging method. As shown in Figure 6.4A, at mean-2SD threshold, both conventional 2D and proposed 3D LRT approach were able to fully detect hemorrhage comparing to ex-vivo ground truth. However, due to motion by unsuccessful gating or blood flow, more epicardium zones were highlighted due to signal loss from motion and the remote myocardium was more inhomogeneous on conventional 2D T_2* images. This resulted in two consequences, conventional 2D T_2* images showed lower specificity at low thresholds (mean – 2SD or mean – 3SD) due to false positive in epicardium zones. Also, inhomogeneity of remote myocardium resulted in high level of standard deviation of signal intensity which led to lower sensitivity at high thresholds (mean – 4SD or higher). Therefore, there was a big difference of AUC (14.0%) between conventional 2D and proposed 3D LRT approaches.

With higher resolution, the diagnostic performance of 3D LRT T_2* method was further improved in Figure 6.4 with AUC of 0.79 (increased by 18% comparing to conventional 2D). One reason is the image resolution itself. Degradation of resolution intrinsically introduce type I and type II

errors. The other reason was due to the benefit of resolution that the mitigated susceptibility artifacts at heart-lung interface further improved specificity comparing to regular resolution 3D LRT T_2* images.

6.5 Conclusion

We conclude that the proposed fully ungated, free-breathing 3D low-rank tensor T_2* imaging technique is feasible in the application of characterization of intramyocardial hemorrhage and provide superior image quality, imaging resolution and diagnostic accuracy comparing to conventional breath-held ECG-gated 2D T_2* imaging technique.

Chapter 7: Summary and future directions

7.1 Summary

Intramyocardial hemorrhage (IMH) has emerged as an important predictor of adverse long-term outcomes in patients treated with reperfusion therapy for myocardial infarction (MI). Notably, IMH has been associated with delayed infarct healing, larger MIs, presence of persistence microvascular obstruction, higher left ventricular volumes, compromised left-ventricular ejection fraction and late-arrhythmogenic risk. This has precipitated significant clinical interest in the management of MI patients with IMH and driven investigations focused on understanding the mechanisms contributing to the adverse outcomes.

To improve the diagnostic capability of MRI for prognosis and therapeutic care of patients with hemorrhagic myocardial infarction, confounders affecting the capability of T_2* MRI imaging for assessment of intramyocardial hemorrhage have been addressed in this thesis.

In Chapter 2, to provide guidance of choice between bright-blood and dark-blood T_2* and answer the question whether dark-blood T_2* is feasible in imaging of intramyocardial hemorrhage, evaluations of performance of dark-blood T_2* in clinical assessment of intramyocardial hemorrhage were carried out in a series of pre-clinical animal studies and clinical patient studies at 1.5T and 3.0T field strength in both acute and chronic phases of MIs. While IMH can be visible on dark-blood T_2*-weighted MRI, the overall conspicuity of IMH is significantly reduced compared to that observed in bright-blood T_2*-weighted images, across infarct age in clinical and preclinical settings at 1.5T and 3.0T. Hence, dark-blood T_2*-weighted MRI should be used with the understanding that it carries the potential to misclassify hemorrhagic MIs as non-hemorrhagic MIs. To take the investigation one step further, mechanisms of signal loss on dark-blood T_2* images were explored in Chapter 3. Phantom and pre-clinical animal studies have shown a

significant signal loss due to double-inversion-recovery preparation and insufficient recovery before readout in dark-blood T_2* imaging. The signal loss can be mitigated by extending recovery time but will result in prolonged scan time and missing the blood nulling point for double-inversion-recovery preparation. T_2* maps can be used as substitute for T_2*-weighted images when using dark-blood imaging technique for hemorrhage identification. However, SNR levels, goodness of T_2* fitting and off-resonance artifacts were still unavoidable issues in dark-blood T_2* maps, affecting its diagnostic performance in assessment of intramyocardial hemorrhage. Therefore, we recommended bright-blood T_2* for imaging of intramyocardial hemorrhage.

In Chapter 4, studies were performed to emphasize on the overlooked influence of fat infiltration on T_2* fitting when quantifying iron overload in chronic hemorrhagic MIs. A confounder-corrected water-fat separation algorithm was used to separate signals from fat and iron. Fat was observed in chronic MI zones. According to results of R2* measurement, iron quantification can be biased and unreliable with the presence of fat. Therefore, it is necessary to correct for fat induced chemical shifts in assessment of intramyocardial hemorrhage in chronic phases of MIs.

In Chapter 5 and 6, to address the issue of motion artifacts due to unsuccessful breath-holding and ECG-gating in patient with acute myocardial infarctions, a 3D fully ungated free-breathing motion-resolved cardiac T_2* technique was developed based on a low-rank tensor framework. The proposed 3D LRT T_2* imaging approach was tested and validated on healthy volunteers and animal models. The proposed fully ungated, free-breathing T_2* approach could overcome image artifacts caused by motion due to failure of breath-holding and ECG gating. It is reliable to produce accurate T_2* maps for assessment of intramyocardial iron overload. High-resolution T_2* images were acquired and reconstructed by the proposed LRT approach as a benefit of 3D free-breathing acquisition. T_2* images with higher resolution showed better sensitivity and specificity on

identification of intramyocardial hemorrhage comparing to T_2* images with lower resolution. Furthermore, there's more space in improvement of imaging resolution in the proposed 3D LRT imaging approach. A resolution of 1.6 mm isotropic in cardiac T_2* images by the proposed LRT approach showed great potentials in minimizing off-resonance artifacts by reducing intravoxel dephasing.

In summary, with guidance on choice between bright-blood and dark-blood T_2*, identification of fat infiltration as a confounder, development of a fully ungated free-breathing 3D T_2* imaging technique, this thesis has made major contributions to cardiac T_2* imaging for improvement of the diagnostic capability for prognosis and therapeutic care of patients with hemorrhagic myocardial infarctions.

7.2 Future Directions

7.2.1 Improvement of SNR and CNR on Dark-Blood T_2* CMR

Even though dark-blood T_2* cardiac MRI has been shown to be problematic for assessment of intramyocardial hemorrhage, better delineation of myocardium is still beneficial for image analysis. Future work will be focused on increasing SNR and CNR on dark-blood T_2* CMR by improving and shortening adiabatic inversion pulses to reduce signal loss during double-inversion-recovery.

7.2.2 CMR Guided Iron Chelation Therapy

Results in Chapter 4 indicated a correlation between iron deposition and fat infiltration within hemorrhagic myocardial infarctions. It can be an important observation in the exploration of the mechanisms of fat infiltration within myocardial infarctions. More work will be performed using T_2* CMR as guidance during iron chelation therapy to better understand the progression of iron deposition and fat infiltration from acute to chronic phases of myocardial infarction.

7.2.3 Validation of Proposed LRT T_2* on Patients with IMH

The newly developed fully ungated free-breathing 3D T_2* technique has been validated in animals with and without intramyocardial hemorrhage. Animal scans were performed with intubation and anesthesia which reduced unexpected motions. In human studies, large movement may affect the reconstruction efficiency for LRT techniques. Results on healthy volunteers have showed that the 3D LRT T_2* technique is feasible on application for human. But it still needs to be validated on patients with hemorrhage myocardial infarctions due to different health conditions.

7.2.4 Further Development of LRT T_2* Imaging Method

With cardiac motion resolved by the LRT imaging technique, T_2* images can be analyzed in systole phases which provide better short-axis view of myocardium especially with presence of myocardium thinning in patients with myocardial infarctions. The possibility of functional analysis can be realized by optimizing imaging parameters such as flip angle for better contrast between myocardium and blood pool at short echo time. With the saved time of functional MRI during each CMR scans, higher resolution T_2* imaging parameters can be explored by longer scanning time. In the capacity of LRT framework, multi-gradient-echo T_2* images can also be acquired with T_1 or T_2 dimensions which will further improve CMR scanning time in clinical application.

References

1. Association, A.H., Heart Disease and Stroke Statistics 2018 At-a-Glance. www.heart.org, 2018.
2. Braunwald, E., Heart Disease. A textbook of cardiovascular medicine 5th ed. Philadvelphia: WB Saunders Co, 1997: p. 1464-1467.
3. Antman, E., et al., Canadian Cardiovascular Society; American Academy of Family Physicians; American College of Cardiology; American Heart Association. 2007 focused update of the ACC/AHA 2004 guidelines for the management of patients with ST-elevation myocardial infarction: a report of the American College of Cardiology/American Heart Association Task Force on Practice Guidelines. J Am Coll Cardiol, 2008. **51**(2): p. 210-247.
4. Yellon, D.M. and D.J. Hausenloy, Myocardial reperfusion injury. New England Journal of Medicine, 2007. **357**(11): p. 1121-1135.
5. Reffelmann, T. and R.A. Kloner, The "no-reflow" phenomenon: basic science and clinical correlates. Heart, 2002. **87**(2): p. 162-168.
6. Kloner, R., et al., Studies of experimental coronary artery reperfusion. Effects on infarct size, myocardial function, biochemistry, ultrastructure and microvascular damage. Circulation, 1983. **68**(2 Pt 2): p. I8-15.
7. Capone, R.J. and A.S. Most, Myocardial hemorrhage after coronary reperfusion in pigs. The American journal of cardiology, 1978. **41**(2): p. 259-266.
8. Reffelmann, T. and R.A. Kloner, Microvascular reperfusion injury: rapid expansion of anatomic no reflow during reperfusion in the rabbit. American Journal of Physiology-Heart and Circulatory Physiology, 2002. **283**(3): p. H1099-H1107.

9. Fishbein, M.C., et al., The relationship of vascular injury and myocardial hemorrhage to necrosis after reperfusion. Circulation, 1980. **62**(6): p. 1274-1279.

10. Kloner, R.A., Does reperfusion injury exist in humans? Journal of the American College of Cardiology, 1993. **21**(2): p. 537-545.

11. Olafsson, B., et al., Reduction of reperfusion injury in the canine preparation by intracoronary adenosine: importance of the endothelium and the no-reflow phenomenon. Circulation, 1987. **76**(5): p. 1135-1145.

12. Betgem, R.P., et al., Intramyocardial haemorrhage after acute myocardial infarction. Nature Reviews Cardiology, 2015. **12**(3): p. 156.

13. Roberts, C.S., F.J. Schoen, and R.A. Kloner, Effect of coronary reperfusion on myocardial hemorrhage and infarct healing. The American journal of cardiology, 1983. **52**(5): p. 610-614.

14. Lie, J., et al., Hemorrhagic myocardial infarction associated with aortocoronary bypass revascularization. American heart journal, 1978. **96**(3): p. 295-302.

15. Ganame, J., et al., Impact of myocardial haemorrhage on left ventricular function and remodelling in patients with reperfused acute myocardial infarction. European heart journal, 2009. **30**(12): p. 1440-1449.

16. Kali, A., et al., Chronic manifestation of postreperfusion intramyocardial hemorrhage as regional iron deposition: a cardiovascular magnetic resonance study with ex vivo validation. Circ Cardiovasc Imaging, 2013. **6**(2): p. 218-28.

17. Eitel, I., et al., Prognostic value and determinants of a hypointense infarct core in T_2-weighted cardiac magnetic resonance in acute reperfused ST-elevation-myocardial infarction. Circ Cardiovasc Imaging, 2011. **4**(4): p. 354-62.

18. Mather, A.N., et al., Reperfusion haemorrhage as determined by cardiovascular MRI is a predictor of adverse left ventricular remodelling and markers of late arrhythmic risk. Heart, 2011. **97**(6): p. 453-459.

19. Cokic, I., et al., Iron-Sensitive Cardiac Magnetic Resonance Imaging for Prediction of Ventricular Arrhythmia Risk in Patients With Chronic Myocardial Infarction: Early Evidence. Circ Cardiovasc Imaging, 2015. **8**(8).

20. Behrouzi, B., et al., Action of iron chelator on intramyocardial hemorrhage and cardiac remodeling following acute myocardial infarction. Basic Research in Cardiology, 2020. **115**(3): p. 1-18.

21. Bradley Jr, W., MR appearance of hemorrhage in the brain. Radiology, 1993. **189**(1): p. 15-26.

22. Gomori, J., et al., Intracranial hematomas: imaging by high-field MR. Radiology, 1985. **157**(1): p. 87-93.

23. Kumar, A., et al., Detection and quantification of myocardial reperfusion hemorrhage using T_2*-weighted CMR. JACC: Cardiovascular Imaging, 2011. **4**(12): p. 1274-1283.

24. Anderson, L., Cardiovascular T_2-star (T_2*) magnetic resonance for the early diagnosis of myocardial iron overload. European Heart Journal, 2001. **22**(23): p. 2171-2179.

25. Kali, A., et al., Detection of acute reperfusion myocardial hemorrhage with cardiac MR imaging: T_2 versus T_2. Radiology, 2013. **269**(2): p. 387-395.

26. Westwood, M., et al., A single breath-hold multiecho T_2* cardiovascular magnetic resonance technique for diagnosis of myocardial iron overload. J Magn Reson Imaging, 2003. **18**(1): p. 33-9.

27. Hernando, D., et al., Quantification of liver iron with MRI: state of the art and remaining challenges. Journal of Magnetic Resonance Imaging, 2014. **40**(5): p. 1003-1021.

28. Wood, J.C., et al., MRI R2 and R2* mapping accurately estimates hepatic iron concentration in transfusion-dependent thalassemia and sickle cell disease patients. Blood, 2005. **106**(4): p. 1460-1465.

29. Ghugre, N.R. and J.C. Wood, Relaxivity-iron calibration in hepatic iron overload: probing underlying biophysical mechanisms using a Monte Carlo model. Magnetic resonance in medicine, 2011. **65**(3): p. 837-847.

30. Westwood, M.A., et al., Normalized left ventricular volumes and function in thalassemia major patients with normal myocardial iron. Journal of Magnetic Resonance Imaging: An Official Journal of the International Society for Magnetic Resonance in Medicine, 2007. **25**(6): p. 1147-1151.

31. Meloni, A., et al., Different patterns of myocardial iron distribution by whole-heart T_2* magnetic resonance as risk markers for heart complications in thalassemia major. International journal of cardiology, 2014. **177**(3): p. 1012-1019.

32. Alpendurada, F., et al., Relation of myocardial T_2* to right ventricular function in thalassaemia major. European Heart Journal, 2010. **31**(13): p. 1648-1654.

33. Gujja, P., et al., Iron overload cardiomyopathy: better understanding of an increasing disorder. Journal of the American College of Cardiology, 2010. **56**(13): p. 1001-1012.

34. Wood, J.C., Magnetic resonance imaging measurement of iron overload. Current opinion in hematology, 2007. **14**(3): p. 183.

35. Positano, V., et al., Standardized T_2* map of normal human heart in vivo to correct T_2* segmental artefacts. NMR in Biomedicine: An International Journal Devoted to the Development and Application of Magnetic Resonance In vivo, 2007. **20**(6): p. 578-590.

36. Wood, J.C., et al., Cardiac iron determines cardiac T_2*, T_2, and T_1 in the gerbil model of iron cardiomyopathy. Circulation, 2005. **112**(4): p. 535-543.

37. Yablonskiy, D.A. and E.M. Haacke, Theory of NMR signal behavior in magnetically inhomogeneous tissues: the static dephasing regime. Magnetic resonance in medicine, 1994. **32**(6): p. 749-763.

38. Meloni, A., et al., Feasibility, reproducibility, and reliability for the T* 2 iron evaluation at 3 T in comparison with 1.5 T. Magnetic resonance in medicine, 2012. **68**(2): p. 543-551.

39. Chen, Y., et al., Quantification of myocardial hemorrhage using T_2* cardiovascular magnetic resonance at 1.5T with ex-vivo validation. Journal of Cardiovascular Magnetic Resonance, 2021. **23**(1): p. 104.

40. He, T., et al., Black-blood T_2* technique for myocardial iron measurement in thalassemia. J Magn Reson Imaging, 2007. **25**(6): p. 1205-9.

41. Liguori, C., et al., Dark blood versus bright blood T_2* acquisition in cardiovascular magnetic resonance (CMR) for thalassaemia major (TM) patients: Evaluation of feasibility, reproducibility and image quality. European Journal of Radiology, 2014. **83**(1): p. e8-e14.

42. Messroghli, D.R., et al., Clinical recommendations for cardiovascular magnetic resonance mapping of T_1, T_2, T_2* and extracellular volume: a consensus statement by the Society for Cardiovascular Magnetic Resonance (SCMR) endorsed by the European Association for Cardiovascular Imaging (EACVI). Journal of Cardiovascular Magnetic Resonance, 2017. **19**(1): p. 1-24.

43. Kidambi, A., et al., The effect of microvascular obstruction and intramyocardial hemorrhage on contractile recovery in reperfused myocardial infarction: insights from cardiovascular magnetic resonance. Journal of Cardiovascular Magnetic Resonance, 2013. **15**(1): p. 58.

44. O'Regan, D.P., et al., Reperfusion hemorrhage following acute myocardial infarction: assessment with T_2* mapping and effect on measuring the area at risk. Radiology, 2009. **250**(3): p. 916-922.

45. Avinash Kali, R.T., Rohan Dharmakumar, Detection of Acute Reperfusion Myocardial Hemorrhage with Cardiac MR Imaging: T_2 versus T_2*. Radiology, 2013.

46. Guan, X., et al., Assessment of intramyocardial hemorrhage with dark-blood T_2*-weighted cardiovascular magnetic resonance. Journal of Cardiovascular Magnetic Resonance, 2021. **23**(1): p. 1-15.

47. Bilheimer, D.W., et al., Fatty acid accumulation and abnormal lipid deposition in peripheral and border zones of experimental myocardial infarcts. Journal of nuclear medicine: official publication, Society of Nuclear Medicine, 1978. **19**(3): p. 276-283.

48. Pantanowitz, L., Fat infiltration in the heart. Heart, 2001. **85**(3): p. 253-253.

49. Roberts, W.C. and J.D. Roberts, The floating heart or the heart too fat to sink: analysis of 55 necropsy patients. The American journal of cardiology, 1983. **52**(10): p. 1286-1289.

50. Crocker, D., Lipomatous infiltrates of the heart. Archives of pathology & laboratory medicine, 1978. **102**(2): p. 69-72.

51. Dixon, W.T., Simple proton spectroscopic imaging. Radiology, 1984. **153**(1): p. 189-194.

52. Baroldi, G., et al., Lipomatous metaplasia in left ventricular scar. The Canadian journal of cardiology, 1997. **13**(1): p. 65-71.

53. Su, L., J.E. Siegel, and M.C. Fishbein, Adipose tissue in myocardial infarction. Cardiovascular Pathology, 2004. **13**(2): p. 98-102.

54. Goldfarb, J.W., et al., T_1-weighted magnetic resonance imaging shows fatty deposition after myocardial infarction. Magnetic Resonance in Medicine: An Official Journal of the International Society for Magnetic Resonance in Medicine, 2007. **57**(5): p. 828-834.

55. Molinari, G., et al., Adipose replacement and wall motion abnormalities in right ventricle arrhythmias: evaluation by MR imaging. Retrospective evaluation on 124 patients. The International Journal of Cardiac Imaging, 2000. **16**(2): p. 105-115.

56. Vignaux, O., et al., Right ventricular MR abnormalities in myotonic dystrophy and relationship with intracardiac electrophysiologic test findings: initial results. Radiology, 2002. **224**(1): p. 231-235.

57. Burke, A.P., et al., Arrhythmogenic right ventricular cardiomyopathy and fatty replacement of the right ventricular myocardium: are they different diseases? Circulation, 1998. **97**(16): p. 1571-1580.

58. Yokoo, T. and J.D. Browning, Fat and iron quantification in the liver: past, present, and future. Topics in magnetic resonance imaging, 2014. **23**(2): p. 73-94.

59. Hood, M.N., et al., Chemical shift: the artifact and clinical tool revisited. Radiographics, 1999. **19**(2): p. 357-371.

60. Babcock, L.B., J.C. Weinreb, and S.D. Horner, Edge artifacts in MR images: chemical shift effect. J Comput Assist Tornogr, 1985. **9**(2).

61. Dwyer, A.J., R.H. Knop, and D. Hoult, Frequency shift artifacts in MR imaging. J Comput Assist Tomogr, 1985. **9**(1): p. 16-18.

62. Bley, T.A., et al., Fat and water magnetic resonance imaging. Journal of Magnetic Resonance Imaging, 2010. **31**(1): p. 4-18.

63. Rieke, V., MR Thermometry, in Interventional Magnetic Resonance Imaging, T. Kahn and H. Busse, Editors. 2012, Springer Berlin Heidelberg: Berlin, Heidelberg. p. 271-288.

64. Haase, A., et al., 1H NMR chemical shift selective (CHESS) imaging. Physics in Medicine & Biology, 1985. **30**(4): p. 341.

65. Meyer, C.H., et al., Simultaneous spatial and spectral selective excitation. Magnetic resonance in medicine, 1990. **15**(2): p. 287-304.

66. Bydder, G.M., et al., The short TI inversion recovery sequence—an approach to MR imaging of the abdomen. Magnetic resonance imaging, 1985. **3**(3): p. 251-254.

67. Reeder, S.B., et al., Multicoil Dixon chemical species separation with an iterative least-squares estimation method. Magnetic Resonance in Medicine: An Official Journal of the International Society for Magnetic Resonance in Medicine, 2004. **51**(1): p. 35-45.

68. Hargreaves, B.A., et al., Dual-acquisition phase-sensitive fat–water separation using balanced steady-state free precession. Magnetic resonance imaging, 2006. **24**(2): p. 113-122.

69. Schick, F., Simultaneous highly selective MR water and fat imaging using a simple new type of spectral-spatial excitation. Magnetic resonance in medicine, 1998. **40**(2): p. 194-202.

70. Star-Lack, J., et al., Improved solvent suppression and increased spatial excitation bandwidths for three-dimensional PRESS CSI using phase-compensating spectral/spatial spin-echo pulses. Journal of Magnetic Resonance Imaging, 1997. **7**(4): p. 745-757.

71. Schick, F., et al., Improved clinical echo-planar MRI using spatial-spectral excitation. Journal of Magnetic Resonance Imaging, 1998. **8**(4): p. 960-967.

72. Dousset, M., et al., Short TI inversion-recovery imaging of the liver: pulse-sequence optimization and comparison with spin-echo imaging. Radiology, 1989. **171**(2): p. 327-333.

73. Glover, G.H. and E. Schneider, Three-point Dixon technique for true water/fat decomposition with B0 inhomogeneity correction. Magnetic resonance in medicine, 1991. **18**(2): p. 371-383.

74. Szumowski, J., et al., Phase unwrapping in the three-point Dixon method for fat suppression MR imaging. Radiology, 1994. **192**(2): p. 555-561.

75. Kovanlikaya, A., et al., Fat quantification using three-point dixon technique: in vitro validation1. Academic radiology, 2005. **12**(5): p. 636-639.

76. Berglund, J., et al., Three-point dixon method enables whole-body water and fat imaging of obese subjects. Magnetic Resonance in Medicine: An Official Journal of the International Society for Magnetic Resonance in Medicine, 2010. **63**(6): p. 1659-1668.

77. Hardy, P.A., R.S. Hinks, and J.A. Tkach, Separation of fat and water in fast spin-echo MR imaging with the three-point Dixon technique. Journal of Magnetic Resonance Imaging, 1995. **5**(2): p. 181-185.

78. Wang, Y., et al., A three-point Dixon method for water and fat separation using 2D and 3D gradient-echo techniques. Journal of Magnetic Resonance Imaging, 1998. **8**(3): p. 703-710.

79. Schneider, E. and T.W. Chan, Selective MR imaging of silicone with the three-point Dixon technique. Radiology, 1993. **187**(1): p. 89-93.

80. Reeder, S.B., et al., Iterative decomposition of water and fat with echo asymmetry and least-squares estimation (IDEAL): application with fast spin-echo imaging. Magnetic Resonance in Medicine: An Official Journal of the International Society for Magnetic Resonance in Medicine, 2005. **54**(3): p. 636-644.

81. Szczepaniak, L.S., et al., Measurement of intracellular triglyceride stores by H spectroscopy: validation in vivo. American Journal of Physiology-Endocrinology And Metabolism, 1999. **276**(5): p. E977-E989.

82. Yu, H., et al., Multiecho water-fat separation and simultaneous R2* estimation with multifrequency fat spectrum modeling. Magn Reson Med, 2008. **60**(5): p. 1122-34.

83. Reeder, S.B., et al., Water–fat separation with IDEAL gradient-echo imaging. Journal of Magnetic Resonance Imaging: An Official Journal of the International Society for Magnetic Resonance in Medicine, 2007. **25**(3): p. 644-652.

84. Sanches-Rocha, L., et al., Comparison between multi-echo T_2* with and without fat saturation pulse for quantification of liver iron overload. Magnetic resonance imaging, 2013. **31**(10): p. 1704-1708.

85. O'Regan, D.P., et al., Liver fat content and T_2*: simultaneous measurement by using breath-hold multiecho MR imaging at 3.0 T—feasibility. Radiology, 2008. **247**(2): p. 550-557.

86. Kellman, P., et al., Free-breathing T_2* mapping using respiratory motion corrected averaging. J Cardiovasc Magn Reson, 2015. **17**(1): p. 3.

87. Breuer, F.A., et al., Dynamic autocalibrated parallel imaging using temporal GRAPPA (TGRAPPA). Magnetic Resonance in Medicine: An Official Journal of the International Society for Magnetic Resonance in Medicine, 2005. **53**(4): p. 981-985.

88. Hermosillo, G., C. Chefd'Hotel, and O. Faugeras, Variational methods for multimodal image matching. International Journal of Computer Vision, 2002. **50**(3): p. 329-343.

89. Jin, N., et al., Free-breathing myocardial T_2* mapping using GRE-EPI and automatic non-rigid motion correction. J Cardiovasc Magn Reson, 2015. **17**: p. 113.

90. Shaw, J.L., et al., Free-breathing, non-ECG, continuous myocardial T_1 mapping with cardiovascular magnetic resonance multitasking. Magnetic resonance in medicine, 2019. **81**(4): p. 2450-2463.

91. Christodoulou, A.G. and Z.-P. Liang. 3D dynamic T_1 mapping of the myocardium using a time-varying subspace. in Proc. Int. Soc. Magn. Reson. Med. 2015.

92. Christodoulou, A.G., et al., Magnetic resonance multitasking for motion-resolved quantitative cardiovascular imaging. Nature biomedical engineering, 2018. **2**(4): p. 215.

93. Ma, S., et al., Accelerated Cardiac Diffusion Tensor Imaging Using Joint Low-Rank and Sparsity Constraints. IEEE Trans Biomed Eng, 2018. **65**(10): p. 2219-2230.

94. Wang, N., et al., Quantitative 3D dynamic contrast-enhanced (DCE) MR imaging of carotid vessel wall by fast T_1 mapping using Multitasking. Magnetic resonance in medicine, 2019. **81**(4): p. 2302-2314.

95. Hu, Z., et al., Magnetic resonance multitasking for multidimensional assessment of cardiovascular system: Development and feasibility study on the thoracic aorta. Magnetic Resonance in Medicine, 2020. **84**(5): p. 2376-2388.

96. Han, P., et al., Electrocardiogram-less, free-breathing myocardial extracellular volume fraction mapping in small animals at high heart rates using motion-resolved cardiovascular magnetic reesonance multitasking: a feasibility study in a heart failure with preserved

ejection fraction rat model. Journal of Cardiovascular Magnetic Resonance, 2021. **23**(1): p. 1-11.

97. Tucker, L.R., Some mathematical notes on three-mode factor analysis. Psychometrika, 1966. **31**(3): p. 279-311.

98. Liu, J., et al., Tensor completion for estimating missing values in visual data. IEEE transactions on pattern analysis and machine intelligence, 2012. **35**(1): p. 208-220.

99. De Lathauwer, L., B. De Moor, and J. Vandewalle, A multilinear singular value decomposition. SIAM journal on Matrix Analysis and Applications, 2000. **21**(4): p. 1253-1278.

100. Bitar, R., et al., In vivo 3D high-spatial-resolution MR imaging of intraplaque hemorrhage. Radiology, 2008. **249**(1): p. 259-267.

101. Link, T.M., et al., High Resolution MRI of Small Joints: Impact of Spatial Resolution on Diagnostic Performance and SNR. Magnetic Resonance Imaging, 1998. **16**(2): p. 147-155.

102. Brown, R.W., et al., Magnetic resonance imaging: physical principles and sequence design. 2014: John Wiley & Sons.

103. Reeder, S.B., et al., In vivo measurement of T* 2 and field inhomogeneity maps in the human heart at 1.5 T. Magnetic resonance in medicine, 1998. **39**(6): p. 988-998.

104. Positano, V., et al., Multislice multiecho T_2* cardiac magnetic resonance for the detection of heterogeneous myocardial iron distribution in thalassaemia patients. NMR in Biomedicine: An International Journal Devoted to the Development and Application of Magnetic Resonance In vivo, 2009. **22**(7): p. 707-715.

105. Atalay, M.K., et al., Cardiac susceptibility artifacts arising from the heart-lung interface. Magnetic Resonance in Medicine: An Official Journal of the International Society for Magnetic Resonance in Medicine, 2001. **45**(2): p. 341-345.

106. Wacker, C.M., et al., Changes in myocardial oxygenation and perfusion under pharmacological stress with dipyridamole: assessment using T^*_2 and T_1 measurements. Magnetic Resonance in Medicine: An Official Journal of the International Society for Magnetic Resonance in Medicine, 1999. **41**(4): p. 686-695.

107. Pepe, A., et al., Evaluation of the efficacy of oral deferiprone in β-thalassemia major by multislice multiecho T_2. European journal of haematology, 2006. **76**(3): p. 183-192.

108. Meloni, A., et al., Preferential patterns of myocardial iron overload by multislice multiecho T* 2 CMR in thalassemia major patients. Magnetic Resonance in Medicine, 2010. **64**(1): p. 211-219.

109. Positano, V., et al., Fast generation of T_{2*} maps in the entire range of clinical interest: Application to thalassemia major patients. Computers in biology and medicine, 2015. **56**: p. 200-210.

110. Yang, X., et al., Postprocessing correction for distortions in T_2* decay caused by quadratic cross-slice B0 inhomogeneity. Magnetic resonance in medicine, 2010. **63**(5): p. 1258-1268.

111. Liu, J., et al., Navigator-Guided Motion and B0 Correction of T_2*-Weighted Magnetic Resonance Imaging Improves Multiple Sclerosis Cortical Lesion Detection. Investigative Radiology, 2021. **56**(7): p. 409-416.

112. Cohen-Adad, J., et al., T_2* mapping and B0 orientation-dependence at 7 T reveal cyto-and myeloarchitecture organization of the human cortex. Neuroimage, 2012. **60**(2): p. 1006-1014.

113. Yang, H.-J., et al., Ultra-Homogeneous B0 field for High-Field Body Magnetic Resonance Imaging with Unified Shim-RF Coils. 2021.

114. Speck, O., J. Stadler, and M. Zaitsev, High resolution single-shot EPI at 7T. Magnetic Resonance Materials in Physics, Biology and Medicine, 2008. **21**(1-2): p. 73.

115. Bondarenko, O., et al., Standardizing the definition of hyperenhancement in the quantitative assessment of infarct size and myocardial viability using delayed contrast-enhanced CMR. Journal of Cardiovascular Magnetic Resonance, 2005. **7**(2): p. 481-485.

116. Kali, A., et al., Determination of location, size, and transmurality of chronic myocardial infarction without exogenous contrast media by using cardiac magnetic resonance imaging at 3 T. Circ Cardiovasc Imaging, 2014. **7**(3): p. 471-81.

117. O'Regan, D.P., et al., Assessment of severe reperfusion injury with T_2* cardiac MRI in patients with acute myocardial infarction. Heart, 2010. **96**(23): p. 1885-1891.

118. Norris, D.G., H. Lüdemann, and D. Leibfritz, An analysis of the effects of short T_2 values on the hyperbolic-secant pulse. Journal of Magnetic Resonance (1969), 1991. **92**(1): p. 94-101.

119. Sorce, D.J., S. Michaeli, and M. Garwood, Relaxation during adiabatic radiofrequency pulses. Current Analytical Chemistry, 2007. **3**(3): p. 239-251.

120. Gillian C Smith, J.P.C., Taigang He, Mohammed H Alam, David N Firmin, Dudley J Pennell, Value of black blood T_2* cardiovascular magnetic resonance. J Cardiovasc Magn Reson, 2011.

121. Payne, A.R., et al., Bright-blood T_2-weighted MRI has higher diagnostic accuracy than dark-blood short tau inversion recovery MRI for detection of acute myocardial infarction

and for assessment of the ischemic area at risk and myocardial salvage. Circ Cardiovasc Imaging, 2011. **4**(3): p. 210-9.

122. Simonetti, O.P., et al., "Black blood" T_2-weighted inversion-recovery MR imaging of the heart. Radiology, 1996. **199**(1): p. 49-57.

123. Triadyaksa, P., M. Oudkerk, and P.E. Sijens, Cardiac T_2* mapping: Techniques and clinical applications. Journal of Magnetic Resonance Imaging, 2020. **52**(5): p. 1340-1351.

124. Mordi, I., et al., Prevalence and Prognostic Significance of Lipomatous Metaplasia in Patients With Prior Myocardial Infarction. JACC Cardiovasc Imaging, 2015. **8**(9): p. 1111-1112.

125. Winer-Muram, H.T., et al., Computed tomography demonstration of lipomatous metaplasia of the left ventricle following myocardial infarction. Journal of computer assisted tomography, 2004. **28**(4): p. 455-458.

126. Wu, Y.-W., et al., Identification of lipomatous metaplasia in old infarcted myocardium by cardiovascular magnetic resonance and computed tomography. International journal of cardiology, 2007. **115**(1): p. E15-E16.

127. James W. Goldfarb, M.R., Jing Han, Myocardial Fat deposition after Left Ventricular Myocardial Infarction: Assessment by Using MR Water-Fat Separation Imaging. Radiology, 2009.

128. Kellman, P., D. Hernando, and A.E. Arai, Myocardial Fat Imaging. Current Cardiovascular Imaging Reports, 2010. **3**(2): p. 83-91.

129. Bydder, M., et al., Relaxation effects in the quantification of fat using gradient echo imaging. Magnetic resonance imaging, 2008. **26**(3): p. 347-359.

130. Fauhl, C., F. Reniero, and C. Guillou, 1H NMR as a tool for the analysis of mixtures of virgin olive oil with oils of different botanical origin. Magnetic Resonance in Chemistry, 2000. **38**(6): p. 436-443.

131. Segmentation, A.H.A.W.G.o.M., et al., Standardized myocardial segmentation and nomenclature for tomographic imaging of the heart: a statement for healthcare professionals from the Cardiac Imaging Committee of the Council on Clinical Cardiology of the American Heart Association. Circulation, 2002. **105**(4): p. 539-542.